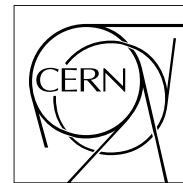


The Compact Muon Solenoid Experiment
Analysis Note

The content of this note is intended for CMS internal use and distribution only



29 June 2021 (v10, 27 February 2023)

Search for neutral long-lived particles decaying in the muon system

Artur Apresyan, Lisa Benato, Javier Duarte, Gregor Kasieczka, Martin Kwok, Cristian Pena, Joerg Schindler,
Maria Spiropulu, Christina Wang, Si Xie

Abstract

A search for long-lived particles (LLPs) decaying in the Muon System is presented. The data sample consists of 137 fb^{-1} of proton-proton collisions at $\sqrt{s} = 13 \text{ TeV}$, recorded at the LHC in 2016 – 2018. A novel technique is employed to reconstruct decays of LLPs in the muon detectors. The search is sensitive to a broad range of LLP decay modes and to masses as low as sub- GeV. The most stringent limits to date on the branching fraction of the Higgs boson to LLPs are found for proper decay lengths of a few meters. We also set first limits on the Higgs to dark quarks for the Dark Shower benchmarks in a wide range of portals.

1 Contents

2	1	Introduction	3
3	2	Trigger	5
4	3	Datasets	6
5	3.1	Data	6
6	3.2	Signal Simulations	6
7	4	Object reconstruction and identification	12
8	4.1	DT and CSC Rehit Clusters	12
9	4.2	Primary Vertex	12
10	4.3	Jets	12
11	4.4	Muons	13
12	4.5	Missing Transverse Momentum	13
13	5	Event Selection and Analysis Strategy	15
14	5.1	CSC Rehit Cluster Selection	15
15	5.2	DT Rehit Cluster Selection	20
16	5.3	ΔR between Clusters	23
17	5.4	Cosmic Shower Events	23
18	5.5	Cosmic Muon Events	26
19	5.6	DT Instrumental Noise Event	28
20	5.7	Signal Region Optimization	31
21	6	Background Estimation	37
22	6.1	Data-Driven Background Estimation Method	37
23	6.2	Validation of the Estimation Method	41
24	6.3	Expected background	43
25	7	Simulation Modeling	45
26	7.1	Simulation Modeling of CSC Clusters	45
27	7.2	Simulation Modeling of DT Clusters	48
28	7.3	Jet Veto Efficiency	49
29	7.4	Muon Veto Efficiency	50
30	8	Systematic uncertainties	52
31	8.1	Background Uncertainties	52
32	8.2	Signal Uncertainties	52
33	9	Results for the two cluster categories	56
34	9.1	Signal Prediction	56
35	9.2	Signal injection test	56
36	9.3	Observed Data	57
37	9.4	Expected and Observed Limits	58
38	10	Combination	64
39	10.1	Observed Limits	64
40	11	Summary	69
41	A	Signal Cut Flow Table	73
42	B	Signal and Data Distributions	93
43	C	Issues in Run2 Data Taking	96

44	C.1	L1 EE Pre-firing	96
45	C.2	HEM15/16 Failure	101
46	D	Study of overlap between double cluster categories and single cluster categories	102
47	D.1	Overlap between Double Cluster and Single Cluster CSC category	102
48	D.2	Overlap between Double Cluster and Single Cluster DT category	102
49	E	Signal contamination for the two cluster categories	104
50	F	Studies on extending the sensitivity to low mass regions	106
51	F.1	Detector response study	106
52	F.2	Sensitivity in low mass region	126
53	G	Selection changes for Single Cluster CSC Category	128
54	G.1	Validation of the Estimation Method	128
55	G.2	Results	132
56	H	Background Composition for Single CSC Cluster Category	134

DRAFT

57 1 Introduction

58 The production of long-lived particles (LLPs) at the LHC [1] is predicted by many BSM scenarios.
 59 Examples of such models include split supersymmetry(SUSY) [2–7], SUSY with weak R -
 60 parity violation (RPV) [8–11], SUSY with gauge-mediated supersymmetry breaking (GMSB) [12–
 61 14], “stealth SUSY” [15, 16], “Hidden Valley” models [17–19], baryogenesis triggered by weakly
 62 interacting massive particles (WIMPs) [20–22], and twin Higgs models [23–25].

63 In this note, we describe a search for LLPs at CMS by detecting particle showers using the CMS
 64 muon system. The iron shielding material comprising the return yoke of the CMS magnet
 65 combined the barrel drift-tube (DT) and endcap cathode-strip chamber (CSC) gas ionization
 66 detectors situated in several station layers within the iron material are used as a sampling
 67 calorimeter to detect electromagnetic and hadronic particle showers produced by the decay
 68 products of the LLPs. A previous version of the analysis [26] used only the endcap muon
 69 system and yielded among the best search sensitivity for LLPs with proper decay lengths above
 70 about 1 m. Geometrically localized clusters of signals from the DT and CSC chambers are used
 71 to identify hadronic showers from the decays of LLPs and distinguish it from backgrounds.
 72 The dense shielding of the CMS hadronic calorimeter and the iron return-yoke suppresses the
 73 large jet punch-through background.

74 Signal events are collected using the MET high level trigger and an offline skim requiring
 75 $\text{MET} > 200 \text{ GeV}$ is required. Signals in the DT and CSC systems are reconstructed into hits
 76 and are clustered into localized objects using the DBSCAN algorithm. The previous search de-
 77 scribed in analysis note [26] are combined with additional search categories using the barrel DT
 78 muon detectors and using two or more particle shower cluster objects. The category searching
 79 for one particle shower cluster in the barrel DT muon detector is described in analysis note [27].
 80 The category searching for two or more particle shower cluster objects is described in this note.

81 We use Higgs boson mediated production of two long-lived scalars S as the signal model
 82 benchmark to evaluate the sensitivity of this analysis. Because of the calorimetric nature of
 83 this search signature, the analysis is sensitive to a large range of LLP masses. We consider
 84 LLP masses between 0.1 and 55.0 GeV. This scalar is hypothesized to decay as a low mass
 85 Higgs boson, and will decay primarily to e^+e^- for m_S below 0.2 GeV, $\pi\pi$ for m_S between
 86 0.3 and 1.0 GeV, KK for m_S between 1.0 and 2.0 GeV, gg for m_S between 2.0 and 3.5 GeV, $c\bar{c}$ for
 87 m_S between 3.5 and 10 GeV, $\tau^+\tau^-$ for m_S between 10 and 15 GeV, and $b\bar{b}$ for m_S above 15 GeV.
 88 In Figure 1 we show the branching ratios for the main decay modes of the S as a function of its
 89 mass [28]. The proper decay length of the LLP scalar S is a free parameter of the model and is
 90 scanned between about 1 cm and 100 m in this analysis.

91 We perform the statistical combination of the endcap search category [26] with the two addi-
 92 tional search categories presented in this note and AN [27]. We demonstrate that the search
 93 sensitivity of each of the two additional search categories is similar to the sensitivity of the
 94 endcap search category. As a result the combination of all three search categories improves
 95 the search sensitivity over the previous result [26] by 50–100% depending on the proper decay
 96 length.

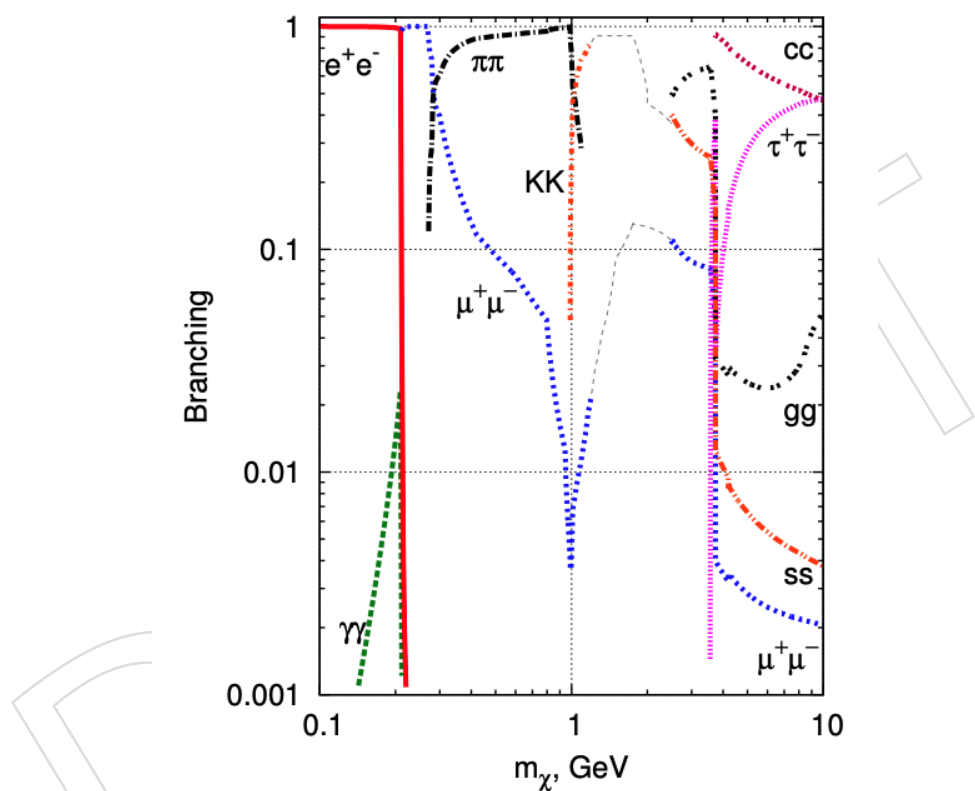


Figure 1: The scalar LLP S decay branching ratios as a function of m_S extracted from reference [28].

97 2 Trigger

98 This analysis utilizes this feature by triggering on the MET-based triggers, summarized in Ta-
 99 ble 1. For Higgs boson mediated LLP production the large MET requirement is satisfied by
 100 events with a large amount of boost provided by recoil from initial state radiation.

Table 1: Trigger paths used in the analysis.

Year	Trigger paths
2016	HLT_PFMETNoMu120_PFMHTNoMu120_IDTight
2017	HLT_PFMETNoMu120_PFMHTNoMu120_IDTight OR HLT_PFMETNoMu140_PFMHTNoMu140_IDTight OR HLT_PFMETNoMu120_PFMHTNoMu120_IDTight_PFHT60
2018	HLT_PFMETNoMu120_PFMHTNoMu120_IDTight OR HLT_PFMETNoMu140_PFMHTNoMu140_IDTight OR HLT_PFMETNoMu120_PFMHTNoMu120_IDTight_PFHT60

101 The “NoMu” version of the MET trigger is used in order to facilitate the measurement of the
 102 trigger efficiency using events triggered on Single Muon triggers because the PFMETNoMu120
 103 trigger is not biased by the presence of a muon in the trigger efficiency measurement sample.
 104 The efficiency of the trigger and offline MET cut of 200 GeV from the MET skim, calculated with
 105 respect to the geometric acceptance, ranges from 0.5% to 2% depending on the signal model.
 106 More details can be found in analysis note [26].

107 The trigger efficiency is measured in the SingleMuon dataset and compared to the simulation
 108 prediction from W+Jets MC samples. The events are required to pass the HLT_IsoMu27 trigger,
 109 has exactly 1 reconstructed muon. The muon is required to have p_T between 30 and 100 GeV
 110 and passes the tight identification and isolation requirement [29]. Events containing muons
 111 with $p_T > 100$ GeV are rejected to limit the impact of mismeasured muons on the MET. More
 112 details of the measurement are described in analysis note [26]. A trigger efficiency correction
 113 factor is calculated as the ratio of the trigger efficiency measured in data to the trigger efficiency
 114 measured in simulation, and is applied on the signal simulation samples to correct the simu-
 115 lated trigger efficiency. The trigger efficiency scale factor is applied per-event, depending on
 116 the value of MET in the event. The impact of the trigger efficiency correction is about 5% for
 117 the signal samples.

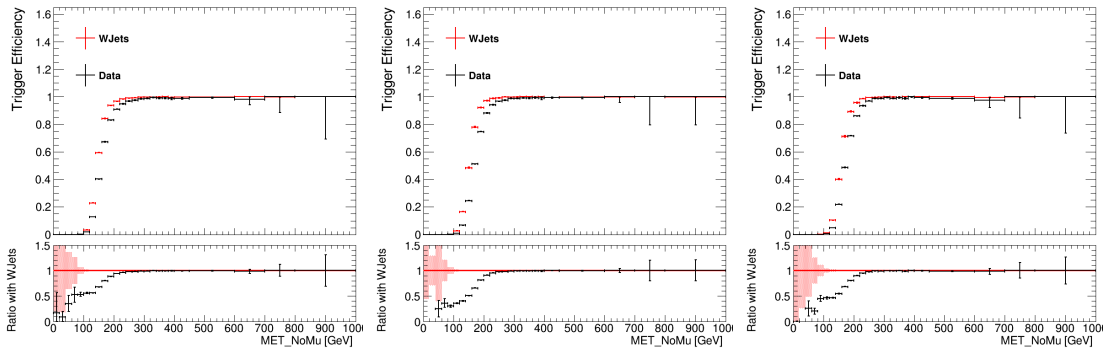


Figure 2: The trigger efficiency as a function of MET NoMu, for data and MC in 2016 (Left),
 2017 (Middle), and 2018 (Right) condition.

118 3 Datasets

119 3.1 Data

120 The data used in this analysis is from the proton-proton collision data at $\sqrt{s} = 13$ TeV in 2016,
 121 2017, and 2018, corresponding to 35.9, 41.5, and 59.7 fb^{-1} . The MET-skim RAW-RECO datasets
 122 are used and listed in Table 2. A requirement of particle flow MET > 200 GeV is imposed on
 123 the skim dataset. More details can be found in reference [26].

Table 2: RAW-RECO MET-skim datasets used in this analysis.

/MET/Run2016B-HighMET-07Aug17_ver1-v1/Raw-Reco
/MET/Run2016B-HighMET-07Aug17_ver2-v1/Raw-Reco
/MET/Run2016C-HighMET-07Aug17-v1/Raw-Reco
/MET/Run2016D-HighMET-07Aug17-v1/Raw-Reco
/MET/Run2016E-HighMET-07Aug17-v1/Raw-Reco
/MET/Run2016F-HighMET-07Aug17-v1/Raw-Reco
/MET/Run2016G-HighMET-07Aug17-v1/Raw-Reco
/MET/Run2016H-HighMET-07Aug17-v1/Raw-Reco
/MET/Run2017B-HighMET-17Nov2017-v1/Raw-Reco
/MET/Run2017C-HighMET-17Nov2017-v1/Raw-Reco
/MET/Run2017D-HighMET-17Nov2017-v1/Raw-Reco
/MET/Run2017E-HighMET-17Nov2017-v1/Raw-Reco
/MET/Run2017F-HighMET-17Nov2017-v1/Raw-Reco
/MET/Run2018A-HighMET-17Sep2018-v1/Raw-Reco
/MET/Run2018B-HighMET-17Sep2018-v1/Raw-Reco
/MET/Run2018C-HighMET-17Sep2018-v1/Raw-Reco
/MET/Run2018D-HighMET-PromptRECO-v1/Raw-Reco
/MET/Run2018D-HighMET-PromptRECO-v2/Raw-Reco

124 3.2 Signal Simulations

125 This analysis is interpreted in two signal models. The first model is the Twin Higgs model, in
 126 which two LLPs are pair produced from the Higgs boson, and each LLP decays to standard
 127 model particles. The Feynman diagram for this model is shown in left plot of Figure 3.

128 We used the centrally produced signal samples for the gluon fusion and vector boson fusion
 129 production modes for 2016, 2017, and 2018 conditions. The samples are produced with LLP
 130 masses of 7, 15, 40, and 55 GeV, as recommended by the LHC Higgs Cross-Section Working
 131 Group, and with proper lifetime $c\tau$ of 0.001, 0.01, 0.1, 1, 10, 100m. Furthermore, 3 different
 132 decay modes of the LLP are generated, with 4b, 4d and 4 τ final states respectively. Due to the
 133 heavier mass of bottom quark, only LLP masses of 15, 40, and 55 GeV are generated for the 4b
 134 final state. These samples include the gluon fusion production mode of the Higgs boson for
 135 all 3 decay modes, while the vector boson fusion (VBF) production mode of the Higgs boson is
 136 only produced for the 4b and 4 τ final states. The VBF production mode of the Higgs Boson with
 137 4d final states are produced privately. The complete list of central signal simulation samples
 138 are shown in Table 3. We use the NNNLO cross section of 48.58 pb for the gluon fusion Higgs
 139 signal sample and the NNLO cross section of 3.78 pb for the VBF Higgs production from the
 140 LHC Higgs Cross Section working group yellow report 4 [30].

141 We produced private signal samples in 2018 condition for all remaining production modes
 142 including VBF (4d final state only), WH, ZH, and ttH. The samples are generated using the

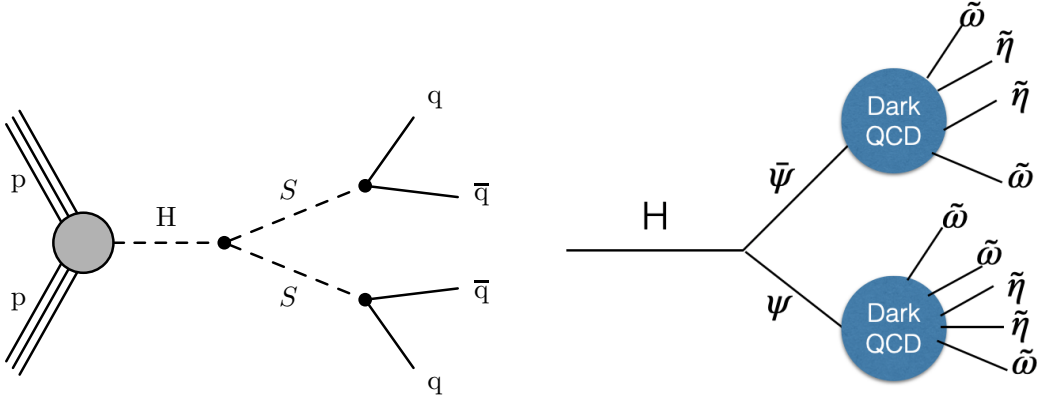


Figure 3: The left diagram shows the Higgs boson decaying to two long-lived scalars which then decay back to Standard Model fermions. The right diagram shows the Higgs boson decaying to two dark sector quarks which hadronize and form a dark shower, which depending on the portal and mass hierarchy can contain dark sector mesons that decay back to Standard Model particles.

Table 3: Signal Simulations for ggH and VBFH used in this analysis.

Samples	$\sigma(\text{pb})$
/ggH_HToSSTobbbb_MH-125_Tune*13TeV-powheg-pythia8/*/GEN-SIM-RECO	48.58
/VBFH_HToSSTo4b_MH-125_Tune*13TeV-powheg-pythia8/*/GEN-SIM-RECO	3.78
/ggH_HToSSToddः_MH-125_Tune*13TeV-powheg-pythia8/*/GEN-SIM-RECO	48.58
/ggH_HToSSTo4Tau_MH-125_Tune*13TeV-powheg-pythia8/*/GEN-SIM-RECO	48.58
/VBFH_HToSSTo4Tau_MH-125_Tune*13TeV-powheg-pythia8/*/GEN-SIM-RECO	3.78

same versions of POWHEG V2 used for the official Higgs samples using the same gridpacks.
The privately produced samples cover all of the LLP masses and proper life time as the centrally produced samples described above. In addition, we produced signal samples for LLPs with lower masses including 3.0, 1.5, 1.0, and 0.4 GeV. They include LLP decay modes to dd for 3.0 GeV, to $K^0\bar{K}^0$ and $K^+\bar{K}^-$ for 1.5 GeV, to $\pi^0\pi^0$ and $\pi^+\pi^-$ for 1.0 GeV, and e^+e^- and $\gamma\gamma$ for 0.4 GeV.

The complete list of private signal simulation samples and the corresponding NNLO cross sections are shown in Table 4. The NNLO cross section are taken from the LHC Higgs Cross Section working group yellow report 4 [30]. Note that the ZH signal samples only include the quark-initiated ZH production. The predicted signal yield for gluon-initiated ZH production is obtained from reweighting the higgs p_T and η distribution from the qqZH samples. We use the NNLO cross section of 0.1227 pb for the gluon-initiated ZH production mode from the LHC Higgs Cross Section working group yellow report 4 [30]. The reweighting procedure has been validated with a set of privately-generated ggZH samples. We propagate an additional 20% systematics on the reweighting procedure to obtain the ggZH signal yield.

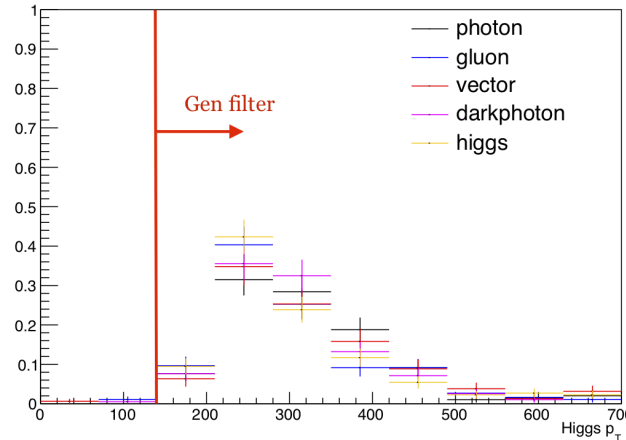
The second model used for the interpretation is the Dark Shower model [31], where a Higgs boson decays to two dark sector quarks which hadronize into lighter dark sector particles forming a "dark shower" that includes particles that eventually decay back to Standard Model particles. Such dark sector models are motivated by a range of mysteries in particle physics, including the

Table 4: Signal Simulations for the associated production modes.

Samples	$\sigma(\text{pb})$
/VBFHToSS_STodd_ms*_pl*/USER	3.782
/WminusHToSS_STo*_ms*_pl*/USER	0.5328
/WplusHToSS_STo*_ms*_pl*/USER	0.8400
/ZHToSS_STo*_ms*_pl*/USER	0.7612
/ttHHToSS_STo*_ms*_pl*/USER	0.5071

stability of the electroweak hierarchy, dark matter, and the antimatter/matter asymmetry [32]. However, the signature produced by such a dark shower can be highly challenging to simulate due to the model dependence in the properties of the new states being produced and the difficulty in predicting the dynamics of the dark sector (particularly for incalculable hadronization processes). To circumvent these issues, Ref. [31] describes a set of benchmark models where the dark sector is reduced to a single dark quark, vector meson, and scalar meson, and the number of dark QCD colors is taken as 3. Various portals through which the dark sector decays to the standard model are then considered. In the case that the decay occurs via a vector portal, the dark vector meson couples to the Standard Model and the dark scalar meson is invisible. For all other portals, the dark scalar meson couples to the Standard Model and the dark vector meson is invisible. In the case of the dark photon portal, the dark scalar meson promptly decays to two intermediate vector mediators (with a mass taken to be 0.4 times the mass of the dark scalar meson) that then undergo displaced decays back to the standard model. There are therefore double the number of displaced decays for this portal. Right plot of Figure 3 illustrates the Higgs decay and dark shower formation.

Unlike the Twin Higgs model, there are no centrally produced simulations of this Dark Shower model, so samples were privately produced for various decay portals from the dark sector to the Standard Model as well as various parameters of the long-lived particle. The simulation included a filter that required the Higgs boson had $p_T > 140 \text{ GeV}$. This filter is very efficient after the $\text{MET} > 200 \text{ GeV}$ requirement detailed in Section 2 and Section 5, as seen in Figure 4. Each of the portals tested had higher than 99% efficiency for this filter. The plot shows one choice of model parameters, but similar results were seen for all models tested.

Figure 4: Higgs boson p_T distributions for various Dark Shower portals with a long-lived particle with mass 10 GeV, proper lifetime 1 meter, and energy scale ratios $x_{i\omega} = x_{i\Lambda} = 1$, with a $\text{MET} > 200 \text{ GeV}$ cut applied. In this high MET selection, the p_T filter is nearly 100% efficient.

184 The samples cover proper lifetimes of 0.5, 1, 5, and 10m. The long-lived particle masses simu-
 185 lated for each decay portal are different because of different theoretically motivated minimums.
 186 The final parameters are $x_{i\omega}$, the ratio of the dark vector meson mass to the dark scalar meson
 187 mass, and $x_{i\Lambda}$, the ratio of the dark scalar meson mass to the dark sector QCD scale Λ . If
 188 the mass of the vector meson is greater than twice the mass of the scalar meson, it will decay
 189 promptly into scalar mesons, but the more massive vector meson can only be produced if its
 190 mass is below the dark QCD scale Λ , i.e. if $x_{i\omega} \leq x_{i\Lambda}$. Since the scalar meson does not couple
 191 to the Standard Model for the vector portal, the shower will be entirely invisible if the vector
 192 meson can decay to two scalar mesons, but for all other portals the visible content is increased
 193 because the scalar mesons do couple to the Standard Model. Three scenarios were simulated
 194 for each decay portal. In the first case, $x_{i\omega} = x_{i\Lambda} = 1$. In this scenario, both vector and scalar
 195 mesons are produced, and the shower is semi-invisible for all portals since only one of the par-
 196 ticles couples to the Standard Model. In the second case $x_{i\omega} = 2.5$ and $x_{i\Lambda} = 1$, so only scalar
 197 mesons are produced, which means the shower is fully visible (except for the vector portal
 198 where the scalar does not couple to the Standard Model). In the final case $x_{i\omega} = x_{i\Lambda} = 2.5$, so
 199 both mesons are produced and the vector can decay to two scalar mesons. Since the scalars are
 200 visible (except for vector portal), this case has a high multiplicity of visible decays. Since the
 201 showers are invisible for the vector portal whenever $x_{i\omega} > 2$, only the first scenario is simulated
 202 for that portal. The simulated parameters for each decay portal are summarized in Table 5. The
 203 visible content of the jet is summarized in the last column.

Table 5: Summary of privately produced Dark Shower signal simulations used in this analysis.

Decay portal	LLP masses [GeV]	LLP lifetimes [m]	$(x_{i\omega}, x_{i\Lambda})$	Features
Gluon	3, 5, 10, 15, 20	0.5, 1, 5, 10	(1.0,1.0), (2.5,1.0), (2.5,2.5)	hadron-rich shower
Photon	2, 5, 10, 15, 20	0.5, 1, 5, 10	(1.0,1.0), (2.5,1.0), (2.5,2.5)	photon shower
Vector	2, 5, 10, 15, 20	0.5, 1, 5, 10	(1.0,1.0)	semi-visible jet
Higgs	4, 5, 10, 15, 20	0.5, 1, 5, 10	(1.0,1.0), (2.5,1.0), (2.5,2.5)	heavy flavor-rich shower
Dark photon	2, 5, 10, 15, 20	0.5, 1, 5, 10	(1.0,1.0), (2.5,1.0), (2.5,2.5)	lepton-rich shower

204 **3.2.1 LLP Lifetime Reweighting**

205 Only a discrete number of LLP lifetimes are simulated. Therefore samples with intermediate
 206 lifetimes can be generated by reweighting from the available signal samples.

Since the decay position of the two LLPs in each event are independent, and each LLP decays with an exponential probability, the distribution of events is simply the product of the two LLP decay probabilities:

$$p(t_1, t_2 | \tau) = \frac{1}{\tau^2} \exp^{-t_1/\tau} \exp^{-t_2/\tau} \quad (1)$$

207 where t_1 and t_2 is the life-time of the first LLP and second LLP in their own rest frame respectively,
 208 given by $t_i = \frac{\text{LLP travel distance (lab frame)}}{\gamma_i \times \beta_i}$, where γ_i and β_i are the Lorentz factor and velocity
 209 of the i-th LLP respectively.

To obtain a sample with lifetime τ_{new} from a sample with lifetime τ_{old} , we assign a weight, which is the ratio of equation 1 with parameter τ_{new} and τ_{old} to the original sample:

$$w = \left(\frac{\tau_{old}}{\tau_{new}} \right)^2 \exp[(t_1 + t_2) \times \left(\frac{1}{\tau_{old}} - \frac{1}{\tau_{new}} \right)] \quad (2)$$

210 **3.2.2 Higgs p_T spectrum correction.**

211 The gen-level pT of the higgs for ggH production mode is reweighted to the best known theoretical
 212 prediction (NNLOPS) [33]. The distribution of the higgs pT from the centrally produced
 213 signal sample and theoretical prediction is shown in Fig. 5. The binning is chosen such that the
 214 statistical uncertainty is less than 10% in each bin: [0, 10, 20, 30, 40, 50, 60, 70, 80, 90, 100, 110,
 215 120, 130, 140, 150, 160, 170, 180, 190, 200, 210, 220, 230, 240, 250, 260, 270, 280, 290, 300, 310, 320,
 216 330, 340, 350, 360, 370, 380, 390, 400, 410, 420, 430, 440, 450, 460, 470, 480, 490, 500, 510, 520, 530,
 217 540, 550, 560, 570, 580, 590, 600, 625, 650, 675, 700, 750, 800, 1000, 1600]. The Higgs p_T correction
 218 increases the signal yield by a few %, as shown in Table 6.

Table 6: Increase in signal yield in the signal region. There are no events selected in the signal region for a few signal points.

CSC-CSC				
LLP mass $c\tau$	0.1 m	1 m	10 m	100 m
15 GeV	0.06%	1.51%	11.74%	\
40 GeV	7.29%	5.2%	8.58%	12.3 %
55 GeV	\	13.75%	21.67%	\

DT-DT				
LLP mass $c\tau$	0.1 m	1 m	10 m	100 m
15 GeV	6.85%	1.05%	4.42%	\
40 GeV	\	1.98%	5.94%	13.57 %
55 GeV	\	4.06%	10.24%	13.17 %

DT-CSC				
LLP mass $c\tau$	0.1 m	1 m	10 m	100 m
15 GeV	4.17%	2.26%	7.77%	\
40 GeV	\	0.72%	4.91%	7.94 %
55 GeV	\	4.7%	9.72%	9.32 %

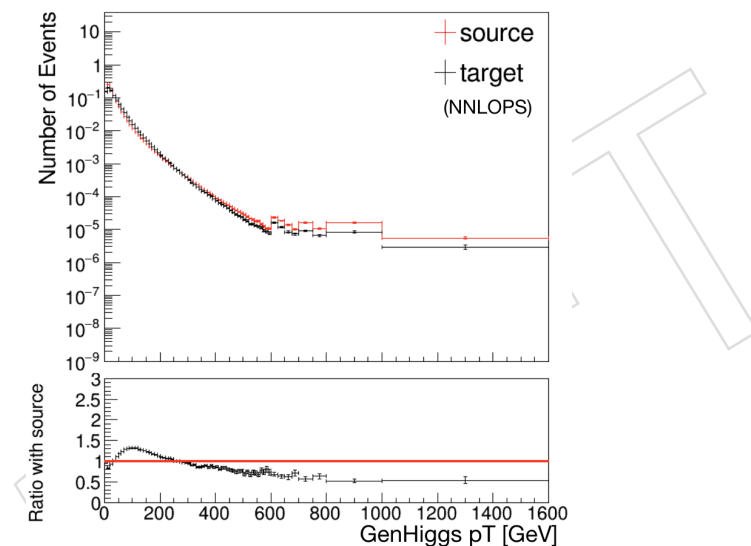


Figure 5: The generator level higgs p_T of the source (centrally produced signal sample) and target (NNLOPS) is shown. The bottom subplot is higgs p_T weight, the ratio between target and source. The binning is chosen such that the statistical uncertainty in each bin is less than 10%.

219 4 Object reconstruction and identification

220 We describe all of the reconstructed objects used in this analysis and their identification criteria.

221 4.1 DT and CSC Rechit Clusters

222 For LLPs that decay within or just prior to the gas ionization detectors of the DT and CSC muon
 223 systems, the material in the iron return yoke structure will induce a particle shower, creating
 224 a geometrically localized and isolated cluster of signal hits. These muon detector hit clusters
 225 are defined by clustering DT or CSC Rechits using their η and ϕ positions. We use the Density-
 226 based spatial clustering of applications with noise (DBSCAN) algorithm [34], with $\Delta R = 0.2$ as
 227 the distance parameter and require a minimum of 50 Rechits per cluster. Further details may
 228 be found in analysis notes [26] and [27].

229 4.2 Primary Vertex

230 The standard primary vertex selection is used. The selected primary vertex is the one with the
 231 largest sum p_T^2 .

232 4.3 Jets

233 Jets are reconstructed by clustering PF candidates with the anti- k_T algorithm with distance
 234 parameter of 0.4. The charged particles from non-primary vertices (pileup) are removed before
 235 clustering, using the Charge Hadron Subtracted (CHS) algorithm. The jet energy corrections
 236 are applied to data and MC according to the latest recommendation from JETMET POG[35]. A
 237 summary of the applied JEC versions is shown in Table 7. The jet energy scale uncertainty is
 238 propagated as a source of signal systematic in the final result, detailed in Section 8.

Table 7: Summary of JEC Global Tags Used for Data and MC

Data 2016 BCD	Summer16_07Aug2017BCD_V11_DATA
Data 2016 EF	Summer16_07Aug2017EF_V11_DATA
Data 2016 GH	Summer16_07Aug2017GH_V11_DATA
Data 2017 B	Fall17_17Nov2017B_V32_DATA
Data 2017 C	Fall17_17Nov2017C_V32_DATA
Data 2017 DE	Fall17_17Nov2017DE_V32_DATA
Data 2017 F	Fall17_17Nov2017F_V32_DATA
Data 2018 A	Autumn18_RunA_V19_DATA
Data 2018 B	Autumn18_RunB_V19_DATA
Data 2018 C	Autumn18_RunC_V19_DATA
Data 2018 D	Autumn18_RunD_V19_DATA
MC 2016	Summer16_07Aug2017_V11_MC
MC 2017	Fall17_17Nov2017_V32_94X_MC
MC 2018	Autumn18_V19_MC

239 In this analysis, PF jets with $|\eta| < 2.5$ and $p_T > 30$ (50) GeV are used to veto CSC (DT) clusters
 240 caused by punchthrough jets if the cluster centroid is within $\Delta R < 0.4$ of the PF jet. The jet
 241 veto threshold used in this double cluster analysis is larger than the 10 GeV jets used in the
 242 single cluster DT and CSC analysis. This suppresses clusters that are produced by either a jet
 243 punching through the shielding or by a K_L produced in the hadronization of the jet decaying

244 within the CSC (DT) geometric acceptance region in the same way as a signal LLP. The inefficiency of this jet veto on signal is caused by random matching to pileup jets. We measure
 245 the signal efficiency for this jet veto to be about 95-97% (98-99%) per CSC (DT) cluster. We
 246 measure the simulation modelling of the jet veto by randomly selecting cluster positions in the
 247 signal cluster distribution and measuring how often a random match is made with pileup jets
 248 from ZToMuMu events in data and MC. This measurement agrees with simulation prediction
 249 to within 1%. Events are also required to have at least one jet with $p_T > 30$ GeV passing the
 250 TightLepVeto ID[36], and with $\Delta R > 0.4$ to the muon detector rechit clusters because the large
 251 MET requirement implies that a high p_T ISR jet is recoiling against the Higgs boson in signal
 252 events. We apply the recommended TightLepVeto ID following the Run2 recommendations
 253 from the JETMET POG twiki [36].
 254

255 4.4 Muons

256 Standard muon reconstruction is used to construct muon candidates [37].

257 GlobalMuon objects with $p_T > 30$ GeV and $|\eta| < 2.4$ are used to veto CSC clusters caused by
 258 muons producing a photon via bremsstrahlung if the CSC cluster centroid is within $\Delta R < 0.4$
 259 of the muon. The signal efficiency of this muon veto is about 99%. This selection looser than
 260 the 20 GeV RECO muon veto applied in the single cluster CSC category, improving the signal
 261 efficiency by 10%.

262 Muon objects passing the Muon POG loose ID criteria [29] with $p_T > 10$ GeV and $|\eta| < 2.4$
 263 are used to veto DT clusters caused by muons producing a photon via bremsstrahlung if the DT
 264 cluster centroid is within $\Delta R < 0.4$ of the muon. This selection is the same as the muon veto
 265 for the single cluster DT category. The signal efficiency of this muon veto is about 99%.

266 4.5 Missing Transverse Momentum

267 The missing transverse momentum used in this analysis is the Type-I Corrected PFMET[38],
 268 which is the negative of the vector sum of all particle flow candidates in the event. The Type-
 269 I Corrected PFMET uses the AK4PF jet collections and propagates the jet energy corrections
 270 (JEC) to p_T^{miss} . The xy-Shift correction is applied to reduce the MET ϕ modulation. The cor-
 271 rection has a large effect on the MET ϕ shape when MET is small, but the MET requirement
 272 is > 200 GeV in our analysis. The correction has a small (1%) effect for both the signal and
 273 background yield.

274 For the 2017 data, the p_T^{miss} measurement is affected by an issue that causes the EE towers to
 275 be noisy. To mitigate this effect, we follow the recommended recipe[39] to disregard jets with
 276 $2.65 < |\eta| < 3.139$ and p_T (raw) < 50 GeV in the p_T^{miss} calculation. We apply this recommended
 277 recipe for 2017 data and MC events (corresponding to 2017 data).

278 In many cases, large MET can be caused by detector noise, cosmic rays, and beam-halo par-
 279 ticles. Therefore, to identify the "fake" MET induced by the non-collisional background, the
 280 MET filters are applied based on the recommendations from the JETMET group[40] for both
 281 data and MC, as shown in Table 8. The signal efficiency of the MET filters is above 98% for all
 282 signal models.
 283

Table 8: List of MET filters used in the analysis.

Filter	Years	Applied to Data	Applied to MC
primary vertex filter	2016, 2017, and 2018	Yes	Yes
beam halo filter	2016, 2017, and 2018	Yes	Yes
HBHE noise filter	2016, 2017, and 2018	Yes	Yes
HBHEiso noise filter	2016, 2017, and 2018	Yes	Yes
ECAL TP filter	2016, 2017, and 2018	Yes	Yes
Bad PF Muon Filter	2016, 2017, and 2018	Yes	Yes
ee badSC noise filter	2016, 2017, and 2018	Yes	No
ECAL bad calibration filter	2017 and 2018	Yes	Yes

284 5 Event Selection and Analysis Strategy

285 Following the same general strategy outlined in analysis note [26], we select events with MET
 286 > 200 GeV, that defines the HighMET RAW-RECO skim dataset used. We require at least one
 287 jet with $p_T > 30$ GeV and $|\eta| < 2.4$, passing the TightLepVeto jet ID criteria defined by the
 288 JetMET POG.

289 In this analysis, we slightly modify the search described in [26] to explicitly categorize events
 290 into those with a single CSC cluster, a single DT cluster, and two or more clusters. The analysis
 291 details for the category with a single DT cluster can be found in analysis note [27]. In the fol-
 292 lowing subsections we discuss the analysis details of the category with two or more clusters.
 293 There are three sub-categories defined by having two DT clusters (DT-DT), two CSC clusters
 294 (CSC-CSC), or one DT and one CSC cluster (DT-CSC). The background rejection for the require-
 295 ment to have two clusters is very large, which allows us to significantly loosen the cluster-level
 296 selection requirements and vetos and consequently improve signal efficiency.

297 5.1 CSC Rechit Cluster Selection

298 We describe the selections applied for CSC Rechit Clusters. For all the plots shown, 2 CSC
 299 clusters are required per event. For the signal events, we use the ggH production and dd decay
 300 mode as benchmark and require both clusters to match to the two LLPs that decay in CSC.
 301 For background, we plot the data distribution in a signal-depleted control region, where both
 302 clusters are required to have $N_{rechits} < 100$.

303 First, we apply a time cut on the CSC cluster time. The time of the cluster, $t_{cluster}$, is defined as
 304 the weighted mean time of recHits making up the cluster. The time for each recHit is calculated
 305 from the weighted average of the wire digi and strip digi time that make up the recHits, where
 306 the weights are the inverse squared of the time error. The strip digi time error is 7 ns and wire
 307 digi time error is 8.6 ns. A tail pruning is applied to times that are more than 9σ away. This
 308 time definition is based on the CSC segment time definition, referenced in this code [41]. The
 309 distribution of the cluster time for is shown in Fig. 6, where we observe that the signal clusters
 310 are mostly in-time, but clusters from data show clear contribution of out-of-time pileup. We
 311 define the signal region to be the region of $t_{cluster}$ between -5 and 12.5 ns. The signal does exhibit
 312 a longer right hand tail due to delays originating from slow moving LLPs. Therefore, we try
 313 to extend the time window on the right side as much as possible before allowing clusters from
 314 the next bunch crossing in. This requirement has a signal efficiency of 99%.

315 To avoid pathological clusters that contain RecHits from multiple bunch crossings, cluster time
 316 spread is required to be less than 20 ns for both CSC clusters. This is the same requirement that
 317 was used for EXO-20-015 [26]. The time spread is defined as $\sqrt{\frac{\sum(t_i - \bar{t})^2}{N}}$, where t_i is the strip digi
 318 time of the i-th RecHit, \bar{t} is the mean of strip digi time in the cluster, and N is the number of
 319 RecHits in the cluster. This requirement has a signal efficiency of 97% on the signal samples.
 320 The shape of the signal and background maximum time spread distribution is shown in Fig. 7,
 321 where the in-time cut described above has been applied.

322 To suppress CSC Rechit clusters from punch-through jets in the muon system, clusters that are
 323 geometrically matched to jets are vetoed. The signal and data distributions of the maximum p_T
 324 of the jet that the clusters are matched to is shown in Fig. 8. A cluster is vetoed if it is matched
 325 to any PF jet with $p_T > 30$ GeV and $|\eta| < 2.5$ to within $\Delta R < 0.4$. No jet ID requirements are
 326 applied to jets used for this veto. This veto has a signal efficiency of 91%-96%.

327 To suppress CSC Rechit clusters from muons that undergo bremsstrahlung in the muon system,

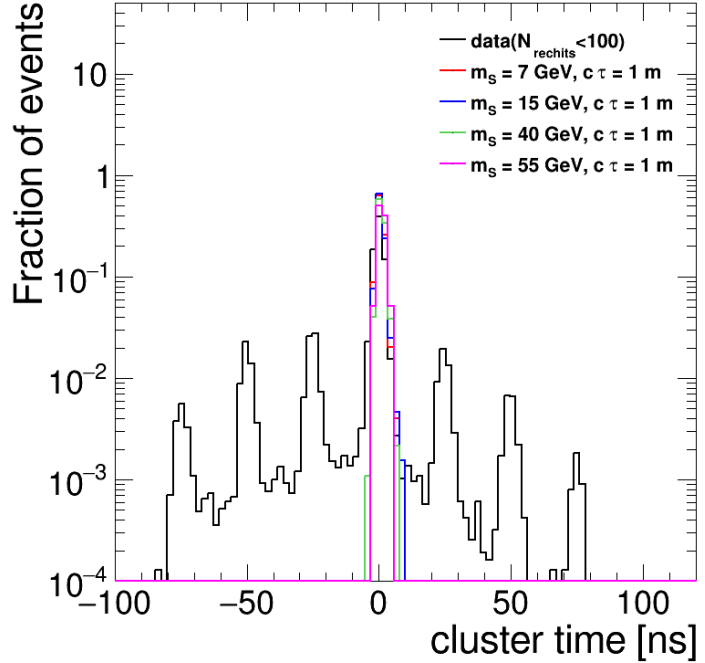


Figure 6: The signal and background distribution for cluster time is shown. Both signal and background, two clusters are required per event and the time of both clusters are plotted. For signal, the clusters are required to match to different LLPs and for background, both clusters are required to have $N_{rechits} < 100$.

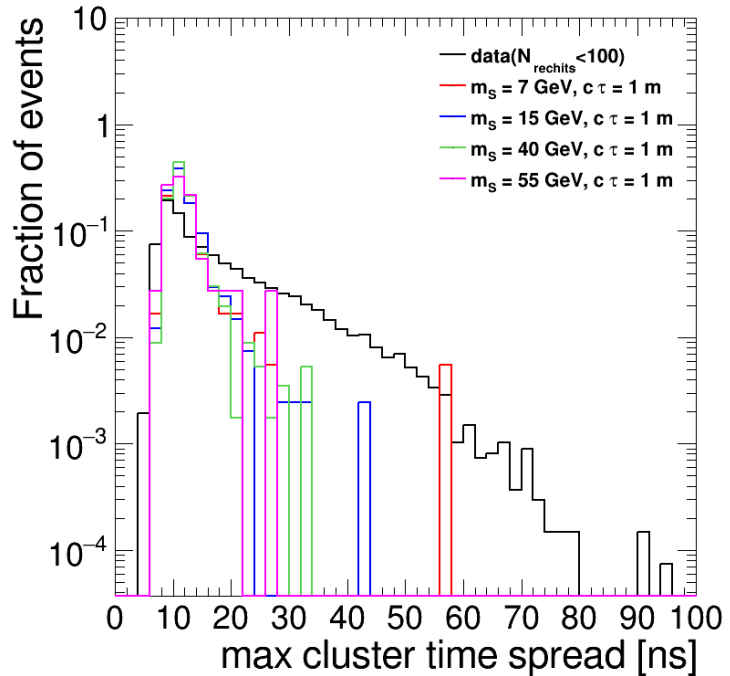


Figure 7: The signal and background distributions for maximum cluster time spread is shown.

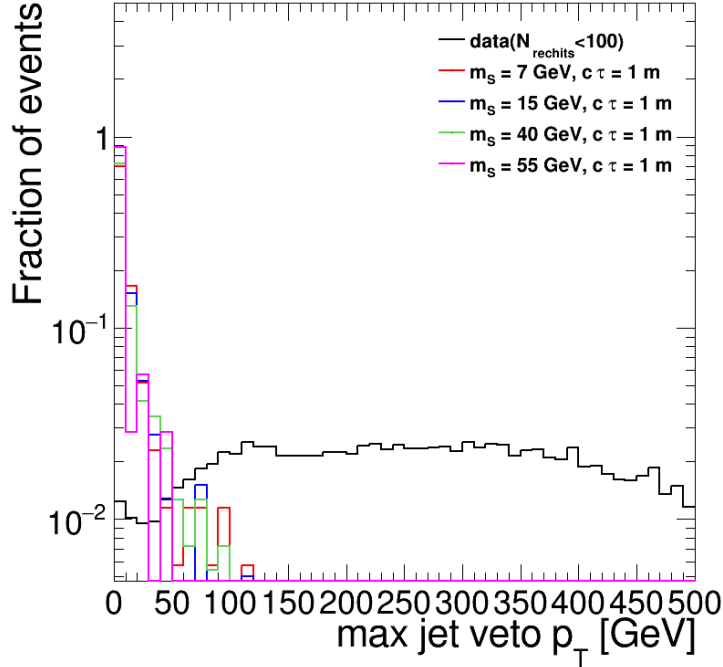


Figure 8: The signal and background distributions for the maximum matched jet p_T are shown. The clusters are required to pass the in-time cut and time spread cut described above.

328 clusters that are geometrically matched to any global muons are vetoed. A cluster is vetoed if
 329 it is matched to any global muons with $p_T > 30$ GeV and $|\eta| < 2.4$, within $\Delta R < 0.4$. The
 330 distribution of the p_T of muons that background and signal clusters are matched to is shown
 331 in Fig. 9.

332 For signal events of interest with two reconstructed clusters, both LLPs decay in the muon
 333 system. In this situation the MET is equal to the higgs p_T . The large MET requirement implies
 334 that the Higgs is boosted and the flight direction of the two LLPs are close to each other and
 335 to the MET. Therefore, both clusters are expected to have a ϕ direction close to the MET ϕ
 336 direction. This is not the case for backgrounds, where the direction of the two clusters are more
 337 independent of the MET direction. The distributions for the $\Delta\phi(\text{cluster}, \text{MET})_{\text{max}}$ are shown
 338 in Figure 10 for signal and background. We require $\Delta\phi(\text{cluster}, \text{MET})_{\text{max}} < 1.2$ to suppress
 339 background. This selection is applied to CSC clusters in CSC-CSC and DT-CSC categories. The
 340 cut threshold requirement was chosen to have more than 90% signal efficiency for LLP mass of
 341 15, 40, and 55 GeV and LLP lifetime of 1m and 80% efficiency for 7 GeV LLP with 1m lifetime.

342 Finally, to suppress clusters produced by punchthrough we veto clusters that are entirely con-
 343 tained in ME11 by requiring $N_{\text{ME11hits}}/N_{\text{rechits}} < 1$. The signal and background distributions of
 344 the maximum $N_{\text{ME11hits}}/N_{\text{rechits}}$ between two clusters are shown in Fig. 11. This requirement
 345 has a signal efficiency of 95%-98%.

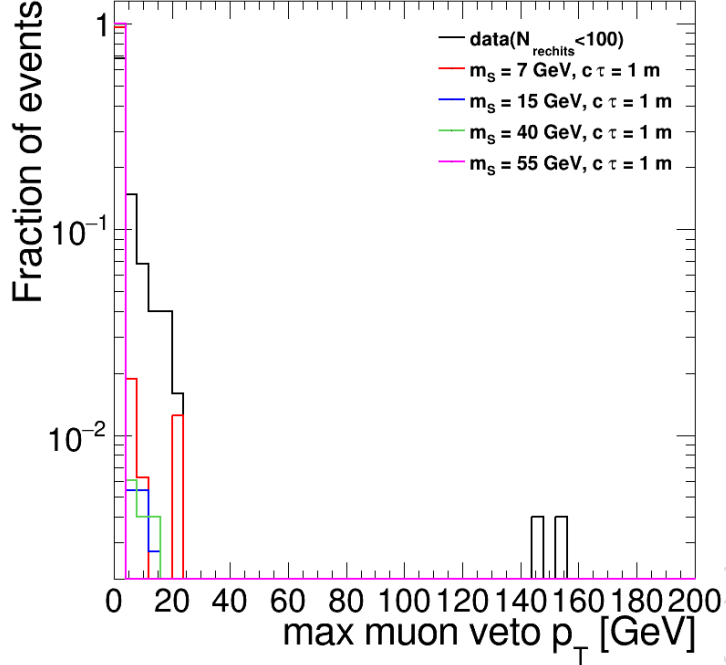


Figure 9: The signal and background distributions for the maximum matched muon p_T are shown. The clusters are required to pass the in-time cut, time spread cut, and jet veto described above. Most background events that are matched to muons are matched to jets as well, so after the jet veto is applied, only background clusters from high p_T are left.

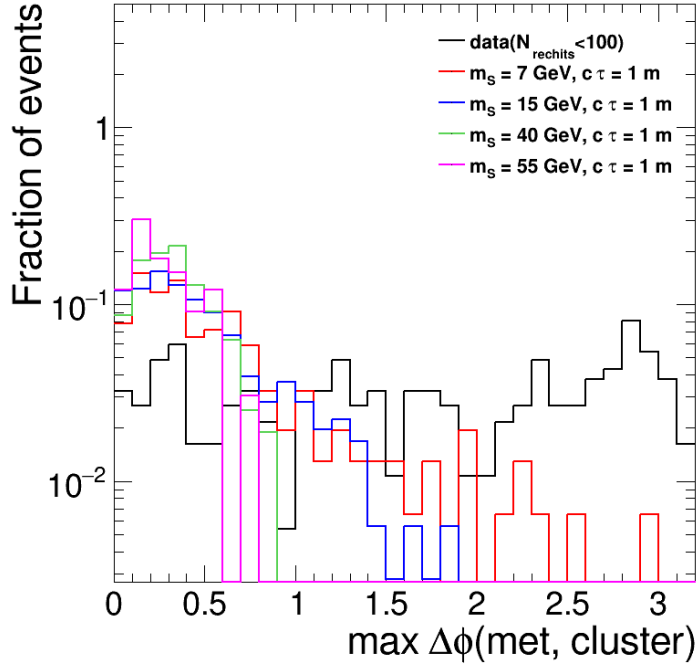


Figure 10: The signal and background distributions for $\Delta\phi(\text{cluster}, \text{MET})_{max}$ is shown. The clusters are required to pass the in-time cut, time spread cut, and jet veto described above.

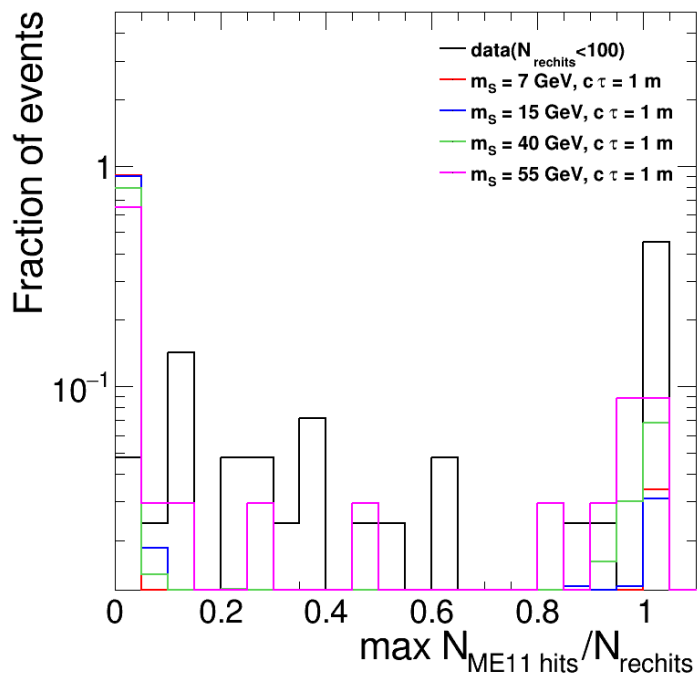


Figure 11: The signal and background distributions for $N_{\text{ME11 hits}} / N_{\text{rechits}}$ is shown. Signal and data are required to pass all others selections described above.

346 5.2 DT Rechit Cluster Selection

347 We describe the selections applied for DT Rechit Clusters. For all the plots shown, 2 DT clusters
 348 are required per event. For the signal events, we use the ggH production and dd decay mode
 349 as benchmark and require both clusters to match to the two LLPs that decay in DT. For back-
 350 ground, we plot the data distribution in the control region, where both clusters are required to
 351 have $N_{\text{rechits}} < 80$.

352 To suppress clusters from punch-through jets, clusters that are geometrically matched to any
 353 jets are vetoed. The signal and data distributions of the maximum p_T of the jet that the clusters
 354 are matched to is shown in Fig. 12. A cluster is vetoed if it is matched to any PF jet with $p_T > 50$
 355 GeV and $|\eta| < 2.4$ to within $\Delta R < 0.4$. No jet ID requirements are applied to jets used for this
 veto. The signal efficiency of this veto is $>98\%$.

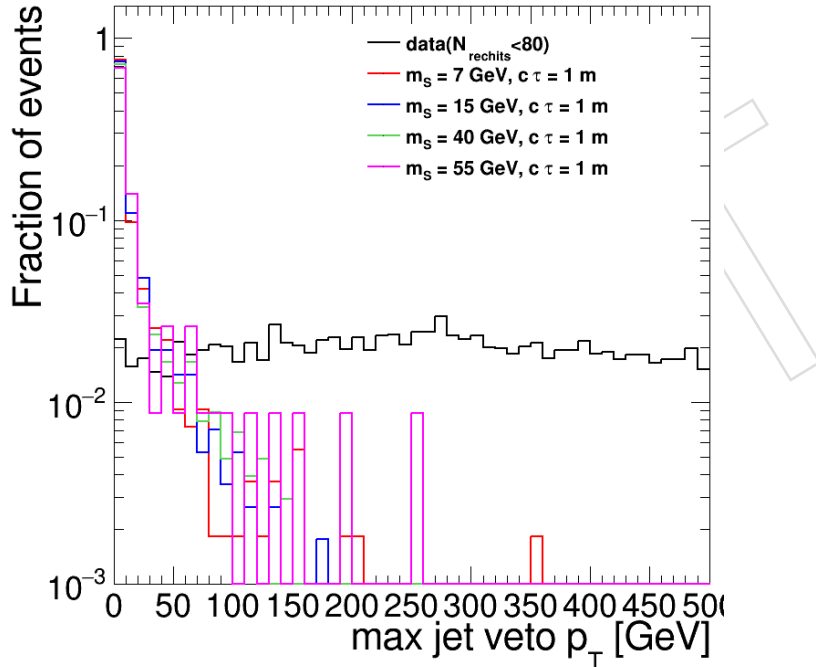


Figure 12: The signal and background distributions for the maximum matched jet p_T are shown. For signal, the clusters are required to match to different LLPs and for background, both clusters are required to have $N_{\text{rechits}} < 80$.

- 356
- 357 To suppress DT Rechit clusters from muons that undergo bremsstrahlung in the muon system,
 358 clusters that are geometrically matched to any loose ID muons are vetoed. A cluster is vetoed
 359 if it is matched to any loose ID muons with $p_T > 10$ GeV and $|\eta| < 2.4$, within $\Delta R < 0.4$. This
 360 muon veto is the same as that applied in the single cluster DT analysis. The distribution of the
 361 p_T of muons that background and signal clusters are matched to is shown in Fig. 13.
- 362 For the same reason that was described above for CSC clusters, we require $\Delta\phi(\text{cluster}, \text{MET})_{\text{max}} < 1$.
 363 The distributions for the $\Delta\phi(\text{cluster}, \text{MET})_{\text{max}}$ are shown in Figure 14 for signal and back-
 364 ground. The cut threshold requirement was chosen to have more than 90% signal efficiency
 365 for LLP mass of 15, 40, and 55 GeV and LLP lifetime of 1m and 80% efficiency for 7 GeV LLP
 366 with 1m lifetime. This selection is applied to DT clusters in DT-DT and DT-CSC categories.
- 367 To further suppress jet punchthrough background, we veto clusters that have $>90\%$ of the

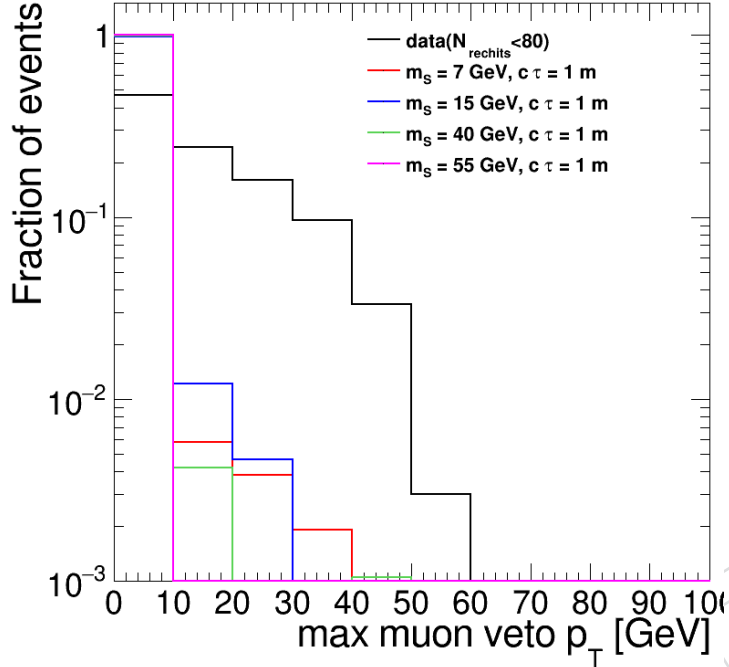


Figure 13: The signal and background distributions for the maximum matched muon p_T are shown. The clusters are required to pass the jet veto described above.

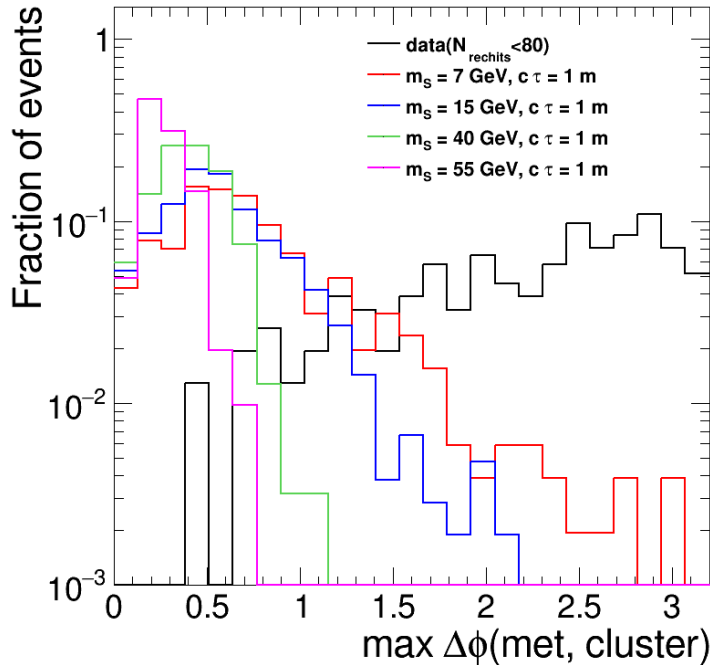


Figure 14: The signal and background distributions for $\Delta\phi(\text{cluster}, \text{MET})_{max}$ is shown. The clusters are required to pass the jet veto and muon veto described above.

³⁶⁸ hits contained in MB1, by applying the cut $N_{\text{MB1hits}}/N_{\text{rechits}} < 0.9$. The signal and background
³⁶⁹ distributions of the maximum $N_{\text{MB1hits}}/N_{\text{rechits}}$ between two clusters are shown in Fig. 15.

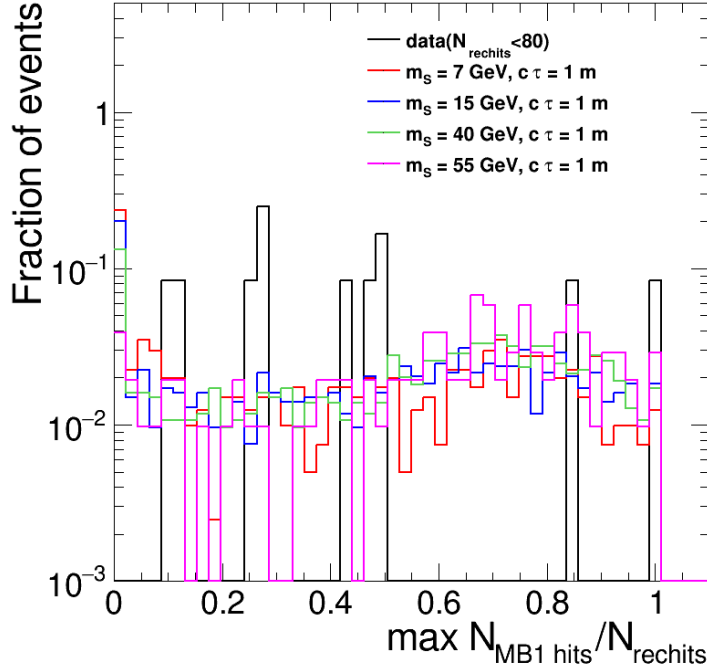


Figure 15: The signal and background distributions for $N_{MB1\text{hits}}/N_{\text{rechits}}$ is shown. Signal and data are required to pass all others selections described above.

370 To further suppress muon bremsstrahlung background, we veto clusters that have hits in all 4
 371 stations and the ratio of number of hits in the minimum and maximum station ($N_{\text{hitminstation}}/N_{\text{hitmaxstation}}$)
 372 is larger than 0.4. Clusters from muon bremsstrahlung would likely have similar number of hits
 373 in all 4 stations, while signal clusters only have hits in 2 or 3 stations, with the ratio close to 0,
 374 as shown in Fig. 16.

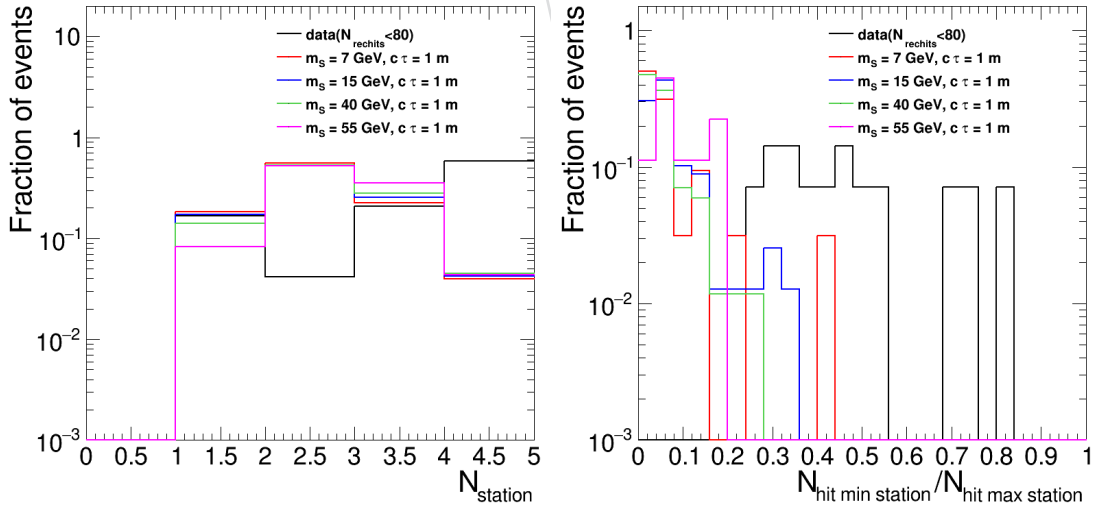


Figure 16: The signal and background distributions for the number of stations (Left) and $N_{\text{hitminstation}}/N_{\text{hitmaxstation}}$ (Right) are shown. Signal and data are required to pass all others selections described above. Additionally, clusters that are plotted in $N_{\text{hitminstation}}/N_{\text{hitmaxstation}}$ (Right) are required to have 4 stations.

375 5.3 ΔR between Clusters

376 For signal events of interest with two reconstructed clusters, the ΔR between two LLPs, thus
 377 between clusters, are usually small. The ΔR distributions of the two clusters for signal and
 378 data for each of the 3 categories are shown in Fig. 17. Based on the signal and background
 379 distributions, we apply a cut of $\Delta R < 2$ for CSC-CSC category and a cut of $\Delta R < 2.5$ for DT-
 380 CSC category. No cuts applied for DT-DT category.

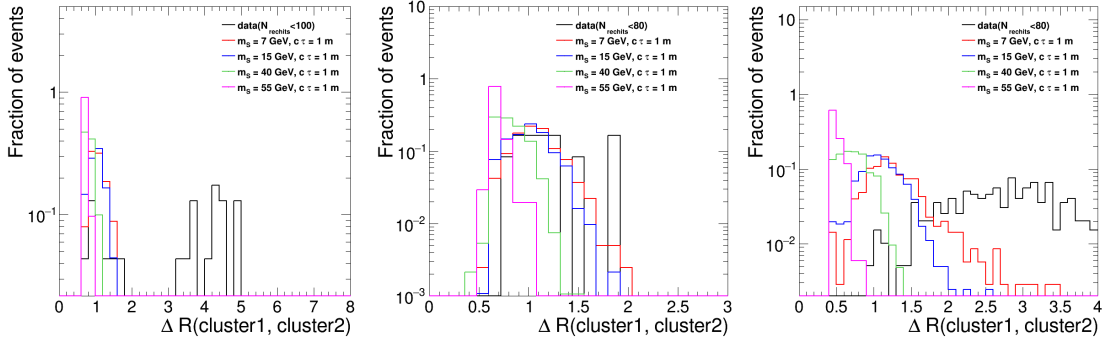


Figure 17: The signal and background distributions for $\Delta R(\text{cluster1}, \text{cluster2})$ is shown for the CSC-CSC (left), DT-DT (center), and CSC-DT (right) category. All cluster-level selections described in the previous sections are applied.

381 5.4 Cosmic Shower Events

382 One specific type of background are cosmic shower events. In such events several cosmic
 383 muons pass through the detector and create showers in the CSC and DT detectors. An event
 384 display of a cosmic muon shower event is shown in Fig. 18. In this example event, there are
 385 more than 10,000 CSC Rechits, distributed across several bunch crossings. We select a control
 386 sample of such events with more than 2000 early (time $< -25 \text{ ns}$) CSC rechits in an early OOT
 387 cluster, as shown in Fig. 19. We observe that these events contain many rechits distributed over
 388 many different parts of the detector.

389 To quantify this effect we define a quantity called “rings” as follows. The CSC detector is
 390 composed of four stations in each of the two endcaps : ME ± 1 , ME ± 2 , ME ± 3 , ME ± 4). Station
 391 ME ± 1 contains three rings (ME $\pm 1/1$, ME $\pm 1/2$, ME $\pm 1/3$), while the remaining three stations
 392 contain two rings each (ME $\pm 2/1$, ME $\pm 2/2$, ME $\pm 3/1$, ME $\pm 3/2$, ME $\pm 4/1$, ME $\pm 4/2$). There
 393 are a total of 18 CSC rings. The DT detector is composed of five wheels : MB0, MB ± 1 , MB ± 2 .
 394 Each wheel has four different layers. We define a DT ring to be a particular layer in a particular
 395 wheel. There are a total of 20 DT rings. We count how many CSC and DT rings with at least 50
 396 rechits there are in an event. This is plotted in Fig. 20, for the control sample of cosmic muon
 397 shower events compared to simulated signal events. We observe that the cosmic muon shower
 398 events occupy a large number of DT and CSC rings, while signal events from LLP decays are
 399 localized in a few rings. Therefore, we veto events that have more than 10 rings with at least 50
 400 Rechits from our signal region. This requirement has near 100% efficiency for the signal.

401 To validate the signal efficiency in data, we select events in the muon bremsstrahlung control
 402 region containing an isolated muon track has been matched to a cluster in the CSC detector.
 403 Such events are a close analogue to the signal events and are used to measure the efficiency of
 404 the cosmic muon shower veto. If high levels of electronic noise were present, we may observe
 405 a large number of rings with many rechits, resulting in signal efficiency loss. The distribution

406 of the number of CSC and DT rings is shown in Fig. 20, and we confirm that the efficiency of
 407 the veto is 100%.

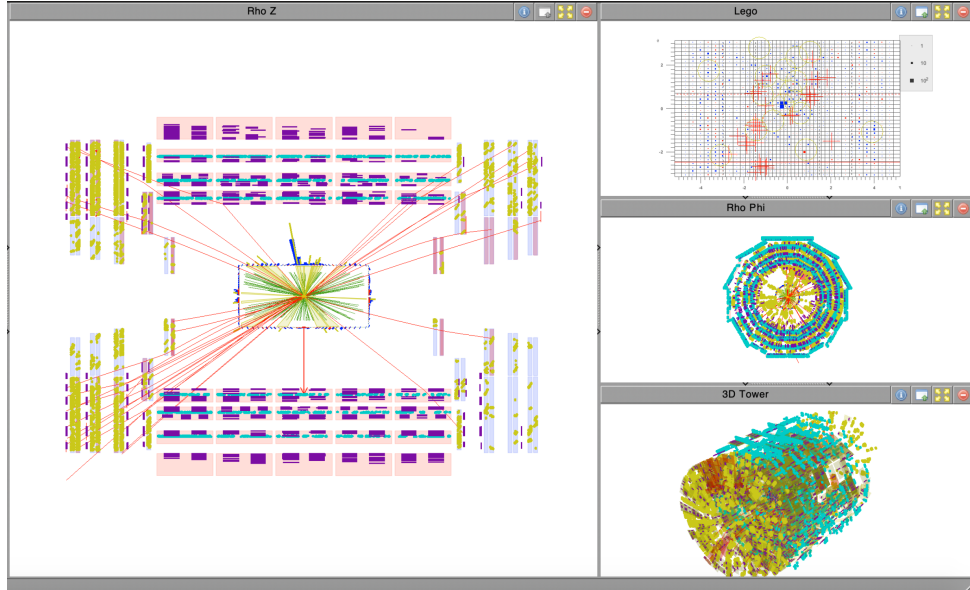


Figure 18: Event display of a cosmic muon shower event that creates showers with a large number of CSC, DT, and RPC Rechits. The red lines in the left figure are reconstructed muons. The yellow dots are CSC Rechits; purple lines are RPC Rechits; Cyan lines are DT Rechits.

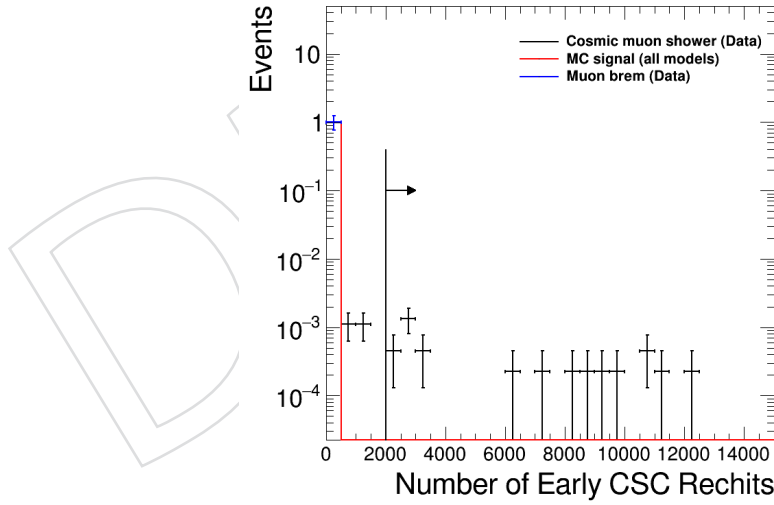


Figure 19: The number of early OOT CSC Rechits. This distribution is used to select a sample enriched in cosmic muon shower events.

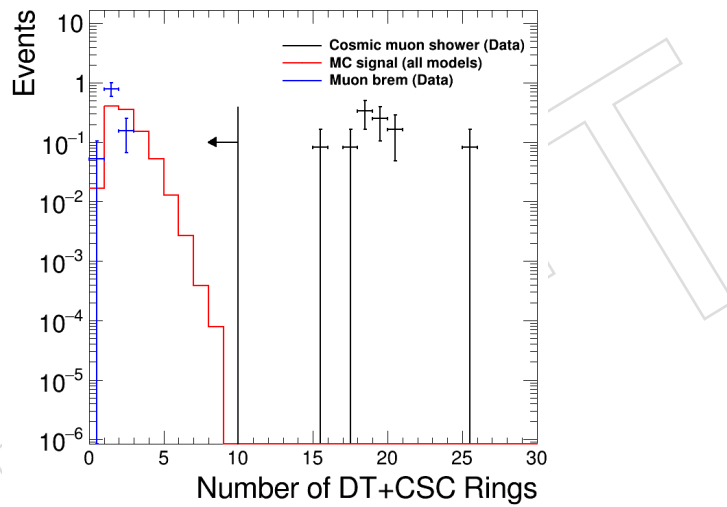


Figure 20: The number of DT and CSC rings that have at least 50 RecHits is shown for the cosmic muon shower control sample, the signal simulation sample, and the muon bremsstrahlung control sample. The histograms have been normalized to unit area. This variable is used to identify the cosmic muon shower background events.

408 5.5 Cosmic Muon Events

409 When there are only one or a few cosmic muons passing through the detector, they can result
 410 in a reconstructed jet as they pass through the calorimeters. Due to the lack of associated
 411 tracks, they generally fail the jet ID. We select a control sample of such events by inverting the
 412 tight jet ID of the ISR jet. In this cosmic muon-enriched control region, we observed 5 cosmic
 413 muon events in the DT-DT category, and no events in the CSC-CSC or DT-CSC categories. All
 414 5 cosmic muon events observed in the DT-DT category look similar to the example shown in
 415 Fig. 21. There are a few muons traversing the drift tubes, leaving segments in all 4 stations in
 416 both the upper and lower hemisphere of the detector.

417 Based on the features of the cosmic muon events observed in this control region, we developed
 418 a cosmic muon veto that uses the fact that for cosmic muons there are usually two legs pointing
 419 in opposite ϕ directions, and both legs generally have rechits or segments in all 4 stations. For
 420 any cluster with 3 or 4 stations (counted if there are ≥ 2 DT Rechits), we look for DT segments
 421 in the opposite ϕ direction ($|\Delta\phi| > 2$). $|\Delta\phi| > 2$ is used because in DT-DT category, clusters
 422 are required to have $|\Delta\phi| < 2$ (required implicitly from $\Delta\phi(\text{cluster}, \text{MET}) < 1$ for both clusters),
 423 so we look for dt segments in the opposite hemisphere that would not belong to the other
 424 cluster. The number of dt segment found in the opposite hemisphere for each cluster is shown
 425 in Fig. 22. Based on the distribution in Fig. 22, we label an event as cosmic muon and veto
 426 the event if a DT segment is found in every station and there are ≥ 6 segments found in the
 427 opposite hemisphere. This veto is 100% efficient in removing all cosmic muon events from the
 428 cosmic muon control region and has little (<0.5%) impact on the signal efficiency.

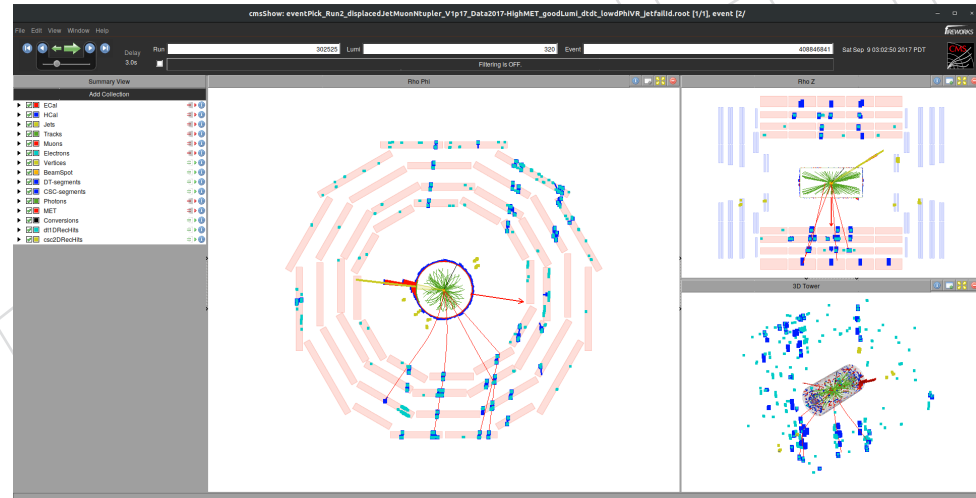


Figure 21: Event display of a cosmic muon event that has DT segments and DT Rechits in opposite ϕ directions. The yellow line is reconstructed jet; yellow dots are CSC Rechits; cyan dots are DT Rechits; dark blue lines are DT segments.

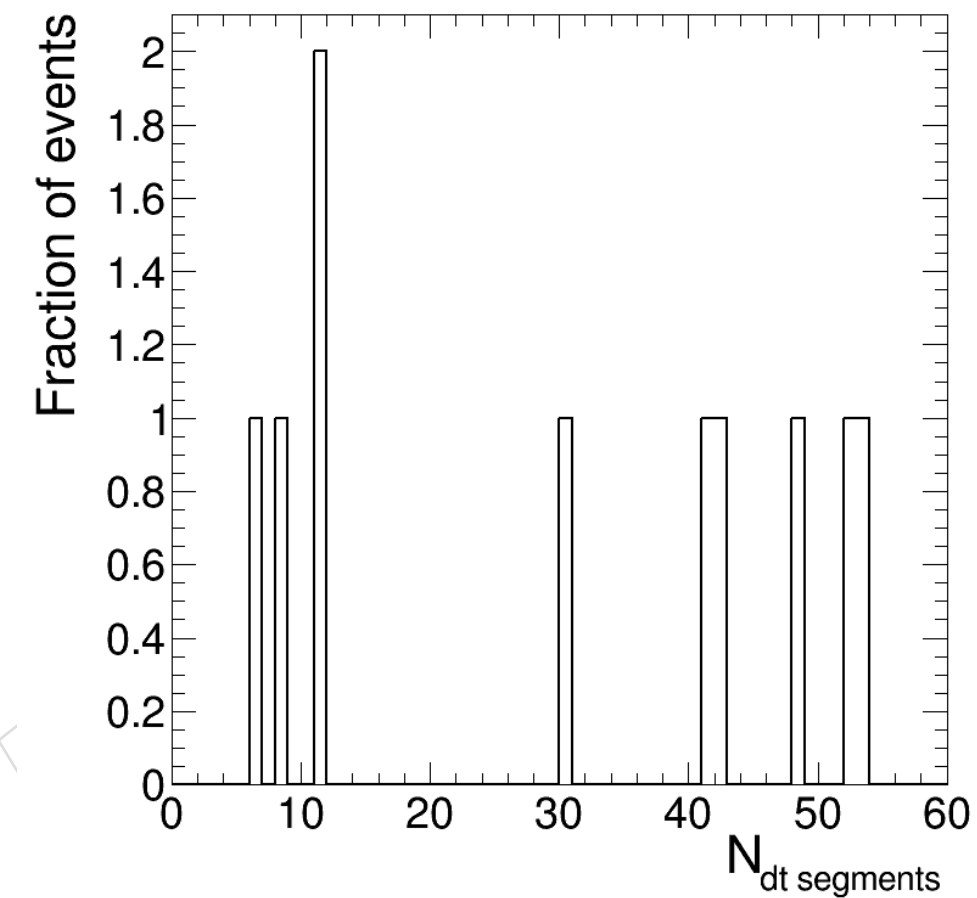


Figure 22: The number of DT segments found in the opposite hemisphere for each cluster found in the cosmic muon enriched region.

429 5.6 DT Instrumental Noise Event

430 We observed a few hundred noise events in the background-enriched control region of the
431 DT-DT category, defined by inverting the $\Delta\phi$ (cluster, MET) requirement for both clusters. The
432 noise events have the same pattern of rechits with a large number of hits in Station 1, wheel
433 -2, Sector 8, 9, and 10. The event displays of three of these noise events are shown in Fig. 23.
434 The events are only observed in 2018D after run number 323400. To remove those events, we
435 develop a dedicated veto by counting the number of DT rechits per sector. The distributions of
436 number of DT rechits per sector for those events are shown in Fig. 24. Based on Fig. 24, we veto
437 an event if in station 1 and wheel -2 it has >50 DT rechits in sector 8, >25 DT rechits in sector
438 9, >10 DT rechits in sector 10, and >120 DT rechits when summed for all three sectors 8, 9, and
439 10. This veto has little impact ($<0.5\%$) on the signal efficiency.

440 Additionally, we have checked if we are affected by the DT noise localized in station 2, observed
441 in the single DT cluster analysis, as detailed in Section 6.9 of AN-21-056 [27]. This noise is
442 only observed in MB2, Wheel 1, ϕ sector 2 and in run number between 275750 and 275950,
443 corresponding to 1.5 fb^{-1} . We observed no such events in both the validation and signal region
444 (events where both clusters have high N_{rechits} are blinded), but we still veto DT clusters in the
445 particular region and runs. For signal, we veto clusters in MB2, Wheel 1 and ϕ sector 2 for
446 1.5 fb^{-1} and do not veto clusters for the rest. This veto has $<0.1\%$ impact on the signal yield
447 given that it only affects 1.5 fb^{-1} of data.

DRAFT

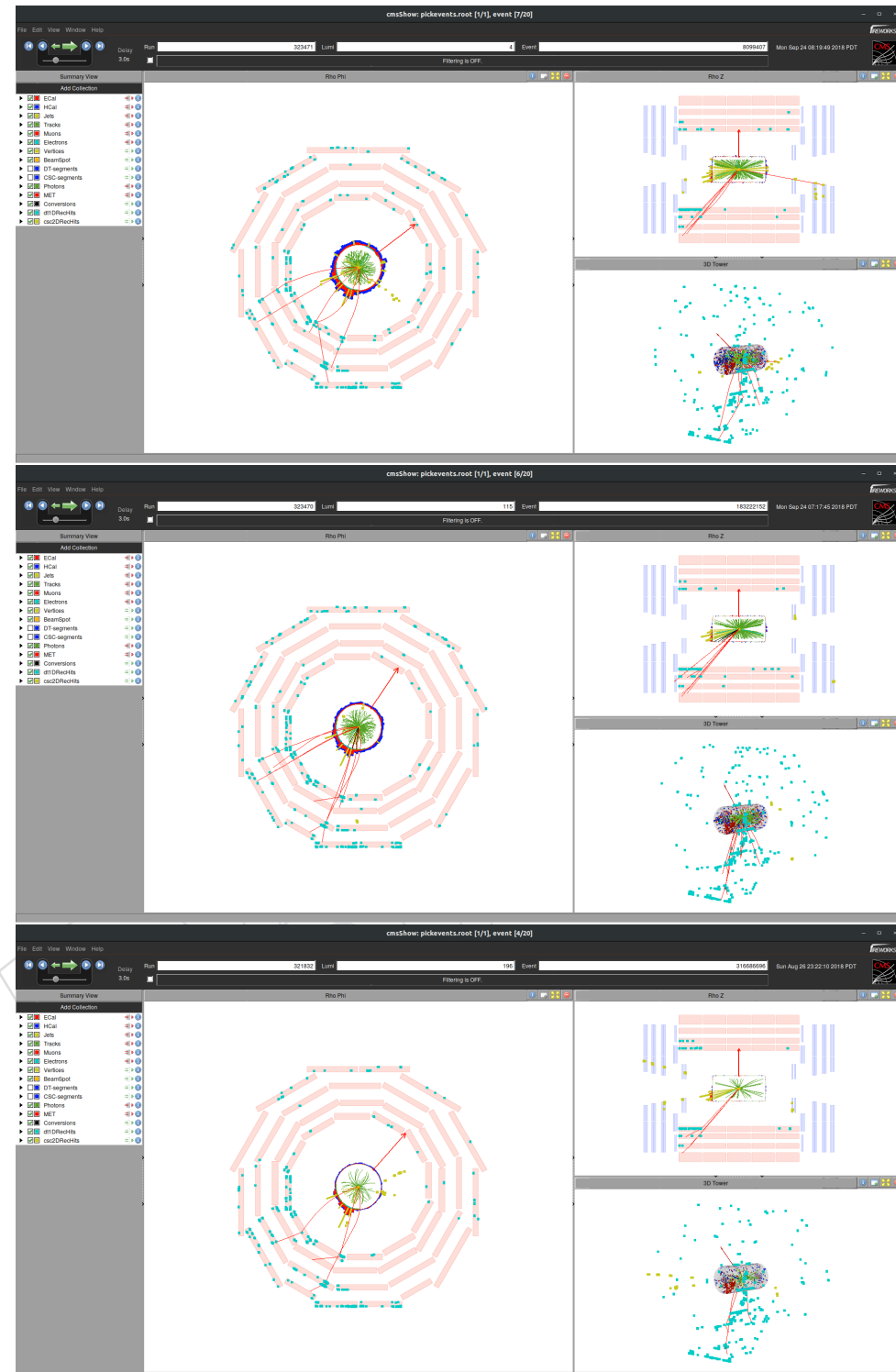


Figure 23: Event display of a DT noise events. The yellow line is reconstructed jet; yellow dots are CSC Rechits; cyan dots are DT Rechits.

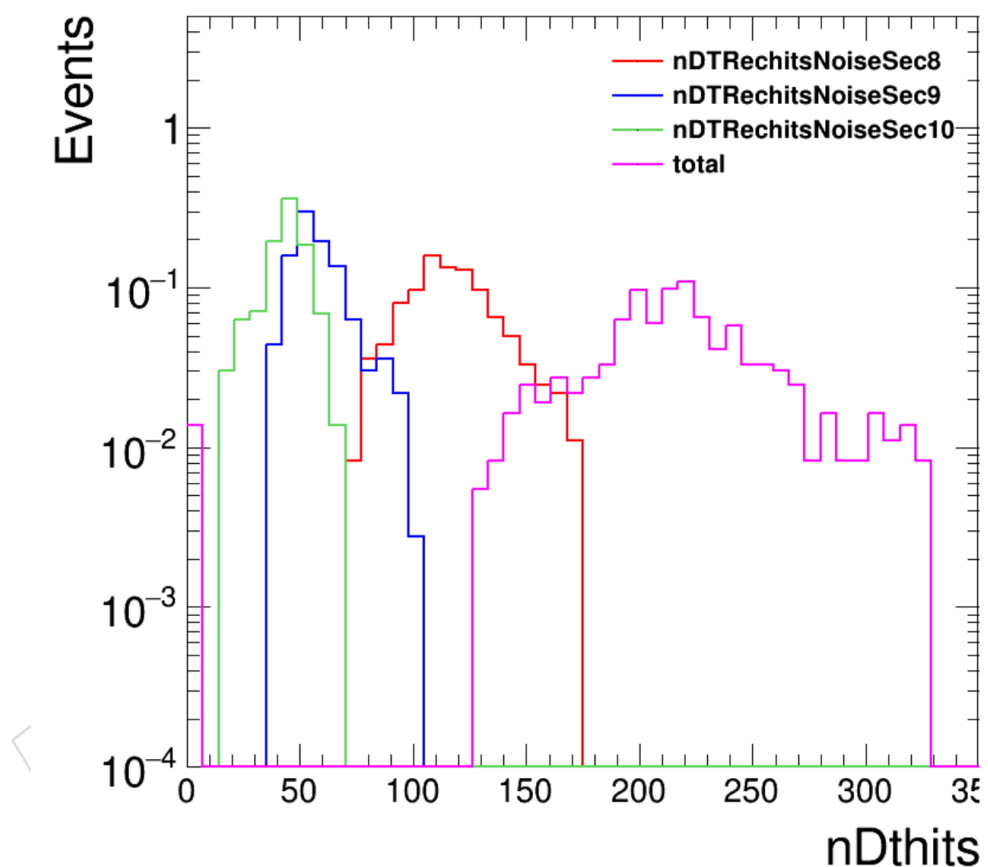


Figure 24: The distribution of the number of DT Rechits in sector 8, 9, 10, or total in Station 1 and Wheel -2.

448 5.7 Signal Region Optimization

449 In addition to the variables mentioned above, the $N_{rechits}$ of the two clusters are used to define
 450 the signal region. The variable is also used to separate the signal-enhanced and background-
 451 enhanced regions used for the background estimation method that will be described in further
 452 detail in Section 6.

453 To optimize for the $N_{rechits}$ cut, we make a projection for the number of background events in
 454 the signal-enhanced bin (A) by fitting the $N_{rechits}$ distribution (per cluster distribution) of data
 455 below 100 with an exponential function. Using the fitted exponential function we calculate
 456 the efficiency of the $N_{rechits}$ cut per cluster as we scan in the cut threshold. We use the $N_{rechits}$
 457 cut efficiency and the number of events with both clusters below 100 Rechits to extrapolate the
 458 expected number of background events with both clusters above each N_{rechit} cut threshold. This
 459 extrapolation using the exponential fit yields greater robustness against statistical fluctuation
 460 due to limited data sample size.

461 When optimizing for the $N_{rechits}$ cut, we remove the ΔR cut between clusters and $N_{hitminstation} / N_{hitmaxstation}$
 462 cut for DT clusters. Without the above cuts removed, we have too few events for optimization.

463 The resulting exponential fits are shown in Fig. 25. For the DT-DT and CSC-CSC categories,
 464 we perform one exponential fit for the $N_{rechits}$ distribution, which is filled for every cluster in
 465 an event. For the DT-CSC category, the $N_{rechits}$ distribution for CSC and DT clusters are plotted
 466 and fitted separately and the $N_{rechits}$ cut efficiency is calculated separately for DT and CSC
 467 clusters.

468 The number of expected background events in the signal bin for the DT-DT category at various
 469 $N_{rechits}$ cut is shown in Table. 9. Based on the table, we choose $N_{rechits} > 80$, since we already
 470 achieve zero background at 80.

Table 9: Background prediction at various $N_{rechits}$ cuts using exponential fit function in the DT-DT category.

N_{rechit} cut	Integral	Eff	EffUp	EffDown	Pred	PredUp	PredDown
80	19	0.03	0.06	0.02	0.02	0.07	0.01
90	19	0.01	0.0237	0.0043	0.0019	0.0106	0.0004
100	19	0.0032	0.0093	0.0011	0.0002	0.0016	0.0000

471 The number of expected background events in the signal bin for the CSC-CSC category at
 472 various $N_{rechits}$ cut is shown in Table. 10. Based on the table, we choose $N_{rechits} > 100$, which is
 473 when the upper bound of the background prediction reduces below 1.

Table 10: Background prediction at various $N_{rechits}$ cuts using exponential fit function in the CSC-CSC category.

N_{rechit} cut	Integral	Eff	EffUp	EffDown	Pred	PredUp	PredDown
80	18	0.21	0.34	0.13	0.78	2.11	0.31
90	18	0.12	0.23	0.07	0.26	0.94	0.08
100	18	0.07	0.15	0.03	0.09	0.42	0.02

474 For DT-CSC category, we choose the same $N_{rechits}$ determined for DT-DT and CSC-CSC cate-
 475 gory. Based on the efficiency extracted from the exponential fit, shown in Fig. 25, the number
 476 of background events is 0.02 in DT-CSC category when the DT cluster threshold is 80 and CSC
 477 cluster threshold is 100.

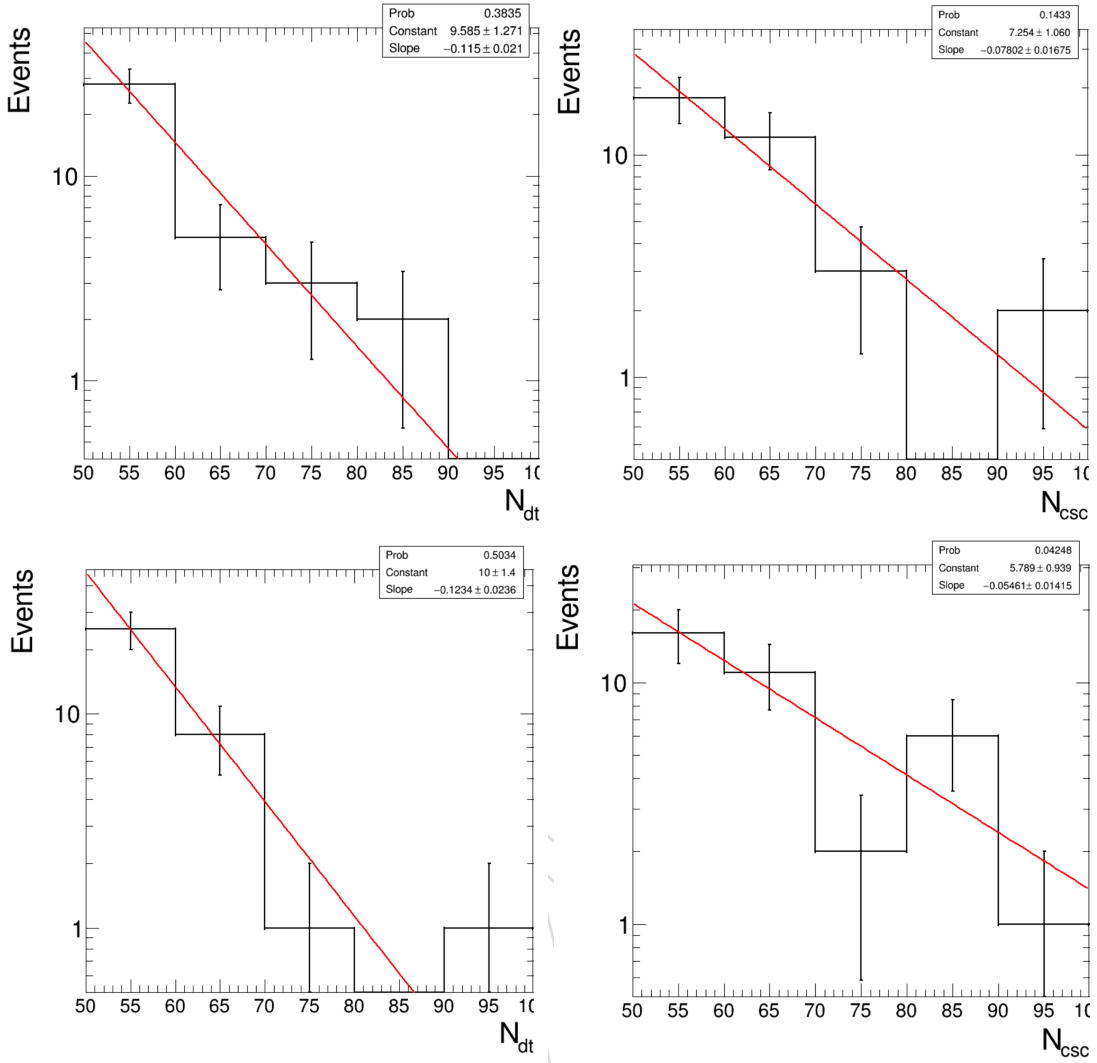


Figure 25: The $N_{rechits}$ distributions and the exponential fits for DT-DT category (Top left), CSC-CSC category (Top right), DT clusters in DT-CSC category (Bottom left), and CSC clusters (Bottom right) in DT-CSC category are shown.

- 478 The data cut flow table is shown in Table 11.
 479 The signal cut flow table for dd decay mode and LLP lifetime of 1 m is shown in Table 12
 480 through Table 15. Additional cut flow tables for other decay modes are shown in Appendix A.

Table 11: Efficiency(%) of each cut for data. Bin A (both clusters passing the $N_{rechits}$ cut) of every category is blinded.

Selection	CSC-CSC		DT-DT		DT-CSC	
	cut eff (%)	N_{events}	cut eff (%)	N_{events}	cut eff (%)	N_{events}
Trigger and MET	100.00	14129474	100.00	14129474	100.00	14129474
MET filters	92.62	13086543	92.62	13086543	92.62	13086543
$N_{jet} \geq 1$	87.32	11426809	87.32	11426809	87.32	11426809
$N_{\text{CSC+DT rings}} \leq 10$	100.00	11426745	100.00	11426745	100.00	11426745
DT noise veto	100.00	11426299	100.00	11426299	100.00	11426299
$N_{cluster} \geq 2$	26.40	29546	17.15	19195	38.05	42594
DT cosmic veto	/	/	83.31	15991	99.19	42251
muon veto	87.94	25984	62.83	10047	76.04	32126
jet veto	22.73	5905	1.62	163	6.41	2060
ME11/MB1 ratio	56.95	3363	49.69	81	51.55	1062
$N_{\text{minstationhits}} / N_{\text{maxstationhits}}$	/	/	44.44	36	61.86	657
time cut	11.33	381	/	/	36.99	243
time spread	34.12	130	/	/	57.61	140
$\Delta\phi(\text{cluster}, \text{MET})$	17.69	23	11.11	4	18.57	26
$\Delta R(\text{cluster1}, \text{cluster2})$	30.43	7	/	/	65.38	17
$N_{rechits}$ cut	0.00	0	0.00	0	0.00	0

Table 12: Signal Efficiency(%) of each cut for twin higgs model, LLP mass 7 GeV, lifetime of 1000 mm and decaying to 2 d quarks. (Cumulative Efficiency for all cuts applied after Trigger and MET cut are calculated with respect to events in acceptance and pass the MET and trigger cut and cut efficiency is calculated with respect to the previous cut. Acceptance is defined as when at least one LLP decays inside CSC.)

Selection	CSC-CSC		DT-DT		DT-CSC	
	cut eff	overall eff	cut eff	overall eff	cut eff	overall eff
acceptance	1.477	1.477	4.509	4.509	4.912	4.912
Trigger and MET	0.498	0.007	0.653	0.029	0.468	0.023
MET filters	98.53	98.53	96.29	96.29	98.14	98.14
$N_{jet} \geq 1$	96.34	94.93	97.40	93.79	96.43	94.64
$N_{\text{CSC+DT rings}} \leq 10$	100.00	94.93	100.00	93.79	100.00	94.64
DT noise veto	100.00	94.93	99.95	93.74	99.83	94.48
$N_{cluster} \geq 2$	41.32	39.22	45.54	42.69	31.36	29.63
DT cosmic veto	/	/	99.87	42.63	99.79	29.57
muon veto	100.00	39.22	98.75	42.10	99.49	29.42
jet veto	90.92	35.66	95.35	40.14	94.92	27.92
ME11/MB1 ratio	96.26	34.33	92.49	37.13	93.22	26.03
$N_{\text{minstationhits}} / N_{\text{maxstationhits}}$	/	/	99.73	37.03	100.00	26.03
time cut	95.57	32.81	/	/	100.00	26.03
time spread	95.14	31.22	/	/	97.54	25.39
$\Delta\phi(\text{cluster}, \text{MET})$	75.81	24	76.91	28.48	86.21	21.89
$\Delta R(\text{cluster1}, \text{cluster2})$	100.00	23.66	/	/	99.63	21.81
$N_{rechits}$ cut	75.46	17.86	66.77	19.02	76.34	16.65

Table 13: Signal Efficiency(%) of each cut for twin higgs model, LLP mass 15 GeV, lifetime of 1000 mm and decaying to 2 d quarks. (Cumulative Efficiency for all cuts applied after Trigger and MET cut are calculated with respect to events in acceptance and pass the MET and trigger cut and cut efficiency is calculated with respect to the previous cut. Acceptance is defined as when at least one LLP decays inside CSC.)

Selection	CSC-CSC		DT-DT		DT-CSC	
	cut eff	overall eff	cut eff	overall eff	cut eff	overall eff
acceptance	2.129	2.129	6.404	6.404	6.504	6.504
Trigger and MET	0.792	0.017	0.869	0.056	0.674	0.044
MET filters	98.43	98.43	96.51	96.51	97.82	97.82
$N_{jet} \geq 1$	95.89	94.39	97.57	94.16	97.27	95.15
$N_{\text{CSC+DT rings}} \leq 10$	100.00	94.39	100.00	94.16	100.00	95.15
DT noise veto	100.00	94.39	100.00	94.16	99.95	95.11
$N_{\text{cluster}} \geq 2$	40.27	38.01	46.03	43.34	37.33	35.51
DT cosmic veto	/	/	99.94	43.32	99.91	35.47
muon veto	100.00	38.01	98.96	42.87	99.59	35.33
jet veto	90.48	34.39	94.38	40.46	94.95	33.55
ME11/MB1 ratio	95.58	32.87	88.99	36.00	93.02	31.20
$N_{\text{minstationhits}} / N_{\text{maxstationhits}}$	/	/	99.92	35.98	100.00	31.20
time cut	99.35	32.66	/	/	100.00	31.20
time spread	96.76	31.60	/	/	98.41	30.71
$\Delta\phi(\text{cluster}, \text{MET})$	88.48	28	88.38	31.80	92.47	28.40
$\Delta R(\text{cluster1}, \text{cluster2})$	99.90	27.93	/	/	100.00	28.40
N_{rechits} cut	81.97	22.90	72.30	22.99	79.86	22.68

Table 14: Signal Efficiency(%) of each cut for twin higgs model, LLP mass 40 GeV, lifetime of 1000 mm and decaying to 2 d quarks. (Cumulative Efficiency for all cuts applied after Trigger and MET cut are calculated with respect to events in acceptance and pass the MET and trigger cut and cut efficiency is calculated with respect to the previous cut. Acceptance is defined as when at least one LLP decays inside CSC.)

Selection	CSC-CSC		DT-DT		DT-CSC	
	cut eff	overall eff	cut eff	overall eff	cut eff	overall eff
acceptance	1.042	1.042	1.203	1.203	1.255	1.255
Trigger and MET	2.693	0.028	4.940	0.059	3.025	0.038
MET filters	96.58	96.58	92.10	92.10	95.25	95.25
$N_{jet} \geq 1$	96.30	93.00	97.86	90.13	96.86	92.26
$N_{\text{CSC+DT rings}} \leq 10$	100.00	93.00	100.00	90.13	100.00	92.26
DT noise veto	99.89	92.90	99.95	90.09	99.88	92.15
$N_{\text{cluster}} \geq 2$	36.69	34.08	37.73	34.00	34.47	31.77
DT cosmic veto	/	/	99.72	33.90	99.38	31.57
muon veto	100.00	34.08	99.31	33.67	99.19	31.31
jet veto	87.21	29.72	93.33	31.42	93.24	29.20
ME11/MB1 ratio	92.51	27.50	89.42	28.10	91.00	26.57
$N_{\text{minstationhits}} / N_{\text{maxstationhits}}$	/	/	100.00	28.10	99.89	26.54
time cut	94.30	25.93	/	/	100.00	26.54
time spread	97.66	25.32	/	/	98.52	26.15
$\Delta\phi(\text{cluster}, \text{MET})$	99.00	25	99.69	28.01	100.00	26.15
$\Delta R(\text{cluster1}, \text{cluster2})$	99.72	25.00	/	/	100.00	26.15
$N_{\text{rechits}} \text{ cut}$	85.63	21.41	75.97	21.28	85.69	22.40

Table 15: Signal Efficiency(%) of each cut for twin higgs model, LLP mass 55 GeV, lifetime of 1000 mm and decaying to 2 d quarks. (Cumulative Efficiency for all cuts applied after Trigger and MET cut are calculated with respect to events in acceptance and pass the MET and trigger cut and cut efficiency is calculated with respect to the previous cut. Acceptance is defined as when at least one LLP decays inside CSC.)

Selection	CSC-CSC		DT-DT		DT-CSC	
	cut eff	overall eff	cut eff	overall eff	cut eff	overall eff
acceptance	0.358	0.358	0.286	0.286	0.230	0.230
Trigger and MET	8.384	0.030	17.338	0.050	12.296	0.028
MET filters	97.38	97.38	91.38	91.38	94.07	94.07
$N_{jet} \geq 1$	97.05	94.51	98.01	89.56	97.63	91.84
$N_{\text{CSC+DT rings}} \leq 10$	100.00	94.51	100.00	89.56	100.00	91.84
DT noise veto	99.96	94.47	99.74	89.33	99.61	91.48
$N_{\text{cluster}} \geq 2$	6.58	6.22	5.27	4.71	12.69	11.61
DT cosmic veto	/	/	99.25	4.67	100.00	11.61
muon veto	100.00	6.22	100.00	4.67	99.40	11.54
jet veto	66.78	4.15	92.00	4.30	88.41	10.20
ME11/MB1 ratio	86.40	3.59	83.59	3.59	72.17	7.36
$N_{\text{minstationhits}} / N_{\text{maxstationhits}}$	/	/	100.00	3.59	100.00	7.36
time cut	58.73	2.11	/	/	100.00	7.36
time spread	95.20	2.00	/	/	97.06	7.15
$\Delta\phi(\text{cluster}, \text{MET})$	97.78	2	100.00	3.59	100.00	7.15
$\Delta R(\text{cluster1}, \text{cluster2})$	100.00	1.96	/	/	100.00	7.15
$N_{\text{rechits}} \text{ cut}$	68.80	1.35	74.55	2.68	88.79	6.34

481 6 Background Estimation

482 After all selections are applied in the previous section, we observe that the main backgrounds
 483 are punchthrough. The punchthrough are from low momentum single particles for CSC clusters
 484 and from higher momentum jets for DT. These background sources are consistent with the
 485 background sources for the single cluster categories. For the CSC clusters, through matching
 486 to generator particles using a combination of minimum bias and W+jets simulation samples,
 487 we find that the dominant source of background clusters are pions with transverse momentum
 488 below 2 GeV. Low momentum kaons also contribute at the 20% level. Such low momentum
 489 particles can be produced by pileup interactions or in the hard interaction and both processes
 490 contribute to the total background.

491 The cluster time, η , and average station distributions for CSC clusters are shown in Fig. 26,
 492 Fig. 27, and Fig. 28. Based on the CSC cluster time distribution, we infer that about one third
 493 contribution is from pileup and two thirds contribution is from the main interaction. The clus-
 494 ter average station distributions for DT clusters, as shown in Fig. 29 peak near average station
 495 1 and 2, indicating that the clusters are from punch-through jets, similar to the single DT clus-
 496 ter category. The cluster average station variable is defined as the average station number for
 497 all stations that contain more than 10 hits. Therefore, it is possible to have average station =
 498 1, while passing the MB1 veto.¹ We only use the average station variable as a check for the
 499 location of clusters in the background. We do not use this variable for selection.

500 Furthermore, the flat distributions of $\Delta\phi$ between the two clusters indicate the clusters in back-
 501 ground events are independent of each other, as shown in Fig. 30. Therefore, we use a data-
 502 driven method similar to the ABCD method to estimate background, where the assumption
 503 that the $N_{rechits}$ of the two background clusters are independent is made.

504 This section describes the data-driven background estimation method and the validation of the
 505 method used in this analysis. We use the ABCD method for DT-CSC category and a slightly
 506 modified ABCD method for the DT-DT and CSC-CSC categories.

507 6.1 Data-Driven Background Estimation Method

508 6.1.1 DT-CSC Category

509 For the DT-CSC category, the standard ABCD method is used to estimate the number of back-
 510 ground events in the signal region. The two variables used to construct the four ABCD bins
 511 are $N_{cscrechits}$ and $N_{dtrechits}$. The ABCD plane is illustrated in Fig. 31, where bin A is the signal
 512 enhanced region, with large values for both $N_{rechits}$. The independence of the two variables in
 513 background are validated using several background-enriched validation regions, detailed in
 514 Section 6.2. The estimation of the number of events in each bin is expressed by Eq. 3 below:

¹An example of such cluster is a cluster with hits 52, 8, 0, 1 in station 1, 2, 3, and 4, respectively. The MB1 veto rejects clusters with more than 90% of hits in station 1, but in this case it is only making up 85% if we count by the number of hits. However the average station is still 1.0 because we are not counting hits in station 2 and 4 as they are below the 10-hit threshold.

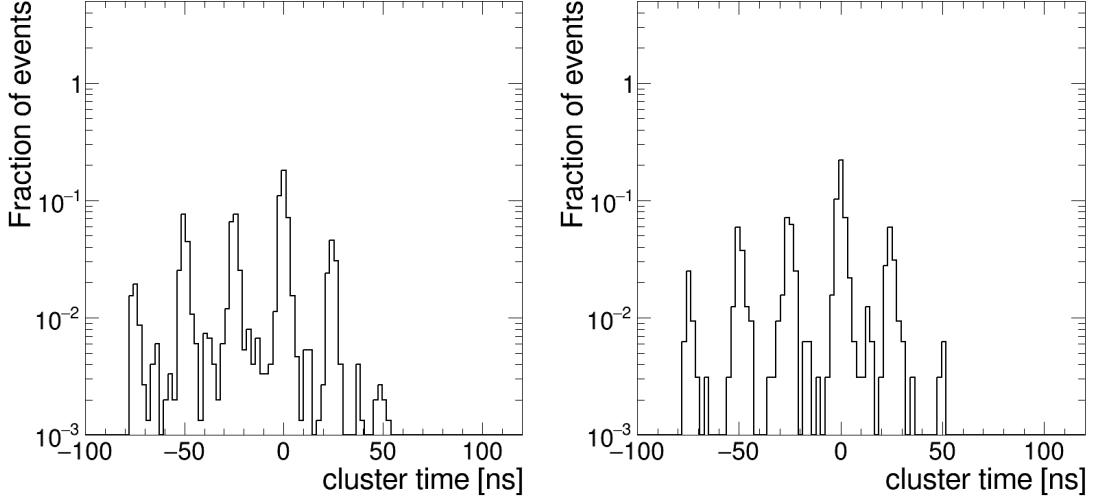


Figure 26: The background distribution for CSC cluster time is shown for the CSC-CSC (left) and DT-CSC (right) category. All cluster-level selections described in the previous sections, except for cluster time and $N_{rechits}$ are applied. Events where both clusters pass the $N_{rechits}$ cut are blinded

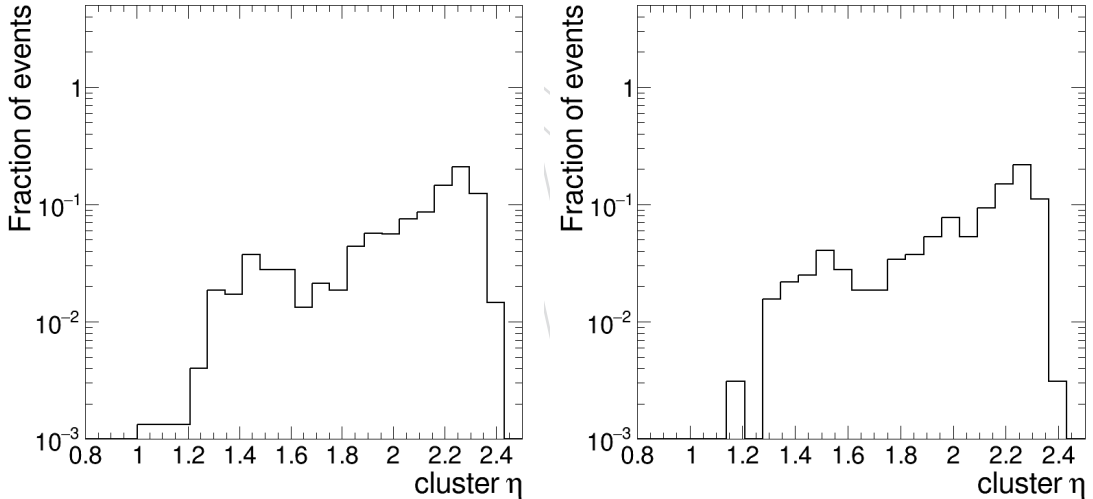


Figure 27: The background distribution for CSC cluster η is shown for the CSC-CSC (left) and DT-CSC (right) category. All cluster-level selections described in the previous sections, except for $N_{rechits}$, $\Delta R(\text{cluster1}, \text{cluster2})$, and $\Delta\phi(\text{cluster}, \text{MET})$ are applied. Events where both clusters pass the $N_{rechits}$ cut are blinded. The removal of $\Delta R(\text{cluster1}, \text{cluster2})$ and $\Delta\phi(\text{cluster}, \text{MET})$ help gain more statistics.

$$\begin{aligned}
 N_A &= c_1 \times c_2 \times Bkg_C + \mu \times SigA \\
 N_B &= c_1 \times Bkg_C + \mu \times SigB \\
 N_C &= Bkg_C + \mu \times SigC \\
 N_D &= c_2 \times Bkg_C + \mu \times SigD,
 \end{aligned} \tag{3}$$

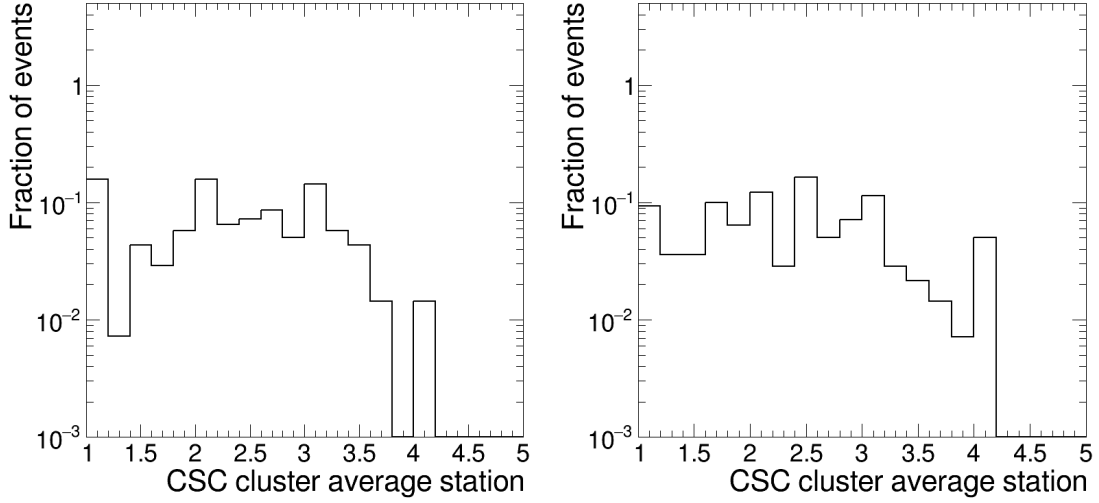


Figure 28: The background distribution for CSC cluster average station is shown for the CSC-CSC (left) and DT-CSC (right) category. All cluster-level selections described in the previous sections, except for $N_{rechits}$, $\Delta R(\text{cluster1}, \text{cluster2})$, and $\Delta\phi(\text{cluster}, \text{MET})$ are applied. Events where both clusters pass the $N_{rechits}$ cut are blinded

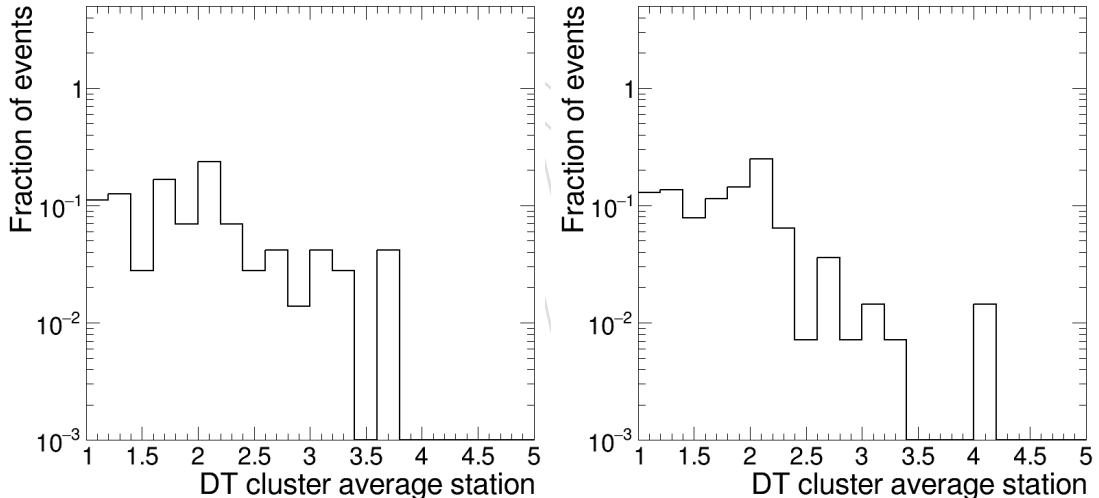


Figure 29: The background distribution for DT cluster average station is shown for the DT-DT (left) and DT-CSC (right) category. All cluster-level selections described in the previous sections, except for $N_{rechits}$, $\Delta R(\text{cluster1}, \text{cluster2})$, and $\Delta\phi(\text{cluster}, \text{MET})$ are applied. Events where both clusters pass the $N_{rechits}$ cut are blinded

515 where:

- 516 • $SigA, SigB, SigC, SigD$ are the number of signal events expected in bin A, B, C, and
517 D, predicted by the signal MC simulation sample,
518 • μ is the signal strength (the parameter of interest of the model),
519 • c_1 is the ratio between D and C for background; c_2 is the ratio between B and C for
520 background (Both c_1 and c_2 are essentially interpreted as nuisance parameters that
521 are unconstrained in the fit), and

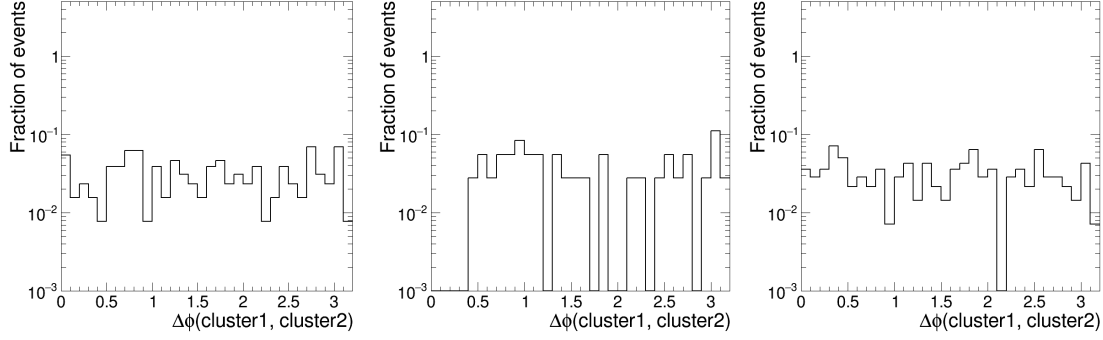


Figure 30: The signal and background distributions for $\Delta\phi(\text{cluster1}, \text{cluster2})$ is shown for the CSC-CSC (left), DT-DT (center), and CSC-DT (right) category. All cluster-level selections described in the previous sections, except for N_{rechits} , $\Delta R(\text{cluster1}, \text{cluster2})$, and $\Delta\phi(\text{cluster}, \text{MET})$ are applied. By applying $\Delta\phi(\text{cluster}, \text{MET})$ cut on both clusters, we implicitly applying a cut on $\Delta\phi(\text{cluster1}, \text{cluster2})$, so we remove this cut to better observe the shape of $\Delta\phi(\text{cluster1}, \text{cluster2})$. The $\Delta\phi(\text{cluster1}, \text{cluster2})$ distribution for DT-DT only has values above 0.4 is because the clustering algorithm cluster all rechits within ΔR of 0.4 and DT clusters in DT-DT are generally close in η , so the separation is mostly in the ϕ direction.

- 522 • Bkg_C is the number of background events in bin C.

The four unknown variables (Bkg_C, c_1, c_2, μ) are extracted from a maximum likelihood fit with the following likelihood expression:

$$L = \prod_i^{ABCD} \text{Pois}(obs_i | N_i) \times \prod_i^{\text{nuisance}} \text{Constraints}(\sigma_j | \hat{\sigma}_j) \quad (4)$$

523 Where obs_i is the number of observed events in each bin and σ_j are the nuisance parameters that
524 capture the impact of systematic uncertainties. All the nuisance parameters are implemented
525 with a log-normal distribution, such that the logarithm of the distribution is a Gaussian con-
526 straint.

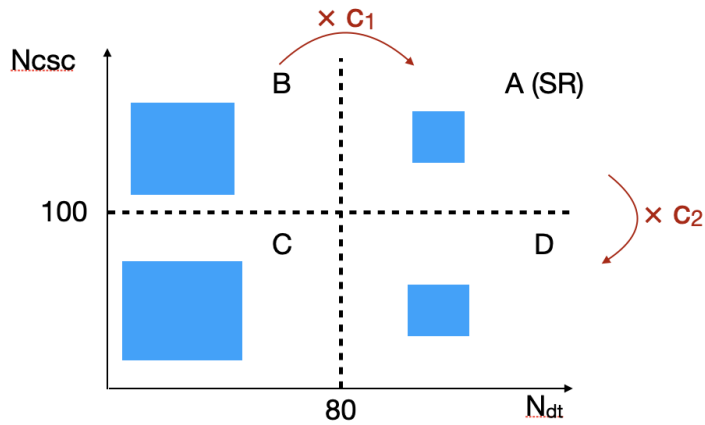


Figure 31: The diagram of the ABCD plane is shown.

527 6.1.2 DT-DT and CSC-CSC Category

528 For the DT-DT and CSC-CSC category, we modify the ABCD method. Because the two clusters
529 are selected with the same requirement, c_1 and c_2 are equal. Therefore, we require only 3 bins

and 3 floating parameters. We count the number of clusters that pass the $N_{rechits}$ cut and the bin with both clusters passing the $N_{rechits}$ cut is the signal region. Fig. 32 illustrates the number of background events expected in each of the 3 bins. The estimation of the number of events in each bin is expressed by Eq. 5 below:

$$\begin{aligned} N_A &= c_1^2 \times Bkg_C + \mu \times SigA \\ N_B &= 2c_1 \times Bkg_C + \mu \times SigB \\ N_C &= Bkg_C + \mu \times SigC, \end{aligned} \quad (5)$$

where:

- $SigA, SigB, SigC$, are the number of signal events expected in bin A, B, and C, predicted by the signal MC simulation sample,
- μ is the signal strength (the parameter of interest of the model),
- c_1 is the ratio between background in B/2 and C (c_1 is interpreted as an unconstrained nuisance parameter in the fit), and
- Bkg_C is the number of background events in bin C.

The three unknown variables (Bkg_C, c_1, μ) are extracted from a maximum likelihood fit with the following likelihood expression:

$$L = \prod_i^{ABC} Pois(obs_i|N_i) \times \prod_i^{nuisance} Constraints(\sigma_j|\hat{\sigma}_j) \quad (6)$$

Where obs_i is the number of observed events in each bin and σ_j are the nuisance parameters that capture the impact of systematic uncertainties.

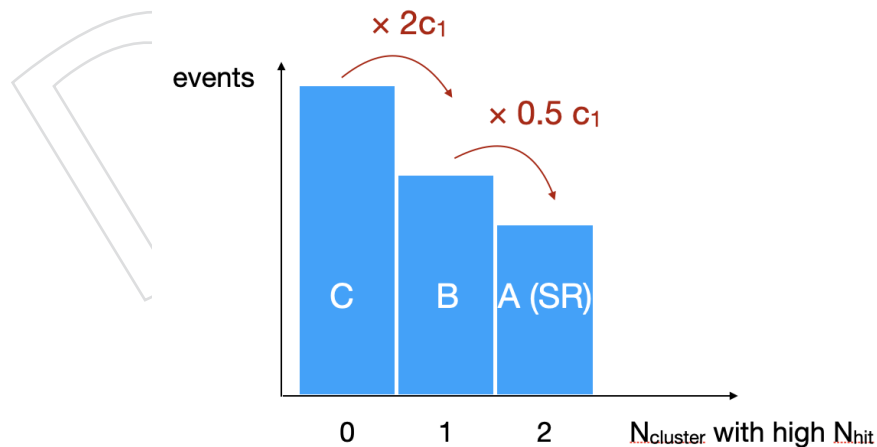


Figure 32: The diagram of the 3 bins is shown.

6.2 Validation of the Estimation Method

Two validation regions are defined in order to validate and test for the accuracy of the background estimation method for each category. The two validation regions are the inverted $N_{rechits}$ validation region and the inverted $\Delta\phi(\text{cluster}, \text{MET})$ validation region. The inverted

547 $N_{rechits}$ validation region is defined by inverting the $N_{rechits}$ requirements for both clusters passing
 548 all other cluster-level selections. The inverted $\Delta\phi(\text{cluster}, \text{MET})$ validation region is de-
 549 fined by inverting the $\Delta\phi(\text{cluster}, \text{MET})$ requirement of both clusters passing all other cluster-
 550 level selections. To probe signal-like events in the inverted $\Delta\phi(\text{cluster}, \text{MET})$ validation region,
 551 we additionally require that $\Delta\phi(\text{cluster1}, \text{cluster2})$ to be < 2 , < 2.2 , and < 2.4 for DT-DT, DT-
 552 CSC, and CSC-CSC category, respectively. This validation region allow us to test for any non-
 553 negligible high $N_{rechits}$ tails that cannot be accessed in the inverted $N_{rechits}$ validation region.

554 6.2.1 Inverted $N_{rechits}$ Validation Region

555 The inverted $N_{rechits}$ validation region is defined by the set of signal selections described in in
 556 Section 5, except the $N_{rechits}$ cut is inverted: $N_{rechits} < 80$ for DT clusters and $N_{rechits} < 100$ for
 557 CSC clusters. We test for all 3 categories in this validation region.

558 In Table 16, 17, and 18, we show the comparison between the prediction and the observation
 559 in the signal-enriched bin A for the 3 categories at various $N_{rechits}$ boundaries. The prediction
 560 agrees well with the observation for all 3 categories, within the statistical uncertainty of the
 561 validation region.

Table 16: Validation of the background estimation method in inverted $N_{rechits}$ validation region for DT-DT category. The uncertainty of the prediction is the statistical uncertainty propogated from bin A and B.

$N_{dtrechits}$	A	B	C	Prediction for A
60	0	2	1	1 ± 1.73
65	0	1	2	0.12 ± 0.27
70	0	1	2	0.12 ± 0.27
75	0	1	2	0.12 ± 0.27

Table 17: Validation of the background estimation method in inverted $N_{rechits}$ validation re-
 gion for CSC-CSC category. The uncertainty of the prediction is the statistical uncertainty pro-
 pogated from bin A and B.

$N_{cscrechits}$	A	B	C	Prediction for A
60	1	5	0	inf
65	1	4	1	4 ± 5.66
70	1	3	2	1.12 ± 1.52
75	1	1	4	0.06 ± 0.13
80	0	2	4	0.25 ± 0.38
85	0	1	5	0.05 ± 0.1
90	0	0	6	0 ± 0
95	0	0	6	0 ± 0

562 6.2.2 Inverted $\Delta\phi(\text{cluster}, \text{MET})$ Validation Region

563 The inverted $\Delta\phi(\text{cluster}, \text{MET})$ validation region is defined by the set of signal selections de-
 564 scribed in in Section 5, except the $\Delta\phi(\text{cluster}, \text{MET})$ cut is inverted: $\Delta\phi(\text{cluster}, \text{MET}) > 1$ for DT
 565 clusters and $\Delta\phi(\text{cluster}, \text{MET}) > 1.2$ for CSC clusters. However, to keep this validation region
 566 more signal-like, we require $\Delta\phi(\text{cluster1}, \text{cluster2}) < 2$ for DT-DT category, $\Delta\phi(\text{cluster1}, \text{cluster2}) < 2.2$
 567 for DT-CSC category, and $\Delta\phi(\text{cluster1}, \text{cluster2}) < 2.4$ for CSC-CSC category. We test for all 3
 568 categories in this validation region.

Table 18: Validation of the background estimation method in inverted $N_{rechits}$ validation region for DT-CSC category. The uncertainty of the prediction is the statistical uncertainty propagated from bin A, B, and C.

$N_{dtrechits}$	$N_{cscrechits}$	A	B	C	D	Prediction for A
60	70	3	2	5	4	1.6 ± 1.56
60	80	1	1	6	6	1.0 ± 1.15
60	90	1	1	6	6	1.0 ± 1.15
70	60	1	9	4	0	0.0 ± 0.0
70	70	1	4	9	0	0.0 ± 0.0
70	80	0	2	11	1	0.18 ± 0.23
70	90	0	2	11	1	0.18 ± 0.23

569 In Table 19, 20, and 21, we show the comparison between the prediction and the observation
 570 in the signal-enriched bin A for each of the 3 categories and at various $N_{rechits}$ boundaries. The
 571 prediction agrees well with the observation for all 3 categories, within the statistical uncertainty
 572 of the validation region.

Table 19: Validation of the background estimation method in inverted $\Delta\phi(\text{cluster}, \text{MET})$ validation region for DT-DT category. The uncertainty of the prediction is the statistical uncertainty propagated from bin A and B.

$N_{dtrechits}$	A	B	C	Prediction for A
60	3	5	4	1.56 ± 1.6
65	1	5	6	1.04 ± 1.02
70	1	3	8	0.28 ± 0.34
75	0	2	10	0.1 ± 0.14
80	0	1	11	0.02 ± 0.05

Table 20: Validation of the background estimation method in inverted $\Delta\phi(\text{cluster}, \text{MET})$ validation region for CSC-CSC category. The uncertainty of the prediction is the statistical uncertainty propagated from bin A and B.

$N_{cscrechits}$	A	B	C	Prediction for A
60	0	6	4	2.25 ± 2.15
65	0	4	6	0.67 ± 0.72
70	0	4	6	0.67 ± 0.72
75	0	3	7	0.32 ± 0.39
80	0	3	7	0.32 ± 0.39
85	0	3	7	0.32 ± 0.39
90	0	3	7	0.32 ± 0.39
95	0	3	7	0.32 ± 0.39
100	0	2	8	0.12 ± 0.18

573 6.3 Expected background

574 We unblind the background-enriched bins (bin B, C, and D) and estimate the number of back-
 575 ground events in bin A from the blinded bin B, C, and D. The predicted background events
 576 is shown in each bin is Table. 22.

Table 21: Validation of the background estimation method in inverted $\Delta\phi$ (cluster, MET) validation region for DT-CSC category. The uncertainty of the prediction is the statistical uncertainty propagated from bin A, B, and C.

$N_{dtrechits}$	$N_{cscrechits}$	A	B	C	D	Prediction for A
60	60	2	7	5	8	11.2 ± 7.66
60	70	0	2	10	10	2.0 ± 1.67
60	80	0	1	11	10	0.91 ± 0.99
60	90	0	1	11	10	0.91 ± 0.99
60	100	0	0	12	10	0.0 ± 0.0
70	60	2	7	8	5	4.38 ± 2.99
70	70	0	2	13	7	1.08 ± 0.91
70	80	0	1	14	7	0.5 ± 0.55
70	90	0	1	14	7	0.5 ± 0.55
70	100	0	0	15	7	0.0 ± 0.0
80	60	0	9	10	3	2.7 ± 1.99
80	70	0	2	17	3	0.35 ± 0.33
80	80	0	1	18	3	0.17 ± 0.2
80	90	0	1	18	3	0.17 ± 0.2
80	100	0	0	19	3	0.0 ± 0.0
90	60	0	9	12	1	0.75 ± 0.82
90	70	0	2	19	1	0.11 ± 0.13
90	80	0	1	20	1	0.05 ± 0.07
90	90	0	1	20	1	0.05 ± 0.07
90	100	0	0	21	1	0.0 ± 0.0

Table 22: Number of background events in the signal region.

	A(prediction)	B	C	D
CSC-CSC	0.04	1	6	/
DT-DT	0.08	1	3	/
DT-CSC	0.14	2	14	1

577 7 Simulation Modeling

578 The validation of the particle shower response of the DT and CSC detectors, as well as the cluster
 579 reconstruction efficiencies are presented in detail in analysis notes [26] and [27]. We use the
 580 same Zmumu skim of the SingleMuon dataset and ZToMuMu Monte Carlo background sam-
 581 ples for this study. The same tag-and-probe method is also used to select for $Z \rightarrow \mu\mu$ events.
 582 However, some of the cluster-level selection requirements and vetos have been loosened for
 583 the two cluster categories. In the following subsections, we present the validation and mea-
 584 surements of the signal efficiencies for selections and vetos that have been slightly loosened for
 585 the two cluster categories.

586 7.1 Simulation Modeling of CSC Clusters

587 In this section we show the simulation modeling of CSC cluster-level variables.

588 In addition to the Tag and Probe selections that select for $Z \rightarrow \mu\mu$ events, a CSC cluster matched
 589 to the probe muon is required to identify the muon brem events. The CSC clusters are selected
 590 with the same set of selections in lined with the cuts used in the analysis, as outlined in Table 23.

Cluster selection
<ul style="list-style-type: none"> • $-5 \text{ ns} < \text{cluster time} < 12.5 \text{ ns}$ • $\text{timeSpread}(\text{cluster}) < 20 \text{ ns}$ • $N_{\text{ME11hits}} / N_{\text{rechits}} < 1$ • $N_{\text{rechits}} \geq 100$ • $\Delta R(\text{cluster}, \text{probemuon}) < 0.4$

Table 23: Cluster selection

591 In this section, we present the measurement of the efficiency of CSC cluster-level selections, in-
 592 cluding the $N_{\text{rechit}} \geq 100$ cut, in-time cut, time spread cut, and $N_{\text{ME11hits}} / N_{\text{rechits}}$ cut. We perform
 593 the measurements on events that pass all selections described above, except for the variables
 594 whose efficiency is being measured. The simulation modeling of the jet veto and muon veto
 595 variable are measured with a different method and discussed in Section 7.3 and 7.4.

596 The distribution of N_{rechits} for CSC clusters are shown in the left plot of Fig. 33. The number
 597 of matched CSC clusters with $N_{\text{rechits}} \geq 100$ with respect to the number of probe muons with
 598 $|\eta|$ between 0.9 and 2.4 is measured to be $2.16\% \pm 0.02\%$ and $2.34\% \pm 0.07\%$ for data and
 599 MC, respectively. The small residual difference indicates that the MC simulation predicts a
 600 slightly larger hit-multiplicity response than the data. Similar to AN-19-154, we found that a 5%
 601 reduction to the hit-multiplicity response in the MC simulation would yield the same fraction
 602 ($2.11\% \pm 0.06\%$) of clusters with $N_{\text{rechits}} \geq 100$ observed in the ZToMuMu control region data.
 603 Implementing the 5% reduction in the hit-multiplicity response would reduce the signal yield
 604 in the signal region by 2.0% in the CSC-CSC and 1.3% in the DT-CSC category. We assign the
 605 difference measured as a source of systematic uncertainty.

606 We repeat the measurement by comparing the combination of data of all 3 years and 2017 MC.
 607 The distributions of N_{rechits} for CSC clusters for data (full run 2) and MC (2017) are shown
 608 in the right plot of Fig. 33. The number of matched CSC clusters with $N_{\text{rechits}} \geq 100$ with
 609 respect to the number of probe muons with $|\eta|$ between 0.9 and 2.4 is measured to be $2.10\% \pm$
 610 0.01% and $2.34\% \pm 0.07\%$ for data and MC, respectively. Similar to the procedure above, we
 611 found that a 5% reduction to the hit-multiplicity response in the MC simulation would yield
 612 the same fraction ($2.11\% \pm 0.06\%$) of clusters with $N_{\text{rechits}} \geq 100$ observed in the ZToMuMu

control region data. Therefore, no additional systematic uncertainty is assigned for signal MC from different years.

The distribution of $N_{\text{ME11hits}} / N_{\text{rechits}}$ for data and MC is shown in Fig. 34. The efficiency of the cut ($N_{\text{ME11hits}} / N_{\text{rechits}} < 1$) is 100% for both data and MC. Since good agreement is observed between 2017 data and MC, no corrections or uncertainties are assigned for MC. Furthermore, the efficiencies from 2016 and 2018 data are found to be in good agreement. The efficiencies are measured to be 100% and $99.98\% \pm 0.01\%$ for 2016 and 2018 data, respectively.

The distributions of the cluster time for data and MC are shown in the left plot in Fig. 35, where the requirement on cluster time is removed. Good agreement is observed between data and MC. The efficiency of the in-time cut ($-5 \text{ ns} < t_{\text{cluster}} < 12.5 \text{ ns}$) is $98.9\% \pm 0.1\%$ and $99.0\% \pm 0.3\%$ for data and MC respectively. We fit both the data and MC distributions with Gaussian function form. The fit to the data distribution resulted in a mean cluster time of $0.01 \pm 0.02 \text{ ns}$ and RMS time of $1.36 \pm 0.01 \text{ ns}$. The fit to the MC distribution resulted in a mean cluster time of $-0.65 \pm 0.04 \text{ ns}$ and RMS time of $1.27 \pm 0.03 \text{ ns}$. To correct for the shift of 0.66 ns in mean, we apply a 0.66 ns shift to the cluster time. However, the correction has no impact on the predicted signal yield in the signal region for most mass/ τ points. The measured efficiency of the in-time cut is $99.5\% \pm 0.1\%$ and $98.8\% \pm 0.1\%$ for 2016 and 2018 data, respectively. Since the larger of the difference between 2016/2018 and 2017 is small, (0.6%), we do not assign any uncertainty.

The distributions of the cluster time spread for data and MC are shown in the right plot in Fig. 35. The distribution is relatively well-modelled and the measured efficiency of the cut is $88.3\% \pm 0.3\%$ and $91.7\% \pm 0.7\%$ for data and MC respectively. The 3.7% difference observed between data and MC is assigned as a systematic uncertainty per cluster.

The efficiency of the time spread cut is measured to be $90.2\% \pm 0.4\%$ and $84.8\% \pm 0.3\%$ for 2016 and 2018 data, respectively. The larger difference from 2017 data, 3.9% is taken as the systematic uncertainty per cluster.

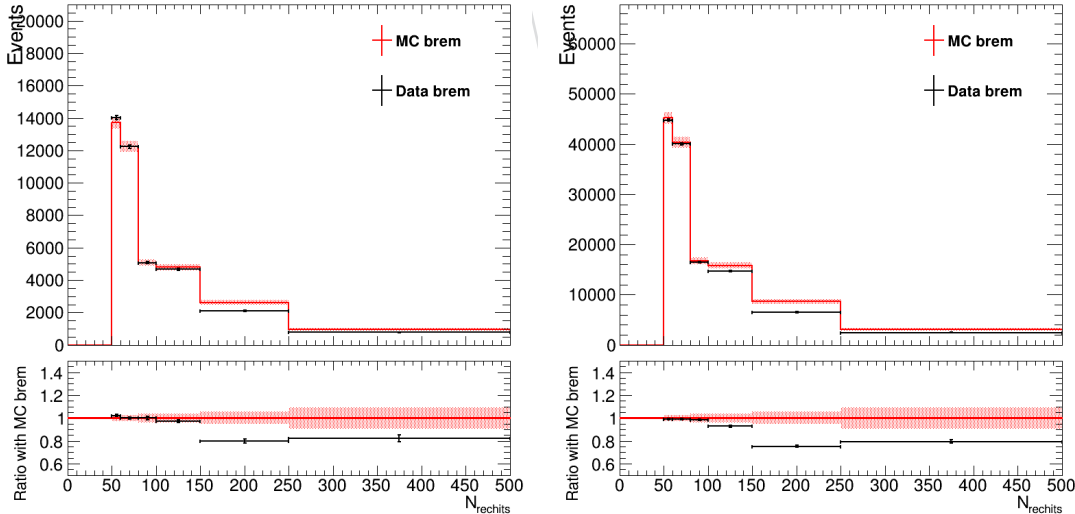


Figure 33: The CSC cluster N_{rechits} distributions for MC and data are shown. The left plot shows the comparison between 2017 MC and 2017 data, while the right plot shows the comparison between 2017 MC and data from full run 2.

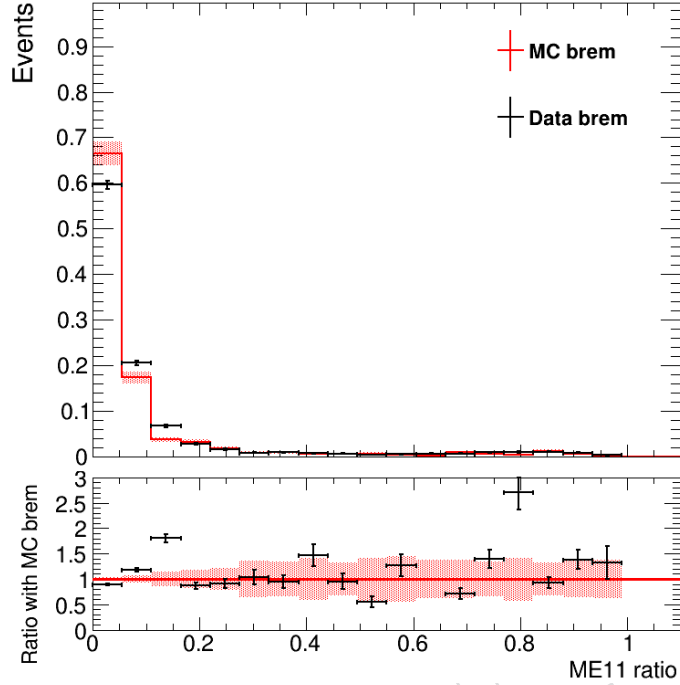


Figure 34: The CSC cluster $N_{\text{ME11hits}} / N_{\text{rechits}}$ distributions for MC and data are shown.

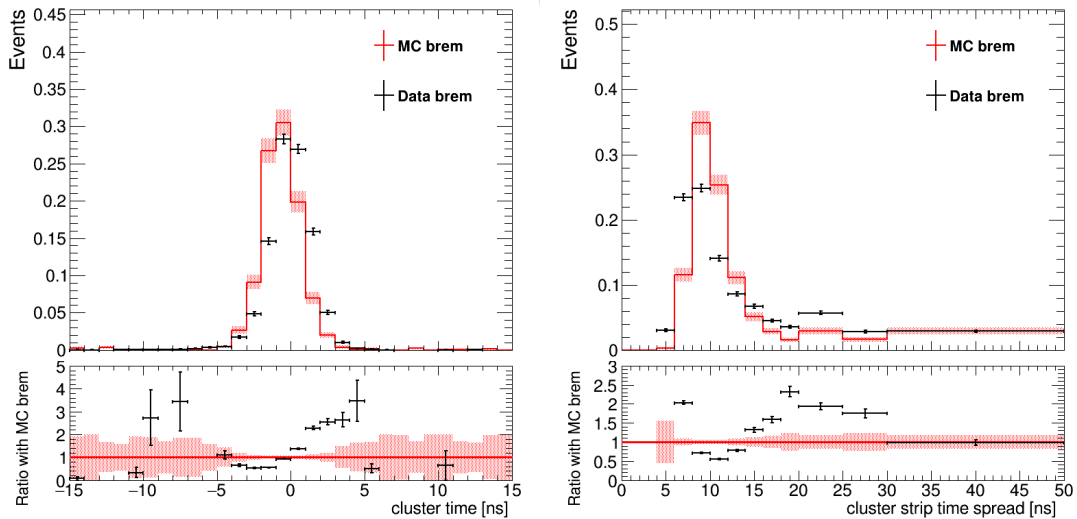


Figure 35: The CSC cluster time(Left) and time spread (Right) distributions for MC and data.

639 7.2 Simulation Modeling of DT Clusters

640 In this section we show the simulation modeling of DT cluster-level variables.

641 In addition to the Tag and Probe selections that select for $Z \rightarrow \mu\mu$ events, a DT cluster matched
642 to the probe muon is required to identify the muon brem events. The DT clusters are selected
643 with the same set of selections in lined with the cuts used in the analysis, as outlined in Table 24.

Cluster selection
• $N_{MB1\text{hits}}/N_{\text{rechits}} < 0.9$
• $N_{\text{rechits}} \geq 80$
• $\Delta R(\text{cluster}, \text{probemuon}) < 0.4$

Table 24: Cluster selection

644 We measure the efficiency of DT cluster-level selections, including the $N_{\text{rechit}} \geq 80$ cut and
645 $N_{MB1\text{hits}}/N_{\text{rechits}}$ cut. We perform the measurements on events that pass all selections described
646 above, except for the variables whose efficiency is being measured. The simulation modeling of
647 the jet veto and muon veto are measured with a different method and discussed in Section 7.3
648 and 7.4.

649 The distribution of N_{rechits} for DT clusters are shown in the left plot of Fig. 36. A clear dis-
650 crepancy is observed been data and MC. We correct for the discrepancy by generating extra
651 noise hits that were mismodeled in MC simulations. For each DT layer (44 layers in total),
652 we generate an extra noise hit with a given probability and add the number of noise hits to
653 the total number of hits per cluster. To determine this probability, we scanned the probability
654 from 1% to 8% with a step size of 1% and found that a probability of 3% resulted in the mini-
655 mum $\chi^2/NDF = 36.85/5$ between data and MC. The distributions after adding the noise hits
656 with a probability of 3% are shown in the right plot of Fig. 36, where much better agreement is
657 observed.

658 The remaining discrepancy observed is quantified by measuring the efficiency of the $N_{\text{rechits}} \geq$
659 80 cut for MC and data. The measured efficiency is $13.4\% \pm 0.2\%$ and $15.5\% \pm 0.5\%$ for data
660 and MC, respectively. Similar to CSC clusters, we correct for the hit-multiplicity response in
661 MC simulation, and found that a 5% correction shifting the threshold from 80 to 84 would
662 yield the same fraction($13.3\% \pm 0.5\%$) of clusters with $N_{\text{rechits}} \geq 80$ observed in the ZToMuMu
663 control region data.

664 For signal, we implement the noise generating procedure for the signal in the signal region,
665 as it impacts the signal yield in all bins in the DT-CSC and DT-DT category. The correction
666 increases the signal yield by 1-2% for bin A (signal-enriched region) in DT-DT category and
667 0.5-1% in DT-CSC category.

668 Furthermore, we implement the correction in the hit-multiplicity response (shift the N_{rechits}
669 cut threshold from 80 to 84) would reduce the signal yield in the signal region by 3.2% and
670 1.1% in the DT-DT and DT-CSC category, respectively. Therefore, we assign a 3.2% systematic
671 uncertainty in DT-DT category and 1.1% uncertainty in DT-CSC category.

672 Finally, we observed good agreement between data from different years. The efficiencies of the
673 $N_{\text{rechits}} \geq 80$ cut are $13.2\% \pm 0.2\%$ and $13.7\% \pm 0.2\%$ for data from 2016 and 2018, respectively.

674 The distribution of $N_{MB1\text{hits}}/N_{\text{rechits}}$ for data and MC is shown in Fig. 37. The efficiency of the
675 cut ($N_{MB1\text{hits}}/N_{\text{rechits}} < 0.9$) is $94.0\% \pm 0.3\%$ and $93.9\% \pm 0.8\%$ for data and MC respectively.
676 Good agreement is observed between data and MC, so no corrections or uncertainties are as-

677 signed for MC. Furthermore, we observed good agreement between data from different years.
 678 The efficiencies are $94.2\% \pm 0.3\%$ and $93.6\% \pm 0.2\%$ for data from 2016 and 2018, respectively.

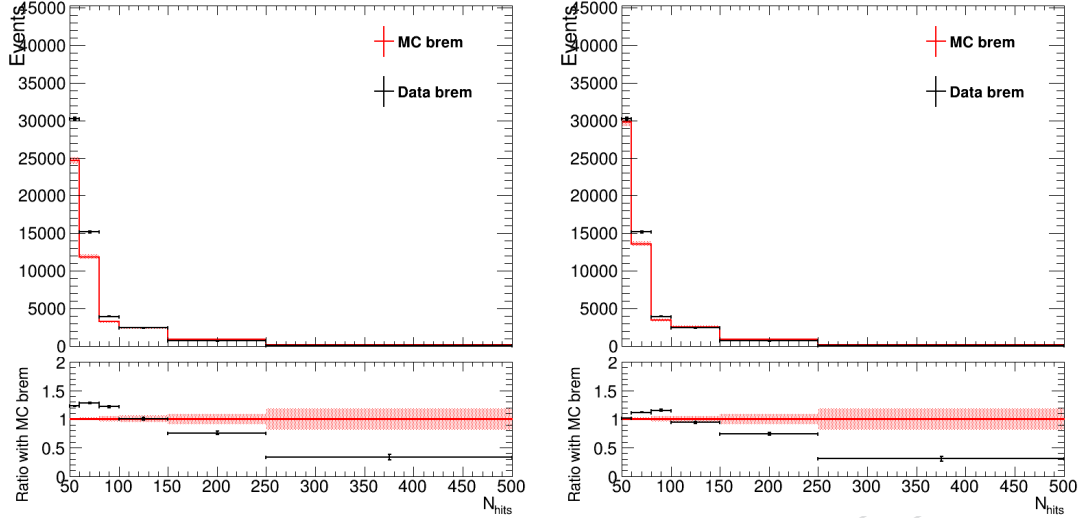


Figure 36: The $N_{rechits}$ distributions of before (Left) and after (Right) the corrections.

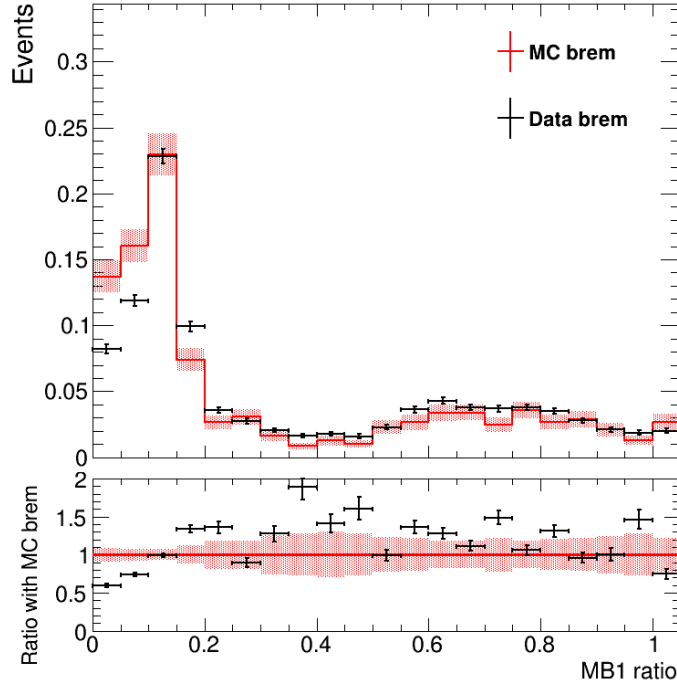


Figure 37: The DT cluster $N_{MB1hits} / N_{rechits}$ distributions for MC and data are shown.

679 7.3 Jet Veto Efficiency

680 The jet veto inefficiency for signal events come from the accidental matching of the signal cluster
 681 to either pileup jets or jets from the decay of the other LLP that decays close to the interaction
 682 point. The composition of the two components depend on the mass and $c\tau$ of the signal
 683 model, which determines how likely that the other LLP decays close to the interaction point
 684 and the topology of the two LLPs. The accidental matching to the other LLP only dominates

for $c\tau = 100$ mm. For all the other signal models, the pileup jet matching dominates the jet veto inefficiency.

To validate that the jet veto efficiency is well-modelled in simulation, in case of the mismodelling of the pileup jet distributions, we measure the jet veto efficiency in simulation and data in the ZToMuMu control region, where the events are required to pass the tag and probe selections described in AN [26], but no clusters are required. To simulate the accidental matching of the clusters to pileup jets, for each event, we randomly select a (η, ϕ) position from the signal cluster distribution that pass all selections but the jet veto, and check if there exists a geomtrically matched jet with $p_T > 30$ or 50 GeV within a ΔR cone of 0.4 for CSC and DT clusters, respectively.

The measured probability that the randomly selected position is not matched to a jet is the jet veto efficiency. The measured jet veto efficiency for CSC clusters is $99.17\% \pm 0.01\%$ and $99.55\% \pm 0.01\%$ for 2017 data and MC respectively. The measured jet veto efficiency for CSC clusters is $99.17\% \pm 0.01\%$ and $99.19\% \pm 0.01\%$ for data from 2016 and 2018, respectively. The measured jet veto efficiency for DT clusters is $99.33\% \pm 0.01\%$ and $99.72\% \pm 0.01\%$ for 2017 data and MC respectively. The measured jet veto efficiency for DT clusters is $99.32\% \pm 0.01\%$ and $99.34\% \pm 0.01\%$ for data from 2016 and 2018, respectively. Since measured difference between data and MC is small ($< 1\%$), and we observed good agreement between data from different years, we do not apply any signal uncertainty or corrections.

The jet veto efficiency with respect to the number of primary vertices is measured in the control region for data and MC as well as signal, where we require the other LLP to decay outside the calorimeters ($R > 300$ cm OR $Z > 600$ cm), as shown in Fig. 38. The measurements in all three regions show good agreement.

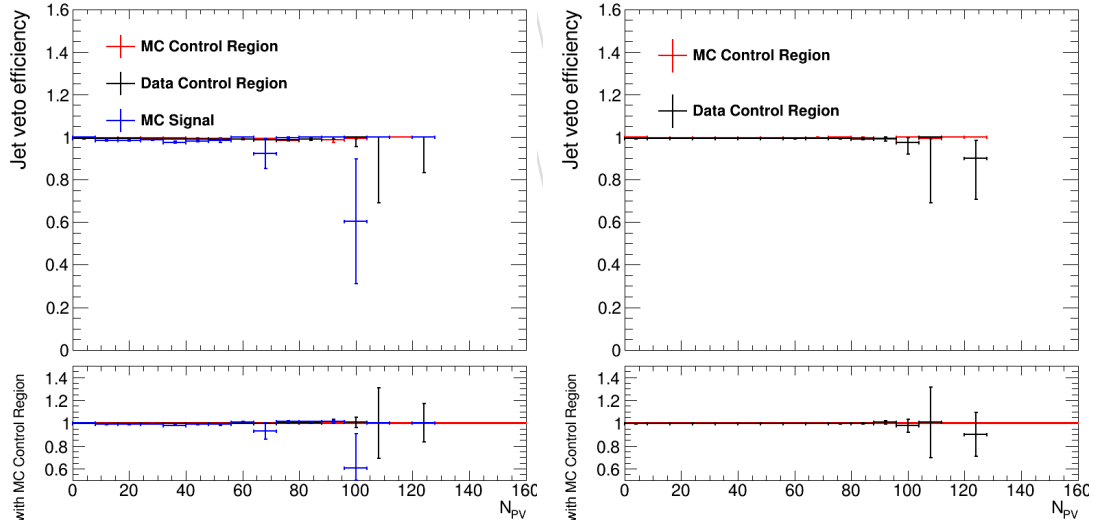


Figure 38: The jet veto efficiency measured in data/MC control region and the signal region for CSC (left) and DT (right) clusters.

7.4 Muon Veto Efficiency

Similar to the jet veto, the muon veto inefficiency for signal events come from the accidental matching of the signal cluster to muons.

To validate that the muon veto efficiency is well-modelled in simulation, we measure the muon veto efficiency in simulation and data in the ZToMuMu control region, where the events are

713 required to pass the tag and probe selections described in AN [26], but no clusters are required.
714 To simulate the accidental matching of the clusters to muons, for each event, we randomly
715 select a (η, ϕ) position from the signal cluster distribution that pass all selections but the muon
716 veto, and check if there exists a geometrically matched loose ID (global) muon with $p_T > 10$
717 (30) GeV within a ΔR cone of 0.4 for DT(CSC) clusters, respectively. Muons from the Z decays
718 are removed and not considered in matching.

719 Since there are very rarely extra muons passing loose ID (for DT) or global muons (for CSC),
720 the measured muon veto efficiency is 99.9-100% for data from all 3 years and MC for both DT
721 and CSC clusters. This agrees with the 99%-100% that we have observed for signal events.

722 Therefore, we do not apply any signal uncertainty or corrections.

DRAFT

723 **8 Systematic uncertainties**

724 **8.1 Background Uncertainties**

725 The background prediction uncertainty is dominated by the statistical uncertainty in the background-
726 dominated bins B, C, and D (only for DT-CSC category). As mentioned in Section 6, we ob-
727 served agreement between the prediction and observed values in all of the validation regions,
728 and therefore assign no additional background systematic uncertainty.

729 **8.2 Signal Uncertainties**

730 The systematic uncertainties of the signals in each bin of ABCD plane are described in this
731 section. For the gluon fusion production, the uncertainty is dominated by the higgs p_T shape
732 uncertainty, while for the other production modes, the uncertainty is dominated by the CSC
733 cluster simulation modelling uncertainty. The cluster modelling uncertainties and MC statistics
734 uncertainties are uncorrelated across the 3 categories, while all other uncertainties are fully
735 correlated across the categories.

736 **8.2.1 CSC and DT Rechit cluster modelling**

737 This uncertainty includes uncertainties measured from the cluster efficiency for both CSC and
738 DT clusters, CSC and DT cluster jet veto efficiency. The detailed measurement procedure of the
739 efficiencies and uncertainties are performed in a muon bremsstrahlung control region, described
740 in Section 7.

741 **8.2.2 CSC Readout**

742 For the CSC chamber to initiate readout in data, there is a requirement to form a pre-trigger in
743 coincidence with L1Accept. The pre-trigger is generated when there are at least two compara-
744 tor (i.e., trigger-level) hits at different CSC layers and matching a given pre-defined pattern
745 of hits. The requirement of pre-triggers for readout has been switched off in simulation. This
746 discrepancy has a few effects on the signal yield prediction.

747 The clustering algorithm overestimates the number of CSC Rechits in signal cluster by includ-
748 ing Rechits in chambers with a small number of hits that did not satisfy the readout requirement
749 in data. We approximate the CSC readout requirement for signal samples by only counting Re-
750 chits if the chamber contains ≥ 6 hits. This requirement resulted in a small ($< 0.1\%$) decrease
751 to the signal efficiency. Since the size of this effect is negligible, we do not propagate any un-
752 certainty for this effect.

753 **8.2.3 Pileup reweight**

754 The size of the pileup uncertainty is summarized in Table. 25 and estimated to be about 1%
755 for all signal models in the signal region and are independent across the models. The pileup
756 reweight uncertainty is estimated by varying the the pp inelastic cross section up and down
757 one standard deviation and measuring the resulting change in the signal yield predicted in the
758 signal region.

759 **8.2.4 Luminosity**

760 A 1.8% luminosity uncertainty is assigned for the sum of all 3 years, following the recommen-
761 dation from the Luminosity Physics Object Group[42].

Table 25: Pileup uncertainty in each bin of ABCD plane.

Uncertainty	A	B	C	D
DT-DT	1.30%	1.52%	7.83%	
CSC-CSC	1.02%	1.44%	1.83%	
DT-CSC	1.07%	1.87%	1.83%	2.53%

8.2.5 Jet Energy Scale

The size of this uncertainty is about 2-3% for all signal models in bin A (signal bin), as summarized in Table. 26. The jet energy scale uncertainty is assigned based on the official recommendation [35]. This uncertainty affects the trigger efficiency (MET-based), the efficiency of the MET cut, and the efficiency of the leading jet selection. To estimate the impact of the jet energy scale uncertainty, we vary the p_T of all jets considered up and down by 1σ , and also propagate the effect to the missing transverse momentum. The resulting variation in signal yield in the signal region is propagated as the jet energy scale uncertainty.

Table 26: Jet energy scale uncertainty in each bin of ABCD plane.

Uncertainty	A	B	C	D
DT-DT	2.66%	3.55%	7.90%	
CSC-CSC	3.51%	5.73%	4.70%	
DT-CSC	3.32%	3.06%	12.11%	3.90%

769

8.2.6 Signal Cross Section

The theory uncertainty on the overall signal cross section for each production mode is taken from the LHC Higgs Cross Section working group yellow report 4 [30]. The uncertainty for ggH, VBF, WH, qqZH, ggZH, and ttH are: 6.7%(-) 4.6%(+), 0.3%(-) 0.4%(+), 0.7%(-) 0.5%(+), 0.6%(-) 0.5%(+), 25.1%(-) 18.9%(+), and 9.2%(-) 5.8%(+), respectively.

8.2.7 Parton Density Functions and Strong Coupling Constant

The effect of PDF uncertainty and strong coupling constant uncertainty on the overall signal yield for each production mode is taken from the LHC Higgs Cross Section working group yellow report 4 [30]. The uncertainty for ggH, VBF, WH, qqZH, ggZH, and ttH are: 3.2%, 2.1%, 1.9%, 1.9%, 2.4%, and 3.6%, respectively.

8.2.8 Higgs p_T Reweighting for Gluon Fusion Production

The higgs p_T reweight uncertainty is calculated by adjusting the renormalization and factorization scale by a factor of 0.5 and 2 and re-evaluating the signal region yield with respect to the nominal signal yield. The shape of the higgs p_T distribution with different renormalization and factorization scale is shown in Fig. 39. A downward uncertainty of 20% is calculated by summing the uncertainties from the 3 variations where the scales are adjusted by a factor 0.5 and an upward uncertainty of 13% is calculated by summing the uncertainties from the 3 variations where the scales are adjusted by a factor 2.0. The uncertainty calculated from the sum of all signal models is used, as summarized in Table. 27.

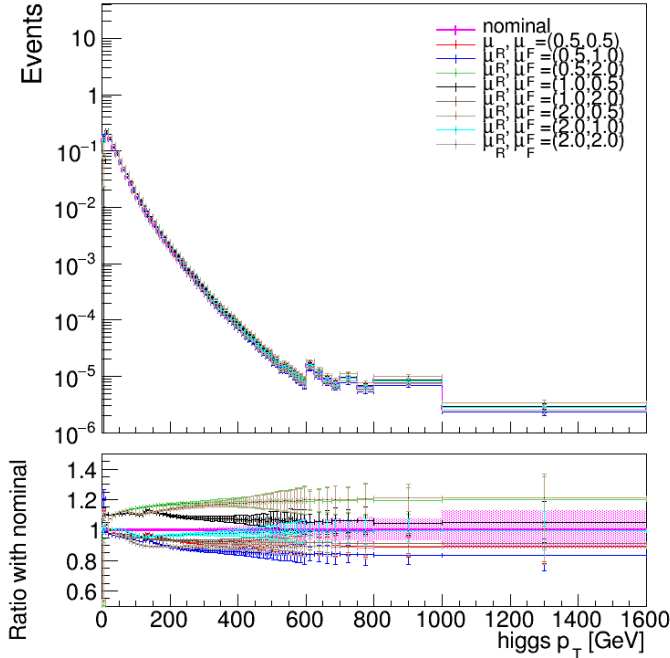


Figure 39: The higgs p_T shape calculated from different renormalization and factorization scale.

8.2.9 Higgs p_T Uncertainty for VBF, VH, and ttH

For the sub-dominant production modes, including VBF, VH, and ttH, the higgs p_T uncertainty is calculated by adjusting the renormalization and factorization scale for the sample by a factor of 0.5 and 2 and re-evaluating the signal region yield with respect to the nominal signal yield. The uncertainty calculated from the 6 variations for all signal model is summed in quadrature, as summarized in Table. 27. This systematic uncertainty is assigned for each production mode independently and are correlated across the 3 categories.

Table 27: Higgs p_T uncertainty in each bin of ABCD plane.

DT-DT													
ggH		VBF		WH		qqZH		ggZH		ttH			
	Up	Down	Up	Down	Up	Down	Up	Down	Up	Down	Up	Down	
A	13.42%	20.74%	1.02%	1.54%	0.99%	2.41%	2.65%	6.74%	2.29%	4.26%	0.24%	1.44 %	
B	13.43%	20.77%	2.4%	3.32%	4.57%	14.52%	2.2%	7.71%	3.96%	24.33%	0.48%	0.76 %	
C	13.36%	20.61%	4.85%	8.23%	4.78%	10.78%	9.12%	33.48%	0.75%	20.63%	1.66%	40.21 %	
CSC-CSC													
ggH		VBF		WH		qqZH		ggZH		ttH			
	Up	Down	Up	Down	Up	Down	Up	Down	Up	Down	Up	Down	
A	13.39%	20.66%	0.84%	3.64%	1.62%	9.9%	1.35%	6.58%	1.99%	11.4%	2.45%	9.19 %	
B	13.4%	20.69%	2.41%	4.84%	1.32%	5.25%	1.3%	5.5%	1.34%	5.01%	9.76%	28.77 %	
C	13.41%	20.69%	1.61%	8.11%	8.54%	38.33%	12.21%	30.26%	13.75%	28.73%	16.91%	36.74 %	
DT-CSC													
ggH		VBF		WH		qqZH		ggZH		ttH			
	Up	Down	Up	Down	Up	Down	Up	Down	Up	Down	Up	Down	
A	13.4%	20.71%	0.96%	1.52%	1.02%	7.72%	0.49%	18.75%	1.94%	9.95%	1.07%	0.92 %	
B	13.4%	20.66%	0.71%	3.06%	3.13%	11.23%	1.07%	6.29%	1.44%	9.98%	6.35%	28.68 %	
C	13.45%	20.84%	3.51%	10.45%	13.62%	56.32%	9.34%	27.84%	27.61%	83.19%	12.91%	23.67 %	
D	13.43%	20.76%	1.09%	2.08%	5.41%	20.4%	2.51%	7.31%	7.53%	14.95%	2.87%	8.44 %	

796 8.2.10 MC Statistics

797 The size of this uncertainty depends on the signal model acceptance. The uncertainty is less
798 than 5% in bin A for signal models with lifetimes around 1 meter, but increases to 20% for
799 signal models with much smaller lifetimes, where the acceptance is much smaller.

800 The uncertainty in the background enriched bins (bin B, C, and D) have large uncertainty of
801 about 10-28%, since there are less signal events in the background enriched regions.

DRAFT

802 9 Results for the two cluster categories

803 We present results of the search in the two cluster categories in this section.

804 9.1 Signal Prediction

805 The expected number of signal events for LLPs decaying to 2 d quarks, 2 b quarks, and 2 τ
 806 leptons, assuming $\text{BR}(\text{H} \rightarrow \text{ss}) = 1\%$ for several LLP masses and proper lifetime $c\tau$, are summa-
 807 rized in Table. 28, Table. 30, and Table. 29, respectively. The expected number of signal events
 808 for 0.4 GeV, 1 GeV, and 1.5 GeV LLPs, assuming $\text{BR}(\text{H} \rightarrow \text{ss}) = 1\%$ for several LLP decay modes
 809 and proper lifetime $c\tau$, are summarized in Table. 31, Table. 32, and Table. 33, respectively.

810 There are more than 20 events in the 3 double cluster categories for the most sensitive signal
 811 points at $c\tau$ around 1 meter, for the heavier mass points and around 10-40mm for the lighter
 812 LLPs. Therefore, it is expected that we are sensitive to exclusion limits at branching ratio below
 813 one percent.

Table 28: Signal yield in the signal region in binA, for LLP decaying to 2 d quarks and various
 LLP masses, assuming $\text{BR}(\text{H} \rightarrow \text{ss}) = 1\%$.

CSC-CSC					
LLP mass / $c\tau$	100 mm	500 mm	1000 mm	10000 mm	100000 mm
3 GeV	6.4	1.1	/	/	/
7 GeV	4.2	/	1.5	0.1	0.0
15 GeV	0.5	/	4.7	0.1	0.0
40 GeV	0.0	/	6.6	0.9	0.0
55 GeV	0.0	/	0.5	0.2	0.0
DT-DT					
LLP mass / $c\tau$	100 mm	500 mm	1000 mm	10000 mm	100000 mm
3 GeV	14.1	3.5	/	/	/
7 GeV	4.9	/	4.9	0.1	0.0
15 GeV	0.3	/	11.7	0.4	0.0
40 GeV	0.0	/	11.4	2.9	0.1
55 GeV	0.0	/	1.2	1.5	0.1
DT-CSC					
LLP mass / $c\tau$	100 mm	500 mm	1000 mm	10000 mm	100000 mm
3 GeV	9.8	3.5	/	/	/
7 GeV	3.8	/	4.3	0.1	0.0
15 GeV	0.3	/	11.1	0.4	0.0
40 GeV	0.0	/	8.8	2.3	0.1
55 GeV	0.0	/	2.1	1.8	0.1

814 9.2 Signal injection test

815 We perform the signal injection test on a few test signal samples for bb decay mode for 15 GeV
 816 and 0.5 m lifetime LLP, 15 GeV and 1m lifetime LLP, and 40 GeV and 1m LLP for the double
 817 cluster categories. The signal is normalized to $\text{BR}(\text{H} \rightarrow \text{ss}) = 2\%$. Fig. 40 shows the fitted signal
 818 strength and the pull for all 3 samples. The injected signal strength is 1 and no significant bias
 819 has been observed.

Table 29: Signal yield in the signal region in binA, for LLP decaying to 2 τ leptons and various LLP masses, assuming $\text{BR}(\text{H} \rightarrow \text{ss}) = 1\%$.

CSC-CSC				
LLP mass / $c\tau$	100 mm	1000 mm	10000 mm	100000 mm
7 GeV	1.9	0.6	0.0	0.0
15 GeV	0.3	1.7	0.0	0.0
40 GeV	0.0	3.3	0.5	0.0
55 GeV	0.0	0.3	0.2	0.0
DT-DT				
LLP mass / $c\tau$	100 mm	1000 mm	10000 mm	100000 mm
7 GeV	2.4	1.4	0.0	0.0
15 GeV	0.1	3.8	0.1	0.0
40 GeV	0.0	3.2	0.9	0.0
55 GeV	0.0	0.6	0.4	0.0
DT-CSC				
LLP mass / $c\tau$	100 mm	1000 mm	10000 mm	100000 mm
7 GeV	1.7	1.6	0.0	0.0
15 GeV	0.1	3.9	0.2	0.0
40 GeV	0.0	3.3	0.8	0.0
55 GeV	0.0	1.0	0.6	0.0

Table 30: Signal yield in the signal region in binA, for LLP decaying to 2 b quarks and various LLP masses, assuming $\text{BR}(\text{H} \rightarrow \text{ss}) = 1\%$.

CSC-CSC				
LLP mass / $c\tau$	100 mm	1000 mm	10000 mm	100000 mm
15 GeV	0.6	4.3	0.1	0.0
40 GeV	0.0	6.7	1.0	0.0
55 GeV	0.0	0.5	0.3	0.0
DT-DT				
LLP mass / $c\tau$	100 mm	1000 mm	10000 mm	100000 mm
15 GeV	0.3	11.8	0.3	0.0
40 GeV	0.0	10.4	3.2	0.0
55 GeV	0.0	1.5	1.2	0.1
DT-CSC				
LLP mass / $c\tau$	100 mm	1000 mm	10000 mm	100000 mm
15 GeV	0.4	10.0	0.4	0.0
40 GeV	0.0	8.7	2.5	0.0
55 GeV	0.0	2.1	2.0	0.1

9.3 Observed Data

The number of background events predicted from the background-only fit in the signal region is summarized in Table 34, as well as the observed yields. We observe no statistically significant deviation with respect to the expected number of events.

Table 31: Signal yield in the signal region in binA, for 0.4 GeV LLP mass and various decay modes, assuming $\text{BR}(\text{H} \rightarrow \text{ss}) = 1\%$.

CSC-CSC		
LLP decay / $c\tau$	10 mm	50 mm
EE	1.0	0.3
GammaGamma	0.9	0.3
Pi0Pi0	0.9	0.3
PiPlusPiMinus	7.5	1.7

DT-DT		
LLP decay / $c\tau$	10 mm	50 mm
EE	1.6	0.9
GammaGamma	1.9	1.0
Pi0Pi0	1.6	0.8
PiPlusPiMinus	15.1	5.9

DT-CSC		
LLP decay / $c\tau$	10 mm	50 mm
EE	1.4	0.9
GammaGamma	1.3	1.0
Pi0Pi0	1.3	1.0
PiPlusPiMinus	10.1	5.8

Table 32: Signal yield in the signal region in binA, for 1 GeV LLP mass and various decay modes, assuming $\text{BR}(\text{H} \rightarrow \text{ss}) = 1\%$.

CSC-CSC		
LLP decay / $c\tau$	25 mm	125 mm
Pi0Pi0	1.1	0.3
PiPlusPiMinus	6.7	1.9

DT-DT		
LLP decay / $c\tau$	25 mm	125 mm
Pi0Pi0	1.3	1.0
PiPlusPiMinus	13.4	5.9

DT-CSC		
LLP decay / $c\tau$	25 mm	125 mm
Pi0Pi0	1.5	0.9
PiPlusPiMinus	9.7	5.4

824 9.4 Expected and Observed Limits

825 We compute expected and observed limits on the Higgs boson branching fraction to long-lived
 826 scalars, $\text{BR}(\text{H} \rightarrow \text{ss})$. The limits are computed based on the background estimation method de-
 827 scribed in Section 6 and performing the maximum likelihood fit expressed in Eq. 4 and Eq. 6
 828 for the corresponding categories using the asymptotic approximation.

829 The limits on the Higgs decay branching ratio to LLPs are shown in Fig. 41 separately for sce-
 830 narios where each LLP exclusively decays into 2 b quarks, 2 d quarks, 2 τ leptons, 2 electrons, 2
 831 photons, 2 $\pi^0, \pi^+ \pi^-$, 2 K^0 , and $K^+ K^-$. The signal contributions of all the available produc-
 832 tions are included, including ggH, VBF, VH, and ttH. With just the double cluster category, we are
 833 able to achieve branching ratios of about 9×10^{-4} at the most sensitive lifetime when the LLP

Table 33: Signal yield in the signal region in binA, for 1.5 GeV LLP mass and various decay modes, assuming $\text{BR}(\text{H} \rightarrow \text{ss}) = 1\%$.

CSC-CSC		
LLP decay / $c\tau$	38 mm	187 mm
KPlusKMinus	7.1	2.1
K0K0	6.6	2.1
DT-DT		
LLP decay / $c\tau$	38 mm	187 mm
KPlusKMinus	15.1	7.2
K0K0	15.4	6.3
DT-CSC		
LLP decay / $c\tau$	38 mm	187 mm
KPlusKMinus	11.2	6.4
K0K0	12.1	6.0

Table 34: Number of background events in the signal region observed and predicted by the background-only fit using the ABCD method.

category	fit	A(SR)	B	C
CSC-CSC	Background-only fit	0.7 ± 0.4	3.6 ± 1.5	4.7 ± 2.0
	Observation	2	1	6
DT-DT	Background-only fit	0.06 ± 0.06	0.9 ± 0.7	3.1 ± 1.6
	Observation	0	1	3
category	fit	A(SR)	B	C
				D
DT-CSC	Background-only fit	0.12 ± 0.12	1.9 ± 1.2	14.1 ± 3.8
	Observation	0	2	14
				1

⁸³⁴ decays into 2 b, 2 d quarks, $\pi^+ \pi^-$, $K^+ K^-$ or 2 K^0 , branching ratio of 2×10^{-3} when the LLP
⁸³⁵ decays into 2 τ leptons, and branching ratio of 7×10^{-3} when the LLP decays into 2 electrons,
⁸³⁶ 2 photons, or 2 π^0 .

⁸³⁷ Additionally Figure 42 through Figure 46 show the limits on the branching ratio of the Higgs
⁸³⁸ to the dark sector for the Dark Shower benchmarks. A wide range of portals, masses and
⁸³⁹ lifetimes are considered, with the search typically achieving an optimal expected limit of sub-
⁸⁴⁰ percent level branching ratio for all portals except for the dark photon portal. These results
⁸⁴¹ highlight the unique sensitivity of the search to dark shower signatures, including in the case
⁸⁴² that the dark mesons have masses as low as a few GeV and for electromagnetic showers in the
⁸⁴³ muon system.

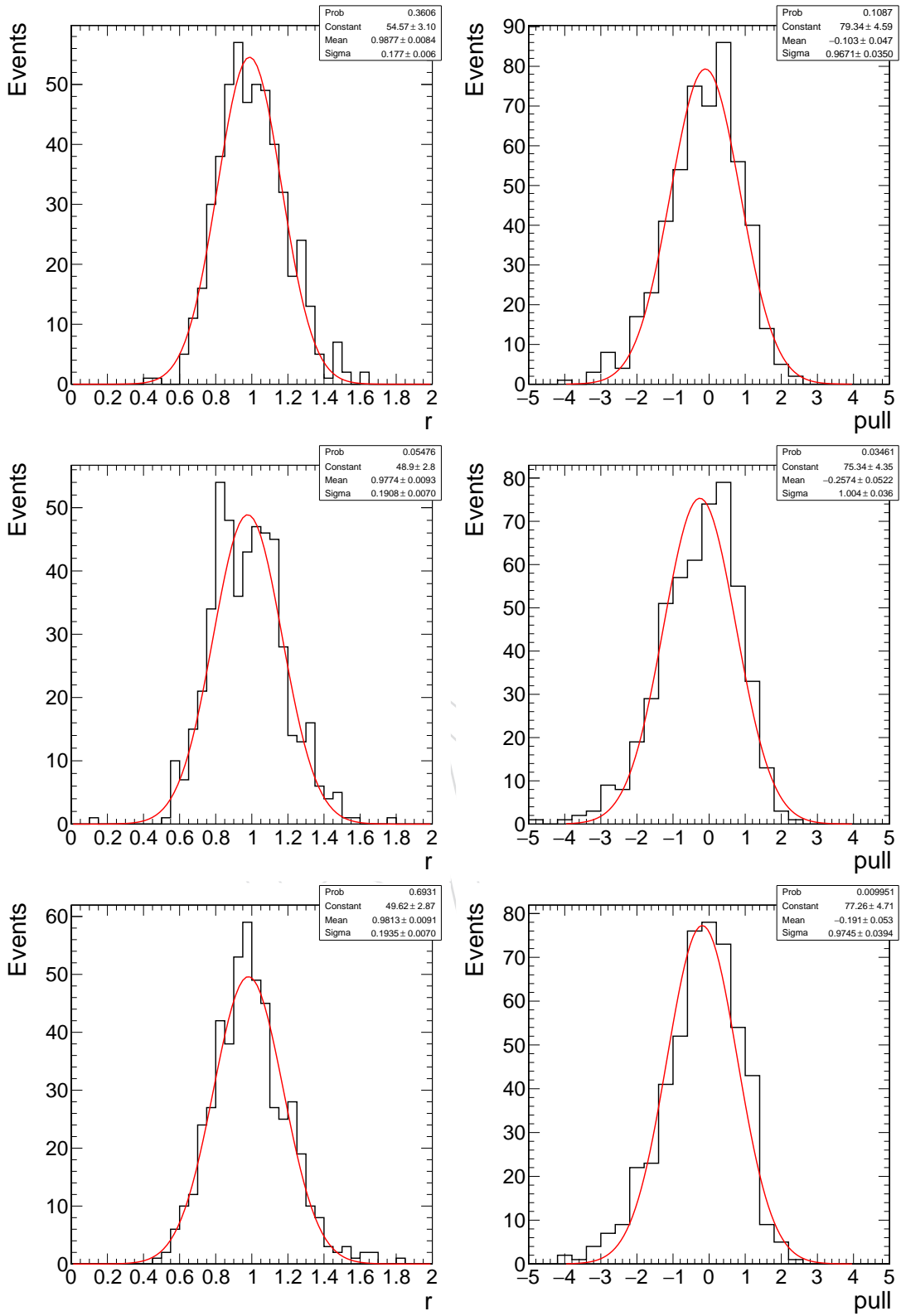


Figure 40: The fitted signal strength (left) and pull (right) distributions of the toy datasets when injected with signal with 15 GeV and 0.5 m lifetime LLP (top), 15 GeV and 1m lifetime LLP (middle), and 40 GeV and 1m LLP (bottom).

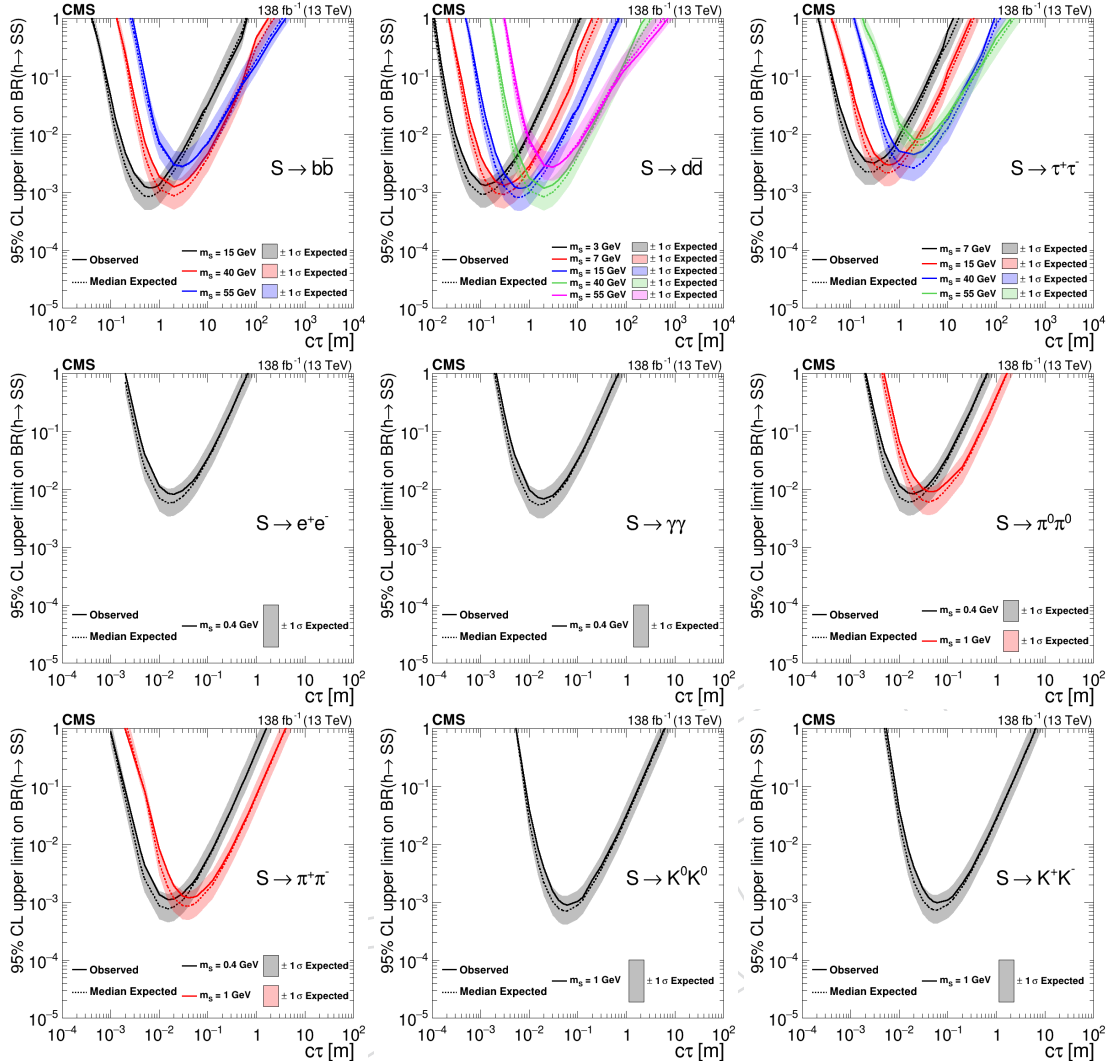


Figure 41: The limits for signal predictions that include ggH, VBF, VH, and ttH production modes for 2b (Top Left), 2d (Top Center), 2 τ (Top Right), 2 electrons (Middle Left), 2 photons (Middle Center), 2 π^0 (Middle Right), $\pi^+\pi^-$ (Bottom Left), 2 K^0 (Bottom Center), and K^+K^- (Bottom Right) decay modes are shown.

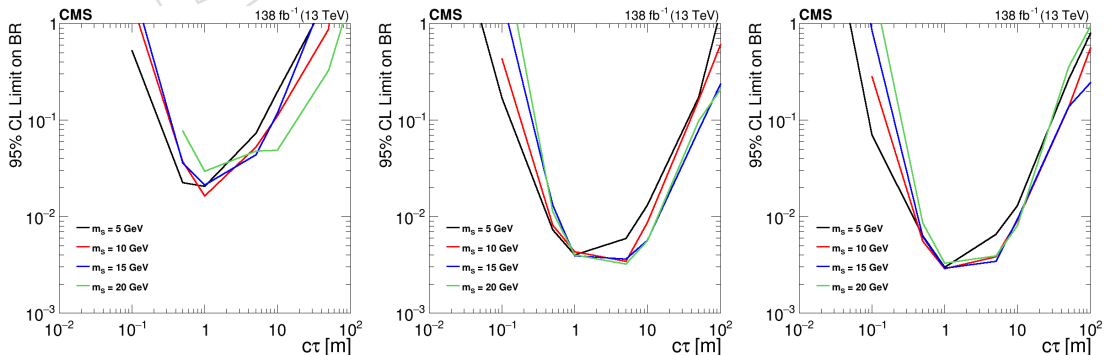


Figure 42: The observed limits for Higgs Dark Shower model with gluon portal and mass ratios $x_{i\omega} = x_{i\Lambda} = 1.0$ (left), $x_{i\omega} = 2.5, x_{i\Lambda} = 1.0$ (middle), and $x_{i\omega} = x_{i\Lambda} = 2.5$ (right).

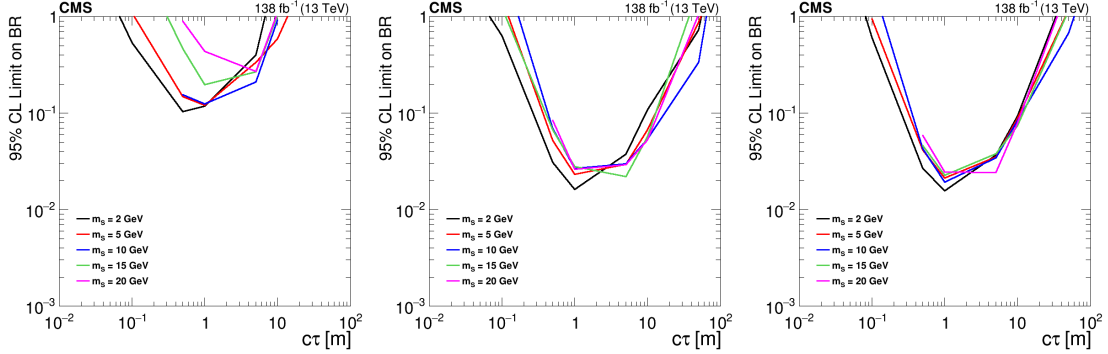


Figure 43: The observed limits for Higgs Dark Shower model with photon portal and mass ratios $x_{i\omega} = x_{i\Lambda} = 1.0$ (left), $x_{i\omega} = 2.5, x_{i\Lambda} = 1.0$ (middle), and $x_{i\omega} = x_{i\Lambda} = 2.5$ (right).

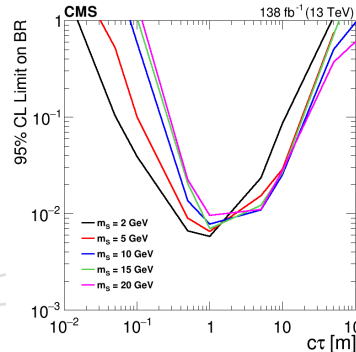


Figure 44: The observed limits for Higgs Dark Shower model with vector portal and mass ratio $x_{i\omega} = x_{i\Lambda} = 1.0$.

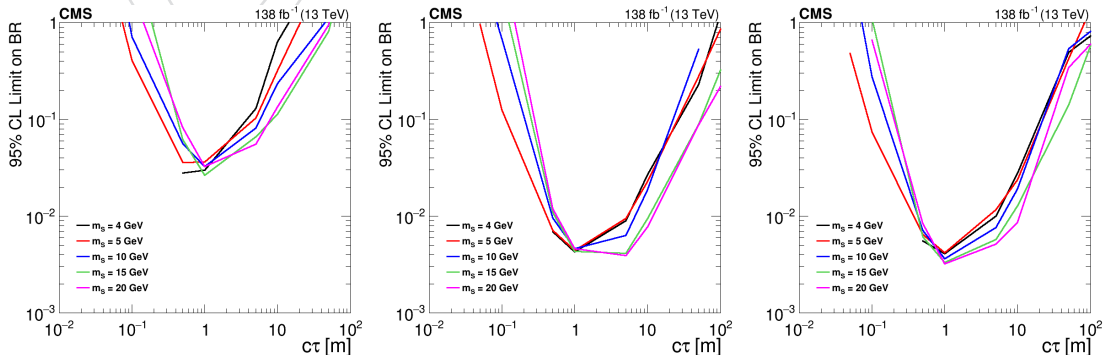


Figure 45: The observed limits for Higgs Dark Shower model with higgs portal and mass ratios $x_{i\omega} = x_{i\Lambda} = 1.0$ (left), $x_{i\omega} = 2.5, x_{i\Lambda} = 1.0$ (middle), and $x_{i\omega} = x_{i\Lambda} = 2.5$ (right).

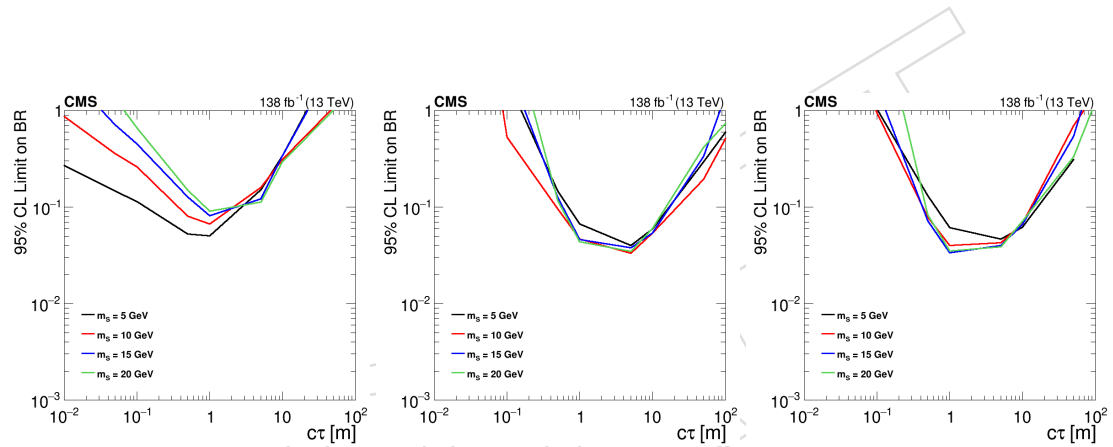


Figure 46: The observed limits for Higgs Dark Shower model with dark photon portal and mass ratios $x_{i\omega} = x_{i\Lambda} = 1.0$ (left), $x_{i\omega} = 2.5, x_{i\Lambda} = 1.0$ (middle), and $x_{i\omega} = x_{i\Lambda} = 2.5$ (right).

844 10 Combination

845 In this section, we present the combination of single CSC cluster category (detailed in AN-
 846 19-154), single DT cluster category (detailed in AN-21-056), and the double-cluster category,
 847 detailed in the previous sections in AN.

848 With the requirement of an additional cluster in the Muon System, the two-cluster category
 849 has a lower background level, while maintaining a decent level of signal efficiency, especially
 850 when the LLPs are expected to decay within the Muon System. As described in section 5, the
 851 $N_{rechits}$ thresholds in the two-cluster category are adjusted to achieve a better sensitivity since
 852 the background level is lowered.

853 The ABCD planes of the 3 categories are defined to be mutually exclusive to each others, for an
 854 easier statistical treatment. Due to the better sensitivity of the two-cluster category, an event is
 855 assigned to the two-cluster category if it passes both of the selections of the one-cluster and the
 856 two-cluster category. The fraction of overlap signal events are studied in details in appendix D.
 857 Since there are no observed two-cluster events in the unblinded CSC one-cluster region, the
 858 data-driven background method of EXO-20-015 is un-affected by the choice of assigning over-
 859 laped events to the two-cluster category. The impact of the migrated signal events on exclusion
 860 limits is shown in Fig. 65.

861 Since the 3 categories are statistically independent, they are combined at the datacard level
 862 using the HiggsCombine Tool. All theoretical uncertainties assigned to signal simulations are
 863 fully correlated. As a conservative estimation, experimental uncertainties associated with clus-
 864 ter selections are assumed to be fully uncorrelated.

865 10.1 Observed Limits

866 First, we present observed limits on the Higgs boson branching fraction to long-lived scalars,
 867 $\text{BR}(\text{H} \rightarrow \text{ss})$, for LLP mass between 7 and 55 GeV. The limits on the Higgs decay branching ratio
 868 to LLPs are shown in Fig. 47, separately for scenarios where each LLP exclusively decays into
 869 2 b quarks, 2 d quarks, and 2 τ leptons. We show the contribution from each category and the
 870 combination of the pre-fit expected limits for decays to $d\bar{d}$ and $\tau\tau$ are shown in Fig. 48.

871 The single CSC category is most sensitive at lower lifetime. The single DT category is most
 872 sensitive at larger lifetime, while the double cluster category is most sensitive in the middle.
 873 The signal contributions of all the available productions are included, including ggH, VBF, VH,
 874 and ttH. We achieve branching ratios limits of about 5×10^{-4} at the most sensitive lifetime
 875 when the LLP decays into 2 b or 2 d quarks and branching ratio of 1×10^{-3} when the LLP
 876 decays into 2 τ leptons.

877 We also show the comparison of the pre-fit expected limit of the combined limit with respect to
 878 the expected single CSC category limit, in Fig. 49. The improvement with respect to EXO-20-
 879 015 mostly comes from proper lifetimes with the peak sensitivity, dominated by double cluster
 880 category and long proper lifetimes, where single DT cluster category contributes more strongly.
 881 There is almost no change at low proper lifetimes, since the sensitivity at low proper lifetimes
 882 is dominated by single CSC cluster category.

883 Additionally, Figure 50 through Figure 54 show the combined expected limits on the branching
 884 ratio of the Higgs to the dark sector for the Dark Shower benchmarks. A wide range of portals,
 885 masses and lifetimes are considered, with the search typically achieving an optimal expected
 886 limit of sub-percent level branching ratio for all portals except for the dark photon portal. These
 887 results highlight the unique sensitivity of the search to dark shower signatures, including in the

case that the dark mesons have masses as low as a few GeV and for electromagnetic showers in the muon system.

Furthermore, we also show the breakdown of the 3 categories and the combined limits for the higgs portal, assuming 15 GeV LLP mass, for all 3 mass ratios scenarios, in Figure 55. The contribution of the double cluster category relative to the two single cluster contributions depends on the acceptance. When the LLP multiplicity is higher the probability of having two LLPs decaying in the muon system is significantly higher. Therefore, the double tag contribution is more dominant when $x_{i\omega} = 2.5$.

We also show the breakdown of the 3 categories, in Figure 56, comparing different portals (higgs, gluon, and photon portals), assuming 15 GeV LLP mass and $x_{i\omega} = 2.5, x_{i\Lambda} = 1.0$. The contribution of the double cluster category relative to the two single cluster contributions depends significantly on the cluster efficiency, because the signal yield is proportional to efficiency squared rather than one factor of efficiency. For gluon and the higgs portal, where LLP decay hadronically, the double cluster category dominates the sensitivity at $c\tau \approx 1\text{m}$. But for the photon portal, where LLPs decay leptonically, the double cluster category does not perform better than the single cluster categories.

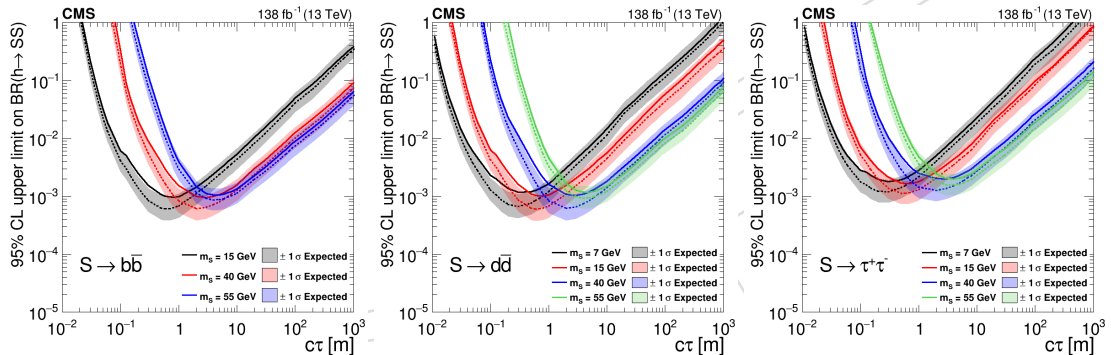


Figure 47: The limits for the combination of the single cluster and two cluster categories. The signal predictions include the ggH, VBF, VH, and ttH production modes for 2b (Left), 2d (Middle), 2 τ (Right) decay modes are shown.

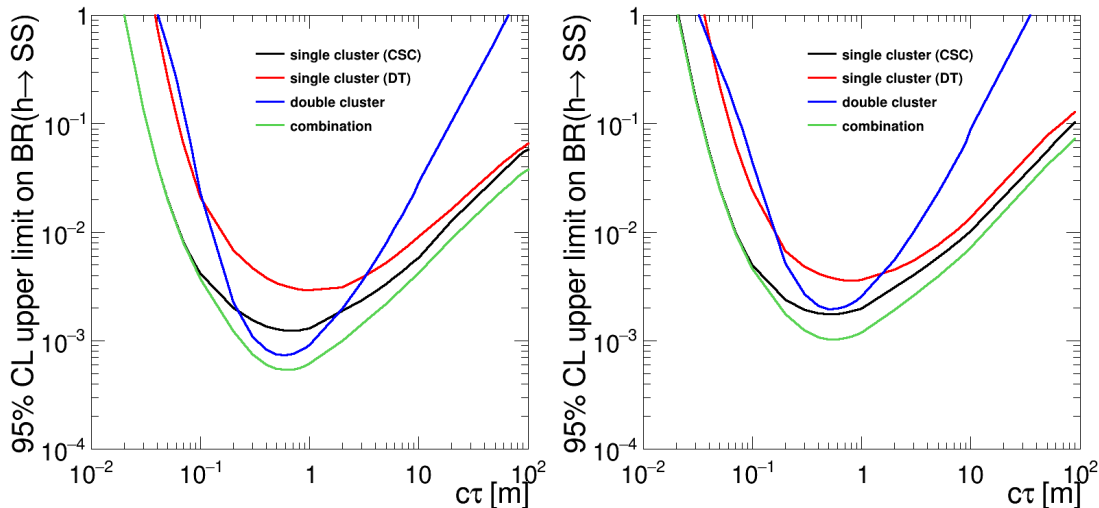


Figure 48: The combined pre-fit expected limits of the 3 categories and the breakdown are shown for 15 GeV LLP decaying to $d\bar{d}$ (left) and $\tau\tau$ (right).

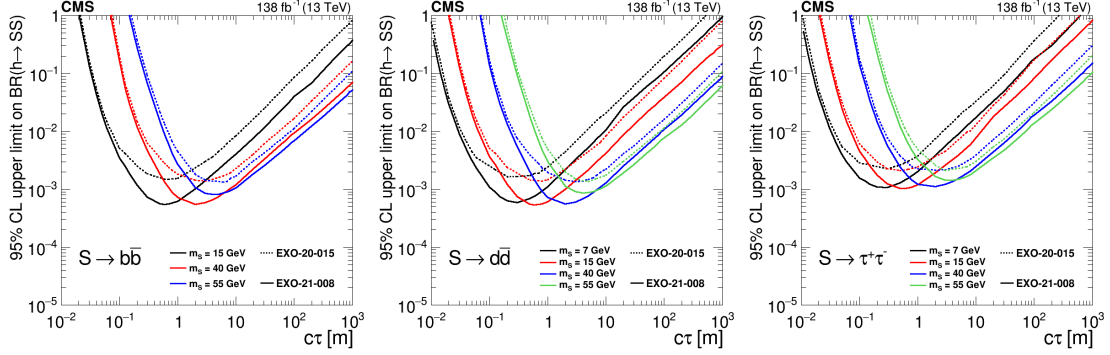


Figure 49: The combined pre-fit expected limits of the 3 categories and the comparison with pre-fit expected limits from EXO-20-015 are shown for LLP decaying to $b\bar{b}$ (left), $d\bar{d}$ (center) and $\tau^+\tau^-$ (right).

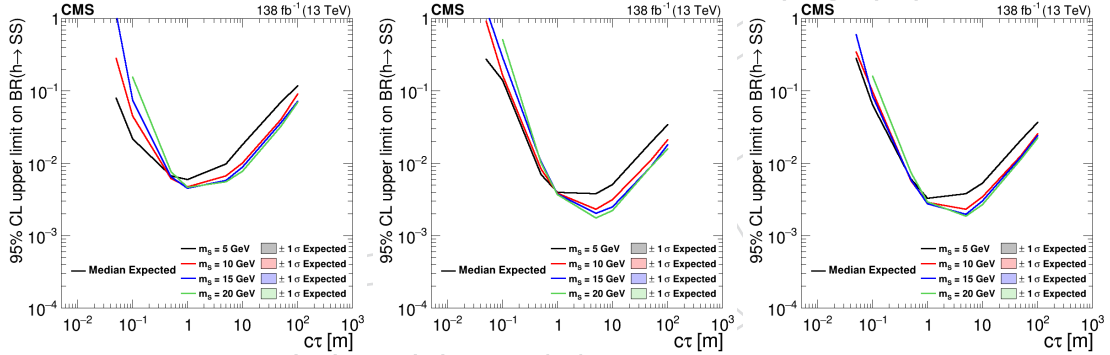


Figure 50: The combined observed limit for Higgs Dark Shower model with gluon portal and mass ratios $x_{i\omega} = x_{i\Lambda} = 1.0$ (left), $x_{i\omega} = 2.5, x_{i\Lambda} = 1.0$ (middle), and $x_{i\omega} = x_{i\Lambda} = 2.5$ (right).

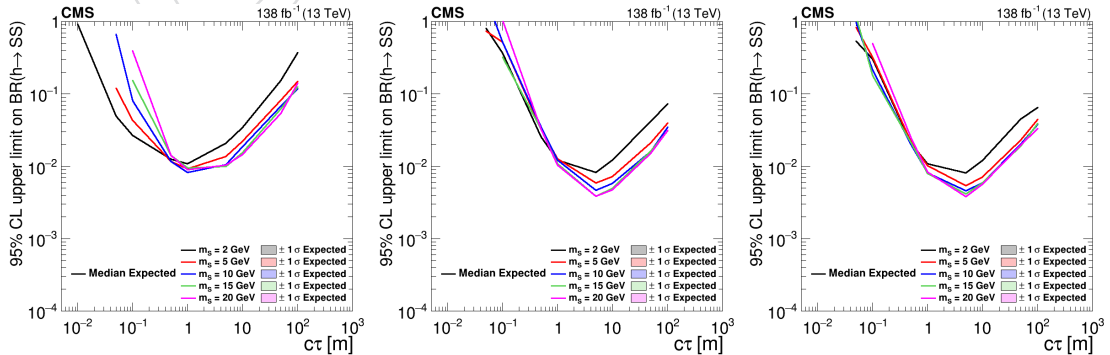


Figure 51: The combined observed limit for Higgs Dark Shower model with photon portal and mass ratios $x_{i\omega} = x_{i\Lambda} = 1.0$ (left), $x_{i\omega} = 2.5, x_{i\Lambda} = 1.0$ (middle), and $x_{i\omega} = x_{i\Lambda} = 2.5$ (right).

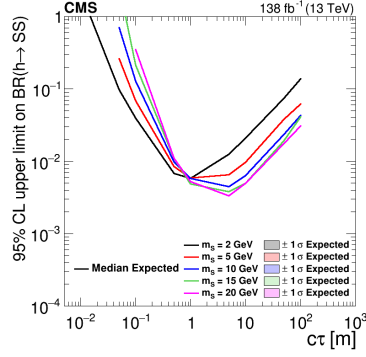


Figure 52: The combined observed limit for Higgs Dark Shower model with vector portal and mass ratio $x_{i\omega} = x_{i\Lambda} = 1.0$.

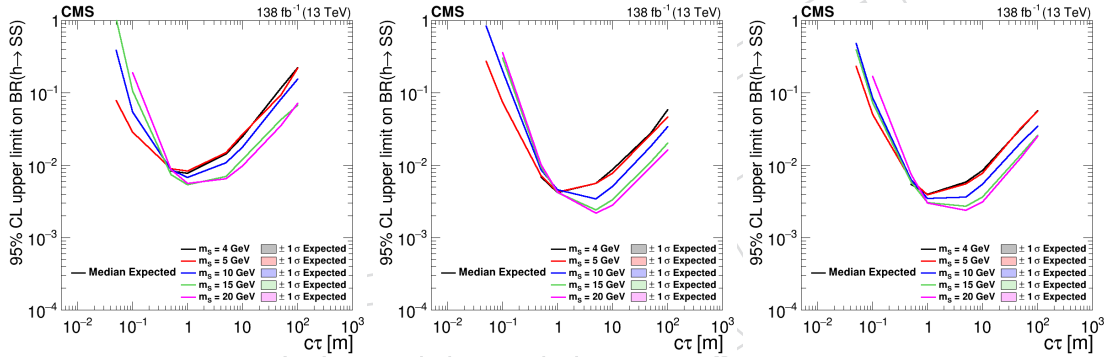


Figure 53: The combined observed limit for Higgs Dark Shower model with higgs portal and mass ratios $x_{i\omega} = x_{i\Lambda} = 1.0$ (left), $x_{i\omega} = 2.5, x_{i\Lambda} = 1.0$ (middle), and $x_{i\omega} = x_{i\Lambda} = 2.5$ (right).

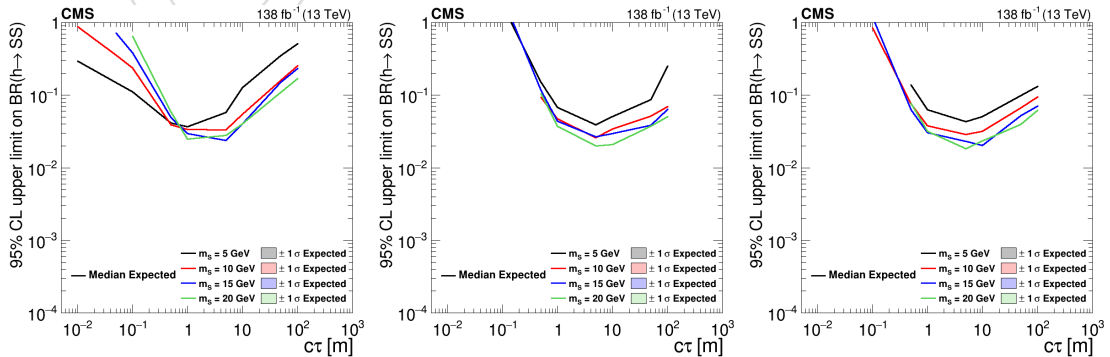


Figure 54: The combined observed limit for Higgs Dark Shower model with dark photon portal and mass ratios $x_{i\omega} = x_{i\Lambda} = 1.0$ (left), $x_{i\omega} = 2.5, x_{i\Lambda} = 1.0$ (middle), and $x_{i\omega} = x_{i\Lambda} = 2.5$ (right).

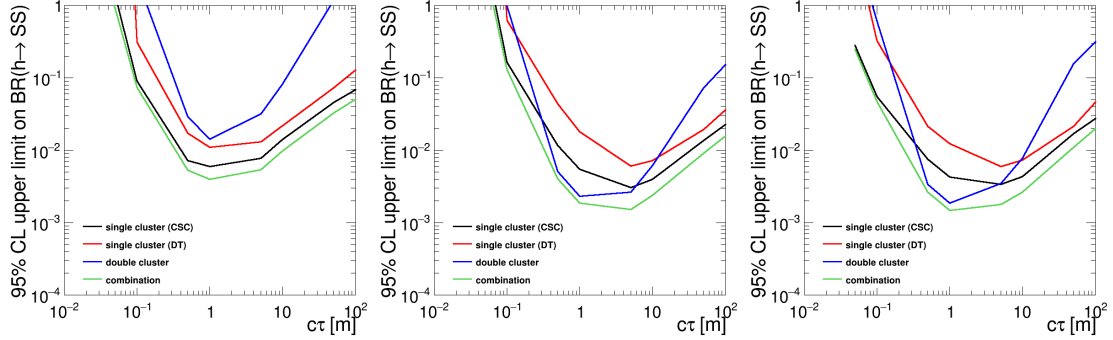


Figure 55: The combined pre-fit expected limits of the 3 categories and the breakdown are shown for Higgs Dark Shower model with higgs portal, assuming LLP mass of 15 GeV and mass ratios $x_{i\omega} = x_{i\Lambda} = 1.0$ (left), $x_{i\omega} = 2.5, x_{i\Lambda} = 1.0$ (middle), and $x_{i\omega} = x_{i\Lambda} = 2.5$ (right). The contribution of the double cluster category relative to the two single cluster contributions depends on the LLP multiplicity, so when $x_{i\omega} = 2.5$, the LLP multiplicity is higher, the double cluster category dominates at $c\tau$ of around 1 m.

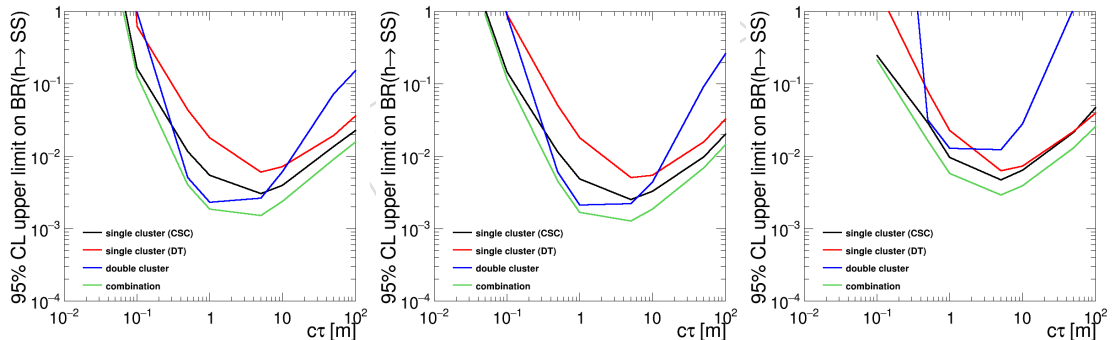


Figure 56: The combined pre-fit expected limits of the 3 categories and the breakdown are shown for Higgs Dark Shower model with higgs portal (left), gluon portal (middle), and photon portal (right). The LLP mass is 15 GeV and mass ratios are $x_{i\omega} = 2.5, x_{i\Lambda} = 1.0$. The contribution of the double cluster category relative to the two single cluster contributions depends significantly on the cluster efficiency, because the signal yield is proportional to efficiency squared rather than one factor of efficiency. For gluon and the higgs portal, where LLP decay hadronically, the double cluster category dominates the sensitivity at $c\tau \approx 1$ m. But for the photon portal, where LLPs decay leptonically, the double cluster category does not perform better than the single cluster categories.

904 11 Summary

905 A search for long-lived particles that decay in the muon system (both DT and CSC) and create
906 showers is performed with full Run2 data, on the pp-collision collected at $\sqrt{s} = 13$ TeV, with
907 an integrated luminosity of 137 fb^{-1} . Clusters of Muon System RecHits with large multiplicity
908 are used to identify signal events. We use the ABCD method to predict the background in
909 the signal-enriched region. We set highly competitive limits on Higgs-mediated production of
910 LLPs decaying to a number of different final states at the 10^{-4} level of Higgs to LLP branching
911 ratio. This analysis represents the most sensitive search for Higgs-mediated LLP production at
912 the LHC for proper lifetime ($c\tau$) above a few meters. We also set first limits on the Higgs to
913 dark quarks for the Dark Shower benchmarks. A wide range of portals, masses and lifetimes
914 are interpreted, with the search typically achieving an optimal expected limit of sub-percent
915 level branching ratio for all portals except for the dark photon portal. These results highlight
916 the unique sensitivity of the search to dark shower signatures, including in the case that the
917 dark mesons have masses as low as a few GeV and for electromagnetic showers in the muon
918 system.



919 **Acknowledgments**

920 **References**

- 921 [1] Z. Liu and B. Tweedie, "The fate of long-lived superparticles with hadronic decays after
922 LHC Run 1", *JHEP* **06** (2015) 042, doi:10.1007/JHEP06(2015)042,
923 arXiv:1503.05923.
- 924 [2] G. F. Giudice and A. Romanino, "Split supersymmetry", *Nucl. Phys. B* **699** (2004) 65,
925 doi:10.1016/j.nuclphysb.2004.08.001, arXiv:hep-ph/0406088. [Erratum:
926 doi:10.1016/j.nuclphysb.2004.11.048].
- 927 [3] J. L. Hewett, B. Lillie, M. Masip, and T. G. Rizzo, "Signatures of long-lived gluinos in split
928 supersymmetry", *JHEP* **09** (2004) 070, doi:10.1088/1126-6708/2004/09/070,
929 arXiv:hep-ph/0408248.
- 930 [4] N. Arkani-Hamed, S. Dimopoulos, G. F. Giudice, and A. Romanino, "Aspects of split
931 supersymmetry", *Nucl. Phys. B* **709** (2005) 3,
932 doi:10.1016/j.nuclphysb.2004.12.026, arXiv:hep-ph/0409232.
- 933 [5] P. Gambino, G. F. Giudice, and P. Slavich, "Gluino decays in split supersymmetry", *Nucl.*
934 *Phys. B* **726** (2005) 35, doi:10.1016/j.nuclphysb.2005.08.011,
935 arXiv:hep-ph/0506214.
- 936 [6] A. Arvanitaki, N. Craig, S. Dimopoulos, and G. Villadoro, "Mini-split", *JHEP* **02** (2013)
937 126, doi:10.1007/JHEP02(2013)126, arXiv:1210.0555.
- 938 [7] N. Arkani-Hamed et al., "Simply unnatural supersymmetry", (2012).
939 arXiv:1212.6971.
- 940 [8] P. Fayet, "Supergauge invariant extension of the Higgs mechanism and a model for the
941 electron and its neutrino", *Nucl. Phys. B* **90** (1975) 104,
942 doi:10.1016/0550-3213(75)90636-7.
- 943 [9] G. R. Farrar and P. Fayet, "Phenomenology of the production, decay, and detection of
944 new hadronic states associated with supersymmetry", *Phys. Lett. B* **76** (1978) 575,
945 doi:10.1016/0370-2693(78)90858-4.
- 946 [10] S. Weinberg, "Supersymmetry at ordinary energies. 1. masses and conservation laws",
947 *Phys. Rev. D* **26** (1982) 287, doi:10.1103/PhysRevD.26.287.
- 948 [11] R. Barbier et al., " R -parity violating supersymmetry", *Phys. Rept.* **420** (2005) 1,
949 doi:10.1016/j.physrep.2005.08.006, arXiv:hep-ph/0406039.
- 950 [12] G. F. Giudice and R. Rattazzi, "Theories with gauge mediated supersymmetry breaking",
951 *Phys. Rept.* **322** (1999) 419, doi:10.1016/S0370-1573(99)00042-3,
952 arXiv:hep-ph/9801271.
- 953 [13] P. Meade, N. Seiberg, and D. Shih, "General gauge mediation", *Prog. Theor. Phys. Suppl.*
954 **177** (2009) 143, doi:10.1143/PTPS.177.143, arXiv:0801.3278.
- 955 [14] M. Buican, P. Meade, N. Seiberg, and D. Shih, "Exploring general gauge mediation",
956 *JHEP* **03** (2009) 016, doi:10.1088/1126-6708/2009/03/016, arXiv:0812.3668.

- [15] J. Fan, M. Reece, and J. T. Ruderman, “Stealth supersymmetry”, *JHEP* **11** (2011) 012, doi:10.1007/JHEP11(2011)012, arXiv:1105.5135.
- [16] J. Fan, M. Reece, and J. T. Ruderman, “A stealth supersymmetry sampler”, *JHEP* **07** (2012) 196, doi:10.1007/JHEP07(2012)196, arXiv:1201.4875.
- [17] M. J. Strassler and K. M. Zurek, “Echoes of a hidden valley at hadron colliders”, *Phys. Lett. B* **651** (2007) 374, doi:10.1016/j.physletb.2007.06.055, arXiv:hep-ph/0604261.
- [18] M. J. Strassler and K. M. Zurek, “Discovering the Higgs through highly-displaced vertices”, *Phys. Lett. B* **661** (2008) 263, doi:10.1016/j.physletb.2008.02.008, arXiv:hep-ph/0605193.
- [19] T. Han, Z. Si, K. M. Zurek, and M. J. Strassler, “Phenomenology of hidden valleys at hadron colliders”, *JHEP* **07** (2008) 008, doi:10.1088/1126-6708/2008/07/008, arXiv:0712.2041.
- [20] Y. Cui, L. Randall, and B. Shuve, “A WIMPY baryogenesis miracle”, *JHEP* **04** (2012) 075, doi:10.1007/JHEP04(2012)075, arXiv:1112.2704.
- [21] Y. Cui and R. Sundrum, “Baryogenesis for weakly interacting massive particles”, *Phys. Rev. D* **87** (2013) 116013, doi:10.1103/PhysRevD.87.116013, arXiv:1212.2973.
- [22] Y. Cui and B. Shuve, “Probing baryogenesis with displaced vertices at the LHC”, *JHEP* **02** (2015) 049, doi:10.1007/JHEP02(2015)049, arXiv:1409.6729.
- [23] Z. Chacko, H.-S. Goh, and R. Harnik, “Natural electroweak breaking from a mirror symmetry”, *Phys. Rev. Lett.* **96** (2006) 231802, doi:10.1103/PhysRevLett.96.231802, arXiv:hep-ph/0506256.
- [24] D. Curtin and C. B. Verhaaren, “Discovering uncolored naturalness in exotic Higgs decays”, *JHEP* **12** (2015) 072, doi:10.1007/JHEP12(2015)072, arXiv:1506.06141.
- [25] H.-C. Cheng, S. Jung, E. Salvioni, and Y. Tsai, “Exotic quarks in twin Higgs models”, *JHEP* **03** (2016) 074, doi:10.1007/JHEP03(2016)074, arXiv:1512.02647.
- [26] Artur Apresyan, Matthew Citron, Daniel Diaz, Gabrielle Dituri, Javier Duarte, Zoltan Gecse, Gregor Kasieczka, Cristian Pena, Joerg Schindler, James Sheplock, Nathan Suri, Maria Spiropulu, Christina Wang, Si Xie, “Search for Neutral Long-lived Particles Decaying in the Muon System”, *CMS Physics Analysis Note AN-2019/154* (2019).
- [27] James Sheplock, David Stuart, Matthew Citron, Daniel Diaz, Javier Duarte, Farouk Mokhtar, Cristian Pena, Joerg Schindler, Christina Wang, Si Xie, “Search for neutral long-lived particles decaying in the CMS Muon Barrel”, *CMS Physics Analysis Note AN-2021/056* (2021).
- [28] F. Bezrukov and D. Gorbunov, “Light inflaton after LHC8 and WMAP9 results”, *JHEP* **07** (2013) 140, doi:10.1007/JHEP07(2013)140, arXiv:1303.4395.
- [29] “Baseline muon selections for Run-II”.
<https://twiki.cern.ch/twiki/bin/viewauth/CMS/SWGuideMuonIdRun2>.

- 996 [30] "SM Higgs production cross sections at $\sqrt{s} = 13$ TeV". <https://twiki.cern.ch/twiki/bin/view/LHCPhysics/CERNYellowReportPageAt13TeV>.
- 997
- 998 [31] S. Knapen, J. Shelton, and D. Xu, "Perturbative benchmark models for a dark shower
999 search program", 2021. <https://arxiv.org/abs/2103.01238>.
- 1000 [32] J. Alimena et al., "Searching for long-lived particles beyond the standard model at the
1001 large hadron collider", *Journal of Physics G: Nuclear and Particle Physics* **47** (2020) 090501,
1002 doi:10.1088/1361-6471/ab4574.
- 1003 [33] K. Hamilton, P. Nason, E. Re, and G. Zanderighi, "NNLOPS simulation of Higgs boson
1004 production", *JHEP* **10** (2013) 222, doi:10.1007/JHEP10(2013)222,
1005 arXiv:1309.0017.
- 1006 [34] M. Ester, H.-P. Kriegel, J. Sander, and X. Xu, "A density-based algorithm for discovering
1007 clusters in large spatial databases with noise", *Data Mining and Knowledge Discovery*
1008 (1996) 226–231.
- 1009 [35] "Recommended Jet Energy Corrections and Uncertainties for Data and MC".
1010 <https://twiki.cern.ch/twiki/bin/view/CMS/JECDataMC>.
- 1011 [36] "Jet Identification". <https://twiki.cern.ch/twiki/bin/view/CMS/JetID>.
- 1012 [37] CMS Collaboration, "Performance of the CMS muon detector and muon reconstruction
1013 with proton-proton collisions at $\sqrt{s} = 13$ TeV", *JINST* **13** (2018), no. 06, P06015,
1014 doi:10.1088/1748-0221/13/06/P06015, arXiv:1804.04528.
- 1015 [38] "MET Corrections and Uncertainties for Run-II". <https://twiki.cern.ch/twiki/bin/viewauth/CMS/MissingETRun2Corrections>.
- 1016
- 1017 [39] "Official Prescription for calculating corrections and uncertainties on Missing Transverse
1018 Energy (MET)". <https://twiki.cern.ch/twiki/bin/view/CMS/MissingETUncertaintyPrescription>.
- 1019
- 1020 [40] "MET Filter Recommendations for Run II". <https://twiki.cern.ch/twiki/bin/viewauth/CMS/MissingETOptionalFiltersRun2>.
- 1021
- 1022 [41] "CSC Segment Time Reconstruction". <https://github.com/cms-sw/cmssw/blob/master/RecoMuon/MuonIdentification/src/CSCTimingExtractor.cc>.
- 1023
- 1024 [42] "Luminosity Physics Object Group – Lumi POG".
1025 <https://twiki.cern.ch/twiki/bin/view/CMS/TWikiLUM>.
- 1026
- 1027 [43] "Analysis checklist for the pre-approval in the EXO PAG".
<https://twiki.cern.ch/twiki/bin/view/CMS/ExoPreapprovalChecklist>.

1028 A Signal Cut Flow Table

1029 We summarize the signal cut flow table of the signal samples with different mass, lifetime, and
 1030 decay modes in this section.

1031 The signal efficiency for twin higgs model are shown in Table 38 through Table 47. The signal
 1032 efficiency of all the selections applied is shown for the gluon-fusion production mode and 4b
 1033 decay mode, for LLP lifetime of 1 meter and mass 15, 40, and 55 GeV in Table 35, 36, and 37,
 1034 respectively. The signal efficiency of all the selections applied is shown for the gluon-fusion
 1035 production mode and 4τ decay mode, for LLP lifetime of 1 meter and mass 7, 15, 40, and 55
 1036 GeV in Table 38, Table 39, 40, and 41, respectively. The signal efficiency of 0.4 GeV LLP with
 1037 lifetime of 10mm decaying to 2 electrons and decaying to 2 photons are shown in Table 42 and
 1038 Table 43, respectively. 1.5 GeV LLP with lifetime of 187mm decaying to 2 charged kaons and
 1039 decaying to 2 neutral kaons are shown in Table 44 and Table 45, respectively 1 GeV LLP with
 1040 lifetime of 125 mm decaying to 2 charged pions and decaying to 2 neutral pions are shown in
 1041 Table 46 and Table 47, respectively

1042 The signal efficiency for hidden valley model are shown in Table 48 through Table 60 for 15 GeV
 1043 LLP and 5 m lifetime, and for various portals, $x_{i\omega}$, and $x_{i\Lambda}$. Table 48, Table 49, and Table 50,
 1044 show the signal efficiency for the higgs portal and various dark meson mass ratio. Table 51,
 1045 Table 52, and Table 53, show the signal efficiency for the gluon portal and various dark meson
 1046 mass ratio. Table 54 shows the signal efficiency for the vector portal. Table 55, Table 56, and
 1047 Table 57, show the signal efficiency for the photon portal and various dark meson mass ratio.
 1048 Table 58, Table 59, and Table 60, show the signal efficiency for the dark photon portal and
 1049 various dark meson mass ratio.



Table 35: Signal Efficiency(%) of each cut for twin higgs model, LLP mass 15 GeV, lifetime of 1000 mm and decaying to 2 b quarks. (Cumulative Efficiency for all cuts applied after Trigger and MET cut are calculated with respect to events in acceptance and pass the MET and trigger cut and cut efficiency is calculated with respect to the previous cut. Acceptance is defined as when at least one LLP decays inside CSC.)

Selection	CSC-CSC		DT-DT		DT-CSC	
	cut eff	overall eff	cut eff	overall eff	cut eff	overall eff
acceptance	2.119	2.119	6.435	6.435	6.501	6.501
Trigger and MET	0.794	0.017	0.883	0.057	0.668	0.043
MET filters	97.66	97.66	95.46	95.46	97.20	97.20
$N_{jet} \geq 1$	96.45	94.20	97.07	92.66	96.34	93.64
$N_{\text{CSC+DT rings}} \leq 10$	100.00	94.20	100.00	92.66	100.00	93.64
DT noise veto	100.00	94.20	99.93	92.60	100.00	93.64
$N_{\text{cluster}} \geq 2$	40.33	37.99	48.68	45.08	36.97	34.62
DT cosmic veto	/	/	99.54	44.87	99.93	34.59
muon veto	99.84	37.93	97.84	43.91	98.81	34.18
jet veto	90.62	34.37	94.39	41.44	94.05	32.15
ME11/MB1 ratio	97.36	33.47	90.88	37.66	93.00	29.90
$N_{\text{minstationhits}} / N_{\text{maxstationhits}}$	/	/	99.62	37.52	99.83	29.85
time cut	97.06	32.48	/	/	100.00	29.85
time spread	95.41	30.99	/	/	98.71	29.46
$\Delta\phi(\text{cluster}, \text{MET})$	88.85	28	90.02	33.78	93.70	27.61
$\Delta R(\text{cluster1}, \text{cluster2})$	100.00	27.54	/	/	100.00	27.61
N_{rechits} cut	84.07	23.15	67.46	22.79	80.65	22.26

Table 36: Signal Efficiency(%) of each cut for twin higgs model, LLP mass 40 GeV, lifetime of 1000 mm and decaying to 2 b quarks. (Cumulative Efficiency for all cuts applied after Trigger and MET cut are calculated with respect to events in acceptance and pass the MET and trigger cut and cut efficiency is calculated with respect to the previous cut. Acceptance is defined as when at least one LLP decays inside CSC.)

Selection	CSC-CSC		DT-DT		DT-CSC	
	cut eff	overall eff	cut eff	overall eff	cut eff	overall eff
acceptance	1.037	1.037	1.200	1.200	1.252	1.252
Trigger and MET	2.795	0.029	5.118	0.061	3.180	0.040
MET filters	96.09	96.09	91.81	91.81	94.56	94.56
$N_{jet} \geq 1$	96.64	92.87	97.65	89.66	97.01	91.73
$N_{\text{CSC+DT rings}} \leq 10$	100.00	92.87	100.00	89.66	100.00	91.73
DT noise veto	99.93	92.81	99.89	89.56	99.84	91.58
$N_{\text{cluster}} \geq 2$	37.01	34.35	35.00	31.34	33.44	30.63
DT cosmic veto	/	/	99.87	31.30	99.73	30.54
muon veto	99.94	34.33	98.56	30.85	99.27	30.32
jet veto	88.87	30.51	92.11	28.42	90.95	27.58
ME11/MB1 ratio	94.47	28.82	89.41	25.41	89.49	24.68
$N_{\text{minstationhits}} / N_{\text{maxstationhits}}$	/	/	99.24	25.22	99.95	24.67
time cut	97.14	28.00	/	/	100.00	24.67
time spread	96.13	26.91	/	/	98.41	24.27
$\Delta\phi(\text{cluster}, \text{MET})$	99.22	27	99.58	25.11	100.00	24.27
$\Delta R(\text{cluster1}, \text{cluster2})$	100.00	26.70	/	/	100.00	24.27
$N_{\text{rechits}} \text{ cut}$	83.20	22.22	76.67	19.25	86.54	21.01

Table 37: Signal Efficiency(%) of each cut for twin higgs model, LLP mass 55 GeV, lifetime of 1000 mm and decaying to 2 b quarks. (Cumulative Efficiency for all cuts applied after Trigger and MET cut are calculated with respect to events in acceptance and pass the MET and trigger cut and cut efficiency is calculated with respect to the previous cut. Acceptance is defined as when at least one LLP decays inside CSC.)

Selection	CSC-CSC		DT-DT		DT-CSC	
	cut eff	overall eff	cut eff	overall eff	cut eff	overall eff
acceptance	0.357	0.357	0.290	0.290	0.235	0.235
Trigger and MET	8.519	0.030	17.350	0.050	12.553	0.029
MET filters	95.69	95.69	89.98	89.98	91.99	91.99
$N_{jet} \geq 1$	97.09	92.91	98.19	88.35	98.03	90.17
$N_{\text{CSC+DT rings}} \leq 10$	100.00	92.91	100.00	88.35	100.00	90.17
DT noise veto	99.95	92.86	99.86	88.23	99.83	90.02
$N_{\text{cluster}} \geq 2$	6.81	6.32	6.42	5.67	13.68	12.32
DT cosmic veto	/	/	100.00	5.67	100.00	12.32
muon veto	100.00	6.32	98.81	5.60	98.60	12.15
jet veto	71.11	4.50	89.65	5.02	89.92	10.92
ME11/MB1 ratio	94.16	4.23	85.61	4.30	68.91	7.53
$N_{\text{minstationhits}} / N_{\text{maxstationhits}}$	/	/	100.00	4.30	100.00	7.53
time cut	58.04	2.46	/	/	100.00	7.53
time spread	88.42	2.17	/	/	98.64	7.42
$\Delta\phi(\text{cluster}, \text{MET})$	92.86	2	100.00	4.30	100.00	7.42
$\Delta R(\text{cluster1}, \text{cluster2})$	100.00	2.02	/	/	100.00	7.42
N_{rechits} cut	66.22	1.34	79.43	3.41	87.38	6.49

Table 38: Signal Efficiency(%) of each cut for twin higgs model, LLP mass 7 GeV, lifetime of 1000 mm and decaying to 4τ leptons. (Cumulative Efficiency for all cuts applied after Trigger and MET cut are calculated with respect to events in acceptance and pass the MET and trigger cut and cut efficiency is calculated with respect to the previous cut. Acceptance is defined as when at least one LLP decays inside CSC.)

Selection	CSC-CSC		DT-DT		DT-CSC	
	cut eff	overall eff	cut eff	overall eff	cut eff	overall eff
acceptance	1.468	1.468	4.508	4.508	4.910	4.910
Trigger and MET	0.524	0.008	0.728	0.033	0.525	0.026
MET filters	99.00	99.00	96.29	96.29	98.03	98.03
$N_{jet} \geq 1$	95.83	94.87	96.75	93.16	96.25	94.36
$N_{\text{CSC+DT rings}} \leq 10$	100.00	94.87	100.00	93.16	100.00	94.36
DT noise veto	100.00	94.87	100.00	93.16	100.00	94.36
$N_{\text{cluster}} \geq 2$	22.30	21.16	26.43	24.63	16.02	15.11
DT cosmic veto	/	/	99.42	24.48	100.00	15.11
muon veto	99.96	21.15	96.87	23.72	98.88	14.94
jet veto	86.89	18.38	97.44	23.11	93.98	14.05
ME11/MB1 ratio	96.57	17.75	81.91	18.93	86.67	12.17
$N_{\text{minstationhits}} / N_{\text{maxstationhits}}$	/	/	91.78	17.37	97.56	11.88
time cut	91.01	16.15	/	/	100.00	11.88
time spread	92.57	14.95	/	/	97.54	11.58
$\Delta\phi(\text{cluster}, \text{MET})$	77.74	12	80.89	14.05	85.09	9.86
$\Delta R(\text{cluster1}, \text{cluster2})$	100.00	11.62	/	/	99.40	9.80
N_{rechits} cut	65.09	7.56	38.23	5.37	57.98	5.68

Table 39: Signal Efficiency(%) of each cut for twin higgs model, LLP mass 15 GeV, lifetime of 1000 mm and decaying to 4τ leptons. (Cumulative Efficiency for all cuts applied after Trigger and MET cut are calculated with respect to events in acceptance and pass the MET and trigger cut and cut efficiency is calculated with respect to the previous cut. Acceptance is defined as when at least one LLP decays inside CSC.)

Selection	CSC-CSC		DT-DT		DT-CSC	
	cut eff	overall eff	cut eff	overall eff	cut eff	overall eff
acceptance	2.120	2.120	6.429	6.429	6.484	6.484
Trigger and MET	0.872	0.018	1.043	0.067	0.738	0.048
MET filters	97.17	97.17	94.88	94.88	96.51	96.51
$N_{jet} \geq 1$	96.70	93.96	97.56	92.57	97.19	93.79
$N_{\text{CSC+DT rings}} \leq 10$	100.00	93.96	100.00	92.57	100.00	93.79
DT noise veto	100.00	93.96	99.95	92.52	99.97	93.76
$N_{\text{cluster}} \geq 2$	19.96	18.75	30.95	28.64	17.53	16.43
DT cosmic veto	/	/	99.80	28.58	100.00	16.43
muon veto	99.60	18.68	97.67	27.92	98.68	16.22
jet veto	91.82	17.15	95.60	26.69	95.64	15.51
ME11/MB1 ratio	96.62	16.57	81.34	21.71	87.76	13.61
$N_{\text{minstationhits}} / N_{\text{maxstationhits}}$	/	/	93.15	20.22	98.54	13.41
time cut	96.84	16.05	/	/	100.00	13.41
time spread	95.05	15.26	/	/	99.01	13.28
$\Delta\phi(\text{cluster}, \text{MET})$	88.89	14	90.97	18.40	97.04	12.89
$\Delta R(\text{cluster1}, \text{cluster2})$	98.94	13.42	/	/	100.00	12.89
N_{rechits} cut	62.79	8.42	38.75	7.13	60.63	7.81

Table 40: Signal Efficiency(%) of each cut for twin higgs model, LLP mass 40 GeV, lifetime of 1000 mm and decaying to 4τ leptons. (Cumulative Efficiency for all cuts applied after Trigger and MET cut are calculated with respect to events in acceptance and pass the MET and trigger cut and cut efficiency is calculated with respect to the previous cut. Acceptance is defined as when at least one LLP decays inside CSC.)

Selection	CSC-CSC		DT-DT		DT-CSC	
	cut eff	overall eff	cut eff	overall eff	cut eff	overall eff
acceptance	1.039	1.039	1.213	1.213	1.254	1.254
Trigger and MET	2.973	0.031	6.335	0.077	3.685	0.046
MET filters	96.54	96.54	91.34	91.34	93.95	93.95
$N_{jet} \geq 1$	96.37	93.04	97.65	89.20	96.48	90.64
$N_{\text{CSC+DT rings}} \leq 10$	100.00	93.04	100.00	89.20	100.00	90.64
DT noise veto	99.91	92.96	99.97	89.17	99.91	90.56
$N_{\text{cluster}} \geq 2$	20.80	19.34	23.35	20.82	15.11	13.68
DT cosmic veto	/	/	99.70	20.76	100.00	13.68
muon veto	99.97	19.33	98.46	20.44	98.92	13.54
jet veto	86.71	16.76	94.56	19.33	94.49	12.79
ME11/MB1 ratio	93.21	15.62	76.77	14.84	80.75	10.33
$N_{\text{minstationhits}} / N_{\text{maxstationhits}}$	/	/	91.00	13.50	99.57	10.28
time cut	96.40	15.06	/	/	100.00	10.28
time spread	95.86	14.44	/	/	99.22	10.20
$\Delta\phi(\text{cluster}, \text{MET})$	100.00	14	99.85	13.48	99.70	10.17
$\Delta R(\text{cluster1}, \text{cluster2})$	100.00	14.44	/	/	100.00	10.17
N_{rechits} cut	68.71	9.92	39.31	5.30	62.61	6.37

Table 41: Signal Efficiency(%) of each cut for twin higgs model, LLP mass 55 GeV, lifetime of 1000 mm and decaying to 4τ leptons. (Cumulative Efficiency for all cuts applied after Trigger and MET cut are calculated with respect to events in acceptance and pass the MET and trigger cut and cut efficiency is calculated with respect to the previous cut. Acceptance is defined as when at least one LLP decays inside CSC.)

Selection	CSC-CSC		DT-DT		DT-CSC	
	cut eff	overall eff	cut eff	overall eff	cut eff	overall eff
acceptance	0.362	0.362	0.290	0.290	0.234	0.234
Trigger and MET	9.880	0.036	24.828	0.072	15.954	0.037
MET filters	95.07	95.07	89.95	89.95	92.50	92.50
$N_{jet} \geq 1$	96.24	91.49	97.79	87.96	97.03	89.75
$N_{\text{CSC+DT rings}} \leq 10$	100.00	91.49	100.00	87.96	100.00	89.75
DT noise veto	100.00	91.49	99.95	87.91	99.88	89.64
$N_{\text{cluster}} \geq 2$	5.88	5.38	4.49	3.95	6.99	6.26
DT cosmic veto	/	/	100.00	3.95	100.00	6.26
muon veto	100.00	5.38	98.03	3.87	100.00	6.26
jet veto	60.22	3.24	94.42	3.66	91.04	5.70
ME11/MB1 ratio	84.96	2.75	75.52	2.76	70.34	4.01
$N_{\text{minstationhits}} / N_{\text{maxstationhits}}$	/	/	87.93	2.43	98.87	3.97
time cut	55.12	1.52	/	/	100.00	3.97
time spread	92.26	1.40	/	/	97.47	3.87
$\Delta\phi(\text{cluster}, \text{MET})$	91.79	1	100.00	2.43	100.00	3.87
$\Delta R(\text{cluster1}, \text{cluster2})$	89.93	1.16	/	/	100.00	3.87
N_{rechits} cut	65.22	0.75	41.47	1.01	65.40	2.53

Table 42: Signal Efficiency(%) of each cut for twin higgs model, LLP mass 0.4 GeV, lifetime of 10 mm and decaying to 2 electrons. (Cumulative Efficiency for all cuts applied after Trigger and MET cut are calculated with respect to events in acceptance and pass the MET and trigger cut and cut efficiency is calculated with respect to the previous cut. Acceptance is defined as when at least one LLP decays inside CSC.)

Selection	CSC-CSC		DT-DT		DT-CSC	
	cut eff	overall eff	cut eff	overall eff	cut eff	overall eff
acceptance	1.151	1.151	2.376	2.376	2.285	2.285
Trigger and MET	1.733	0.020	2.183	0.052	1.659	0.038
MET filters	99.08	99.08	86.62	86.62	92.77	92.77
$N_{jet} \geq 1$	96.14	95.25	97.62	84.55	96.98	89.97
$N_{\text{CSC+DT rings}} \leq 10$	100.00	95.25	100.00	84.55	100.00	89.97
DT noise veto	100.00	95.25	99.87	84.45	99.97	89.94
$N_{\text{cluster}} \geq 2$	8.86	8.44	21.52	18.18	10.14	9.12
DT cosmic veto	/	/	100.00	18.18	100.00	9.12
muon veto	100.00	8.44	99.30	18.05	99.68	9.09
jet veto	89.86	7.58	96.70	17.45	94.70	8.61
ME11/MB1 ratio	94.59	7.17	42.61	7.44	59.65	5.13
$N_{\text{minstationhits}} / N_{\text{maxstationhits}}$	/	/	100.00	7.44	100.00	5.13
time cut	84.92	6.09	/	/	100.00	5.13
time spread	98.01	5.97	/	/	98.68	5.07
$\Delta\phi(\text{cluster}, \text{MET})$	96.62	6	95.71	7.12	95.68	4.85
$\Delta R(\text{cluster1}, \text{cluster2})$	100.00	5.77	/	/	100.00	4.85
N_{rechits} cut	79.34	4.58	52.70	3.75	72.18	3.50

Table 43: Signal Efficiency(%) of each cut for twin higgs model, LLP mass 0.4 GeV, lifetime of 10 mm and decaying to 2 photons. (Cumulative Efficiency for all cuts applied after Trigger and MET cut are calculated with respect to events in acceptance and pass the MET and trigger cut and cut efficiency is calculated with respect to the previous cut. Acceptance is defined as when at least one LLP decays inside CSC.)

Selection	CSC-CSC		DT-DT		DT-CSC	
	cut eff	overall eff	cut eff	overall eff	cut eff	overall eff
acceptance	1.153	1.153	2.380	2.380	2.285	2.285
Trigger and MET	1.678	0.019	2.217	0.053	1.647	0.038
MET filters	98.79	98.79	86.76	86.76	93.89	93.89
$N_{jet} \geq 1$	97.21	96.04	97.71	84.77	97.44	91.49
$N_{\text{CSC+DT rings}} \leq 10$	100.00	96.04	100.00	84.77	100.00	91.49
DT noise veto	100.00	96.04	99.97	84.74	100.00	91.49
$N_{cluster} \geq 2$	9.12	8.76	20.86	17.68	9.94	9.09
DT cosmic veto	/	/	100.00	17.68	100.00	9.09
muon veto	100.00	8.76	99.57	17.60	100.00	9.09
jet veto	82.41	7.22	96.91	17.06	94.65	8.60
ME11/MB1 ratio	91.27	6.59	42.56	7.26	55.38	4.76
$N_{\text{minstationhits}} / N_{\text{maxstationhits}}$	/	/	99.96	7.26	100.00	4.76
time cut	89.95	5.93	/	/	100.00	4.76
time spread	91.68	5.43	/	/	100.00	4.76
$\Delta\phi(\text{cluster}, \text{MET})$	93.68	5	97.92	7.11	98.75	4.71
$\Delta R(\text{cluster1}, \text{cluster2})$	100.00	5.09	/	/	100.00	4.71
N_{rechits} cut	77.69	3.95	60.29	4.28	63.46	2.99

Table 44: Signal Efficiency(%) of each cut for twin higgs model, LLP mass 1.5 GeV, lifetime of 187 mm and decaying to $K^+ K^-$. (Cumulative Efficiency for all cuts applied after Trigger and MET cut are calculated with respect to events in acceptance and pass the MET and trigger cut and cut efficiency is calculated with respect to the previous cut. Acceptance is defined as when at least one LLP decays inside CSC.)

Selection	CSC-CSC		DT-DT		DT-CSC	
	cut eff	overall eff	cut eff	overall eff	cut eff	overall eff
acceptance	1.632	1.632	5.098	5.098	5.457	5.457
Trigger and MET	0.569	0.009	0.703	0.036	0.511	0.028
MET filters	100.00	100.00	95.82	95.82	99.39	99.39
$N_{jet} \geq 1$	99.16	99.16	97.83	93.75	96.95	96.36
$N_{\text{CSC+DT rings}} \leq 10$	100.00	99.16	100.00	93.75	100.00	96.36
DT noise veto	100.00	99.16	100.00	93.75	100.00	96.36
$N_{\text{cluster}} \geq 2$	40.79	40.44	43.71	40.98	37.77	36.39
DT cosmic veto	/	/	99.65	40.83	100.00	36.39
muon veto	100.00	40.44	98.77	40.33	99.10	36.06
jet veto	92.71	37.49	95.52	38.53	94.33	34.02
ME11/MB1 ratio	94.20	35.32	95.57	36.82	95.22	32.39
$N_{\text{minstationhits}} / N_{\text{maxstationhits}}$	/	/	100.00	36.82	100.00	32.39
time cut	96.94	34.24	/	/	100.00	32.39
time spread	100.00	34.24	/	/	99.00	32.07
$\Delta\phi(\text{cluster}, \text{MET})$	69.58	24	79.34	29.21	77.27	24.78
$\Delta R(\text{cluster1}, \text{cluster2})$	100.00	23.82	/	/	100.00	24.78
N_{rechits} cut	92.33	22.00	81.38	23.77	84.03	20.82

Table 45: Signal Efficiency(%) of each cut for twin higgs model, LLP mass 1.5 GeV, lifetime of 187 mm and decaying to 2 K^0 . (Cumulative Efficiency for all cuts applied after Trigger and MET cut are calculated with respect to events in acceptance and pass the MET and trigger cut and cut efficiency is calculated with respect to the previous cut. Acceptance is defined as when at least one LLP decays inside CSC.)

Selection	CSC-CSC		DT-DT		DT-CSC	
	cut eff	overall eff	cut eff	overall eff	cut eff	overall eff
acceptance	1.637	1.637	5.076	5.076	5.466	5.466
Trigger and MET	0.546	0.009	0.674	0.034	0.503	0.028
MET filters	99.67	99.67	97.62	97.62	98.69	98.69
$N_{jet} \geq 1$	97.52	97.20	96.55	94.25	95.69	94.45
$N_{\text{CSC+DT rings}} \leq 10$	100.00	97.20	100.00	94.25	100.00	94.45
DT noise veto	100.00	97.20	100.00	94.25	100.00	94.45
$N_{\text{cluster}} \geq 2$	39.95	38.83	41.43	39.05	35.54	33.56
DT cosmic veto	/	/	99.52	38.86	100.00	33.56
muon veto	100.00	38.83	98.64	38.33	99.08	33.25
jet veto	89.12	34.60	96.10	36.84	94.96	31.58
ME11/MB1 ratio	95.26	32.96	91.74	33.79	94.18	29.74
$N_{\text{minstationhits}} / N_{\text{maxstationhits}}$	/	/	100.00	33.79	100.00	29.74
time cut	98.49	32.47	/	/	100.00	29.74
time spread	97.53	31.66	/	/	98.07	29.16
$\Delta\phi(\text{cluster}, \text{MET})$	76.08	24	77.23	26.10	88.16	25.71
$\Delta R(\text{cluster1}, \text{cluster2})$	100.00	24.09	/	/	100.00	25.71
N_{rechits} cut	87.22	21.01	74.61	19.47	81.90	21.06

Table 46: Signal Efficiency(%) of each cut for twin higgs model, LLP mass 1 GeV, lifetime of 125 mm and decaying to $2\pi^0$. (Cumulative Efficiency for all cuts applied after Trigger and MET cut are calculated with respect to events in acceptance and pass the MET and trigger cut and cut efficiency is calculated with respect to the previous cut. Acceptance is defined as when at least one LLP decays inside CSC.)

Selection	CSC-CSC		DT-DT		DT-CSC	
	cut eff	overall eff	cut eff	overall eff	cut eff	overall eff
acceptance	1.623	1.623	5.062	5.062	5.449	5.449
Trigger and MET	0.530	0.009	0.694	0.035	0.508	0.028
MET filters	99.01	99.01	92.18	92.18	95.45	95.45
$N_{jet} \geq 1$	96.71	95.75	97.31	89.70	96.86	92.45
$N_{\text{CSC+DT rings}} \leq 10$	100.00	95.75	100.00	89.70	100.00	92.45
DT noise veto	99.87	95.63	99.95	89.66	99.96	92.41
$N_{\text{cluster}} \geq 2$	8.22	7.86	17.18	15.41	8.89	8.22
DT cosmic veto	/	/	100.00	15.41	100.00	8.22
muon veto	100.00	7.86	99.82	15.38	100.00	8.22
jet veto	80.98	6.37	97.42	14.98	96.29	7.91
ME11/MB1 ratio	90.62	5.77	51.03	7.64	66.52	5.26
$N_{\text{minstationhits}} / N_{\text{maxstationhits}}$	/	/	100.00	7.64	100.00	5.26
time cut	88.66	5.12	/	/	98.86	5.20
time spread	100.00	5.12	/	/	98.78	5.14
$\Delta\phi(\text{cluster}, \text{MET})$	84.90	4	85.57	6.54	88.63	4.56
$\Delta R(\text{cluster1}, \text{cluster2})$	100.00	4.34	/	/	100.00	4.56
N_{rechits} cut	81.58	3.54	54.17	3.54	71.04	3.24

Table 47: Signal Efficiency(%) of each cut for twin higgs model, LLP mass 1 GeV, lifetime of 125 mm and decaying to $\pi^+\pi^-$. (Cumulative Efficiency for all cuts applied after Trigger and MET cut are calculated with respect to events in acceptance and pass the MET and trigger cut and cut efficiency is calculated with respect to the previous cut. Acceptance is defined as when at least one LLP decays inside CSC.)

Selection	CSC-CSC		DT-DT		DT-CSC	
	cut eff	overall eff	cut eff	overall eff	cut eff	overall eff
acceptance	1.626	1.626	5.054	5.054	5.445	5.445
Trigger and MET	0.533	0.009	0.668	0.034	0.497	0.027
MET filters	99.24	99.24	97.40	97.40	98.33	98.33
$N_{jet} \geq 1$	96.18	95.45	97.03	94.51	96.62	95.00
$N_{\text{CSC+DT rings}} \leq 10$	100.00	95.45	100.00	94.51	100.00	95.00
DT noise veto	100.00	95.45	100.00	94.51	100.00	95.00
$N_{cluster} \geq 2$	35.84	34.21	43.00	40.64	31.03	29.48
DT cosmic veto	/	/	99.96	40.63	100.00	29.48
muon veto	100.00	34.21	98.46	40.00	98.60	29.07
jet veto	88.22	30.18	95.13	38.05	93.90	27.29
ME11/MB1 ratio	96.28	29.05	91.52	34.83	94.53	25.80
$N_{\text{minstationhits}} / N_{\text{maxstationhits}}$	/	/	99.95	34.81	100.00	25.80
time cut	98.55	28.63	/	/	100.00	25.80
time spread	99.22	28.41	/	/	98.62	25.44
$\Delta\phi(\text{cluster}, \text{MET})$	81.29	23	79.06	27.52	89.32	22.72
$\Delta R(\text{cluster1}, \text{cluster2})$	100.00	23.09	/	/	100.00	22.72
N_{rechits} cut	81.93	18.92	73.35	20.18	78.49	17.84

Table 48: Signal Efficiency(%) of each cut for higgs portal dark shower model, $x_{i0} = 2.5$, $x_{iL} = 1$, LLP mass 15 GeV and lifetime of 5000 mm. (Cumulative Efficiency for all cuts applied after Trigger and MET cut are calculated with respect to events passing the MET and trigger cut and cut efficiency is calculated with respect to the previous cut.)

Selection	CSC-CSC		DT-DT		DT-CSC	
	cut eff	overall eff	cut eff	overall eff	cut eff	overall eff
Trigger and MET	1.012	1.012	1.012	1.012	1.012	1.012
MET filters	98.38	98.38	98.38	98.38	98.38	98.38
$N_{jet} \geq 1$	97.44	95.86	97.44	95.86	97.44	95.86
$N_{\text{CSC+DT rings}} \leq 10$	100.00	95.86	100.00	95.86	100.00	95.86
DT noise veto	100.00	95.86	100.00	95.86	100.00	95.86
$N_{cluster} \geq 2$	1.39	1.33	4.40	4.21	2.66	2.55
DT cosmic veto	/	/	96.58	4.07	99.74	2.54
muon veto	99.91	1.33	95.55	3.89	98.52	2.50
jet veto	73.66	0.98	83.09	3.23	71.85	1.80
ME11/MB1 ratio	89.71	0.88	80.64	2.60	81.22	1.46
$N_{\text{minstationhits}} / N_{\text{maxstationhits}}$	/	/	89.34	2.33	98.55	1.44
time cut	74.37	0.65	/	/	75.77	1.09
time spread	91.25	0.60	/	/	96.45	1.05
$\Delta\phi(\text{cluster}, \text{MET})$	84.04	1	80.24	1.87	91.19	0.96
$\Delta R(\text{cluster1}, \text{cluster2})$	100.00	0.50	/	/	99.07	0.95
N_{rechits} cut	62.93	0.32	41.54	0.78	60.15	0.57

Table 49: Signal Efficiency(%) of each cut for higgs portal dark shower model, $x_{i0} = 2.5$, $x_{iL} = 2.5$, LLP mass 15 GeV and lifetime of 5000 mm. (Cumulative Efficiency for all cuts applied after Trigger and MET cut are calculated with respect to events passing the MET and trigger cut and cut efficiency is calculated with respect to the previous cut.)

Selection	CSC-CSC		DT-DT		DT-CSC	
	cut eff	overall eff	cut eff	overall eff	cut eff	overall eff
Trigger and MET	1.065	1.065	1.065	1.065	1.065	1.065
MET filters	98.76	98.76	98.76	98.76	98.76	98.76
$N_{jet} \geq 1$	97.20	96.00	97.20	96.00	97.20	96.00
$N_{\text{CSC+DT rings}} \leq 10$	100.00	96.00	100.00	96.00	100.00	96.00
DT noise veto	100.00	95.99	100.00	95.99	100.00	95.99
$N_{cluster} \geq 2$	1.08	1.04	3.48	3.34	1.95	1.87
DT cosmic veto	/	/	97.24	3.25	99.73	1.86
muon veto	100.00	1.04	94.16	3.06	98.59	1.84
jet veto	71.28	0.74	83.26	2.55	72.87	1.34
ME11/MB1 ratio	87.88	0.65	80.77	2.06	81.55	1.09
$N_{\text{minstationhits}} / N_{\text{maxstationhits}}$	/	/	88.35	1.82	99.21	1.08
time cut	65.76	0.43	/	/	74.26	0.80
time spread	91.41	0.39	/	/	95.55	0.77
$\Delta\phi(\text{cluster}, \text{MET})$	89.03	0	75.03	1.36	89.63	0.69
$\Delta R(\text{cluster1}, \text{cluster2})$	99.07	0.35	/	/	99.45	0.69
N_{rechits} cut	68.56	0.24	39.40	0.54	60.86	0.42

Table 50: Signal Efficiency(%) of each cut for higgs portal dark shower model, $x_{i0} = 1$, $x_{iL} = 1$, LLP mass 15 GeV and lifetime of 5000 mm. (Cumulative Efficiency for all cuts applied after Trigger and MET cut are calculated with respect to events passing the MET and trigger cut and cut efficiency is calculated with respect to the previous cut.)

Selection	CSC-CSC		DT-DT		DT-CSC	
	cut eff	overall eff	cut eff	overall eff	cut eff	overall eff
Trigger and MET	1.233	1.233	1.233	1.233	1.233	1.233
MET filters	99.57	99.57	99.57	99.57	99.57	99.57
$N_{jet} \geq 1$	96.91	96.50	96.91	96.50	96.91	96.50
$N_{\text{CSC+DT rings}} \leq 10$	100.00	96.50	100.00	96.50	100.00	96.50
DT noise veto	100.00	96.49	100.00	96.49	100.00	96.49
$N_{cluster} \geq 2$	0.31	0.30	0.70	0.68	0.43	0.42
DT cosmic veto	/	/	94.51	0.64	100.00	0.42
muon veto	100.00	0.30	92.96	0.59	97.13	0.41
jet veto	56.10	0.17	69.94	0.42	62.08	0.25
ME11/MB1 ratio	81.72	0.14	82.00	0.34	76.74	0.19
$N_{\text{minstationhits}} / N_{\text{maxstationhits}}$	/	/	75.73	0.26	97.90	0.19
time cut	42.95	0.06	/	/	47.34	0.09
time spread	90.39	0.05	/	/	93.18	0.08
$\Delta\phi(\text{cluster}, \text{MET})$	93.82	0	48.29	0.12	90.84	0.08
$\Delta R(\text{cluster1}, \text{cluster2})$	91.38	0.05	/	/	98.68	0.08
N_{rechits} cut	69.86	0.03	28.03	0.03	59.69	0.04

Table 51: Signal Efficiency(%) of each cut for gluon portal dark shower model, $x_{i0} = 2.5$, $x_{iL} = 1$, LLP mass 15 GeV and lifetime of 5000 mm. (Cumulative Efficiency for all cuts applied after Trigger and MET cut are calculated with respect to events passing the MET and trigger cut and cut efficiency is calculated with respect to the previous cut.)

Selection	CSC-CSC		DT-DT		DT-CSC	
	cut eff	overall eff	cut eff	overall eff	cut eff	overall eff
Trigger and MET	1.065	1.065	1.065	1.065	1.065	1.065
MET filters	98.36	98.36	98.36	98.36	98.36	98.36
$N_{jet} \geq 1$	97.38	95.78	97.38	95.78	97.38	95.78
$N_{\text{CSC+DT rings}} \leq 10$	100.00	95.78	100.00	95.78	100.00	95.78
DT noise veto	99.99	95.77	99.99	95.77	99.99	95.77
$N_{cluster} \geq 2$	1.45	1.39	4.21	4.03	2.87	2.75
DT cosmic veto	/	/	98.69	3.98	100.00	2.75
muon veto	99.85	1.39	96.12	3.83	98.86	2.72
jet veto	72.72	1.01	83.50	3.19	71.92	1.96
ME11/MB1 ratio	87.84	0.89	78.51	2.51	79.86	1.56
$N_{\text{minstationhits}} / N_{\text{maxstationhits}}$	/	/	94.14	2.36	99.52	1.55
time cut	72.68	0.64	/	/	77.48	1.20
time spread	92.47	0.60	/	/	95.37	1.15
$\Delta\phi(\text{cluster}, \text{MET})$	89.15	1	77.03	1.82	89.76	1.03
$\Delta R(\text{cluster1}, \text{cluster2})$	98.46	0.52	/	/	99.48	1.03
N_{rechits} cut	69.99	0.37	44.24	0.80	69.18	0.71

Table 52: Signal Efficiency(%) of each cut for gluon portal dark shower model, $x_{i0} = 2.5$, $x_{iL} = 2.5$, LLP mass 15 GeV and lifetime of 5000 mm. (Cumulative Efficiency for all cuts applied after Trigger and MET cut are calculated with respect to events passing the MET and trigger cut and cut efficiency is calculated with respect to the previous cut.)

Selection	CSC-CSC		DT-DT		DT-CSC	
	cut eff	overall eff	cut eff	overall eff	cut eff	overall eff
Trigger and MET	1.128	1.128	1.128	1.128	1.128	1.128
MET filters	98.71	98.71	98.71	98.71	98.71	98.71
$N_{jet} \geq 1$	97.30	96.05	97.30	96.05	97.30	96.05
$N_{\text{CSC+DT rings}} \leq 10$	100.00	96.05	100.00	96.05	100.00	96.05
DT noise veto	99.99	96.04	99.99	96.04	99.99	96.04
$N_{cluster} \geq 2$	1.18	1.13	3.45	3.32	2.34	2.24
DT cosmic veto	/	/	98.58	3.27	99.90	2.24
muon veto	99.85	1.13	94.97	3.10	98.55	2.21
jet veto	70.01	0.79	83.70	2.60	75.88	1.68
ME11/MB1 ratio	86.07	0.68	80.68	2.10	81.96	1.37
$N_{\text{minstationhits}} / N_{\text{maxstationhits}}$	/	/	93.47	1.96	99.29	1.36
time cut	67.77	0.46	/	/	74.70	1.02
time spread	91.55	0.42	/	/	95.01	0.97
$\Delta\phi(\text{cluster}, \text{MET})$	84.51	0	74.78	1.47	86.79	0.84
$\Delta R(\text{cluster1}, \text{cluster2})$	99.41	0.35	/	/	99.67	0.84
N_{rechits} cut	70.96	0.25	51.27	0.75	66.01	0.55

Table 53: Signal Efficiency(%) of each cut for gluon portal dark shower model, $x_{i0} = 1$, $x_{iL} = 1$, LLP mass 15 GeV and lifetime of 5000 mm. (Cumulative Efficiency for all cuts applied after Trigger and MET cut are calculated with respect to events passing the MET and trigger cut and cut efficiency is calculated with respect to the previous cut.)

Selection	CSC-CSC		DT-DT		DT-CSC	
	cut eff	overall eff	cut eff	overall eff	cut eff	overall eff
Trigger and MET	1.326	1.326	1.326	1.326	1.326	1.326
MET filters	99.50	99.50	99.50	99.50	99.50	99.50
$N_{jet} \geq 1$	97.10	96.62	97.10	96.62	97.10	96.62
$N_{\text{CSC+DT rings}} \leq 10$	100.00	96.62	100.00	96.62	100.00	96.62
DT noise veto	100.00	96.62	100.00	96.62	100.00	96.62
$N_{cluster} \geq 2$	0.35	0.34	0.78	0.75	0.50	0.49
DT cosmic veto	/	/	97.35	0.73	100.00	0.49
muon veto	99.76	0.34	89.08	0.65	98.38	0.48
jet veto	61.14	0.21	65.74	0.43	63.16	0.30
ME11/MB1 ratio	79.77	0.17	78.73	0.34	78.72	0.24
$N_{\text{minstationhits}} / N_{\text{maxstationhits}}$	/	/	82.27	0.28	99.57	0.24
time cut	37.91	0.06	/	/	47.55	0.11
time spread	83.29	0.05	/	/	94.58	0.11
$\Delta\phi(\text{cluster}, \text{MET})$	80.96	0	56.08	0.16	82.16	0.09
$\Delta R(\text{cluster1}, \text{cluster2})$	96.60	0.04	/	/	100.00	0.09
N_{rechits} cut	77.03	0.03	37.82	0.06	55.21	0.05

Table 54: Signal Efficiency(%) of each cut for vector portal dark shower model, $x_{i0} = 1$, $x_{iL} = 1$, LLP mass 15 GeV and lifetime of 5000 mm. (Cumulative Efficiency for all cuts applied after Trigger and MET cut are calculated with respect to events passing the MET and trigger cut and cut efficiency is calculated with respect to the previous cut.)

Selection	CSC-CSC		DT-DT		DT-CSC	
	cut eff	overall eff	cut eff	overall eff	cut eff	overall eff
Trigger and MET	1.131	1.131	1.131	1.131	1.131	1.131
MET filters	98.71	98.71	98.71	98.71	98.71	98.71
$N_{jet} \geq 1$	97.23	95.98	97.23	95.98	97.23	95.98
$N_{\text{CSC+DT rings}} \leq 10$	100.00	95.98	100.00	95.98	100.00	95.98
DT noise veto	100.00	95.98	100.00	95.98	100.00	95.98
$N_{cluster} \geq 2$	0.75	0.72	3.34	3.21	1.50	1.44
DT cosmic veto	/	/	95.89	3.08	99.94	1.44
muon veto	99.33	0.72	90.26	2.78	97.65	1.40
jet veto	67.09	0.48	84.36	2.34	67.37	0.95
ME11/MB1 ratio	87.38	0.42	83.10	1.95	76.92	0.73
$N_{\text{minstationhits}} / N_{\text{maxstationhits}}$	/	/	70.44	1.37	94.17	0.68
time cut	60.80	0.26	/	/	67.06	0.46
time spread	92.11	0.24	/	/	96.11	0.44
$\Delta\phi(\text{cluster}, \text{MET})$	88.52	0	72.96	1.00	88.10	0.39
$\Delta R(\text{cluster1}, \text{cluster2})$	97.93	0.20	/	/	99.41	0.39
N_{rechits} cut	59.79	0.12	26.08	0.26	47.13	0.18

Table 55: Signal Efficiency(%) of each cut for photon portal dark shower model, $x_{i0} = 2.5$, $x_{iL} = 1$, LLP mass 15 GeV and lifetime of 5000 mm. (Cumulative Efficiency for all cuts applied after Trigger and MET cut are calculated with respect to events passing the MET and trigger cut and cut efficiency is calculated with respect to the previous cut.)

Selection	CSC-CSC		DT-DT		DT-CSC	
	cut eff	overall eff	cut eff	overall eff	cut eff	overall eff
Trigger and MET	1.014	1.014	1.014	1.014	1.014	1.014
MET filters	95.91	95.91	95.91	95.91	95.91	95.91
$N_{jet} \geq 1$	97.30	93.32	97.30	93.32	97.30	93.32
$N_{\text{CSC+DT rings}} \leq 10$	100.00	93.32	100.00	93.32	100.00	93.32
DT noise veto	100.00	93.32	100.00	93.32	100.00	93.32
$N_{cluster} \geq 2$	0.62	0.58	1.88	1.75	1.14	1.07
DT cosmic veto	/	/	99.52	1.74	100.00	1.07
muon veto	100.00	0.58	94.12	1.64	98.55	1.05
jet veto	69.14	0.40	76.46	1.25	68.53	0.72
ME11/MB1 ratio	84.48	0.34	48.59	0.61	59.98	0.43
$N_{\text{minstationhits}} / N_{\text{maxstationhits}}$	/	/	86.53	0.53	99.14	0.43
time cut	59.48	0.20	/	/	68.83	0.29
time spread	87.16	0.18	/	/	90.74	0.27
$\Delta\phi(\text{cluster}, \text{MET})$	75.64	0	66.96	0.35	84.23	0.23
$\Delta R(\text{cluster1}, \text{cluster2})$	95.83	0.13	/	/	99.92	0.23
N_{rechits} cut	59.89	0.08	34.24	0.12	66.32	0.15

Table 56: Signal Efficiency(%) of each cut for photon portal dark shower model, $x_{i0} = 2.5$, $x_{iL} = 2.5$, LLP mass 15 GeV and lifetime of 5000 mm. (Cumulative Efficiency for all cuts applied after Trigger and MET cut are calculated with respect to events passing the MET and trigger cut and cut efficiency is calculated with respect to the previous cut.)

Selection	CSC-CSC		DT-DT		DT-CSC	
	cut eff	overall eff	cut eff	overall eff	cut eff	overall eff
Trigger and MET	1.082	1.082	1.082	1.082	1.082	1.082
MET filters	96.78	96.78	96.78	96.78	96.78	96.78
$N_{jet} \geq 1$	97.18	94.05	97.18	94.05	97.18	94.05
$N_{\text{CSC+DT rings}} \leq 10$	100.00	94.05	100.00	94.05	100.00	94.05
DT noise veto	99.99	94.04	99.99	94.04	99.99	94.04
$N_{cluster} \geq 2$	0.45	0.42	1.50	1.41	0.93	0.87
DT cosmic veto	/	/	99.37	1.40	99.96	0.87
muon veto	100.00	0.42	92.11	1.29	98.49	0.86
jet veto	63.92	0.27	73.67	0.95	65.67	0.56
ME11/MB1 ratio	82.50	0.22	50.45	0.48	57.66	0.33
$N_{\text{minstationhits}} / N_{\text{maxstationhits}}$	/	/	85.20	0.41	99.98	0.33
time cut	51.57	0.12	/	/	49.63	0.16
time spread	91.16	0.11	/	/	96.44	0.16
$\Delta\phi(\text{cluster}, \text{MET})$	82.13	0	62.32	0.25	74.58	0.12
$\Delta R(\text{cluster1}, \text{cluster2})$	97.03	0.08	/	/	99.10	0.12
N_{rechits} cut	71.83	0.06	36.89	0.09	62.68	0.07

Table 57: Signal Efficiency(%) of each cut for photon portal dark shower model, $x_{i0} = 1$, $x_{iL} = 1$, LLP mass 15 GeV and lifetime of 5000 mm. (Cumulative Efficiency for all cuts applied after Trigger and MET cut are calculated with respect to events passing the MET and trigger cut and cut efficiency is calculated with respect to the previous cut.)

Selection	CSC-CSC		DT-DT		DT-CSC	
	cut eff	overall eff	cut eff	overall eff	cut eff	overall eff
Trigger and MET	1.306	1.306	1.306	1.306	1.306	1.306
MET filters	98.91	98.91	98.91	98.91	98.91	98.91
$N_{jet} \geq 1$	97.13	96.08	97.13	96.08	97.13	96.08
$N_{\text{CSC+DT rings}} \leq 10$	100.00	96.08	100.00	96.08	100.00	96.08
DT noise veto	100.00	96.08	100.00	96.08	100.00	96.08
$N_{cluster} \geq 2$	0.19	0.19	0.44	0.42	0.21	0.20
DT cosmic veto	/	/	98.33	0.41	100.00	0.20
muon veto	99.54	0.19	88.94	0.37	98.31	0.20
jet veto	51.34	0.10	60.33	0.22	59.96	0.12
ME11/MB1 ratio	77.82	0.07	61.14	0.14	57.40	0.07
$N_{\text{minstationhits}} / N_{\text{maxstationhits}}$	/	/	64.71	0.09	97.33	0.07
time cut	25.96	0.02	/	/	32.08	0.02
time spread	57.18	0.01	/	/	97.43	0.02
$\Delta\phi(\text{cluster}, \text{MET})$	47.54	0	42.51	0.04	88.04	0.02
$\Delta R(\text{cluster1}, \text{cluster2})$	100.00	0.01	/	/	91.66	0.02
N_{rechits} cut	92.70	0.00	22.60	0.01	60.16	0.01

Table 58: Signal Efficiency(%) of each cut for darkphoton portal dark shower model, $x_{i0} = 2.5$, $x_{iL} = 1$, LLP mass 15 GeV and lifetime of 5000 mm. (Cumulative Efficiency for all cuts applied after Trigger and MET cut are calculated with respect to events passing the MET and trigger cut and cut efficiency is calculated with respect to the previous cut.)

Selection	CSC-CSC		DT-DT		DT-CSC	
	cut eff	overall eff	cut eff	overall eff	cut eff	overall eff
Trigger and MET	0.437	0.437	0.437	0.437	0.437	0.437
MET filters	99.46	99.46	99.46	99.46	99.46	99.46
$N_{jet} \geq 1$	98.15	97.62	98.15	97.62	98.15	97.62
$N_{\text{CSC+DT rings}} \leq 10$	100.00	97.62	100.00	97.62	100.00	97.62
DT noise veto	100.00	97.62	100.00	97.62	100.00	97.62
$N_{cluster} \geq 2$	2.50	2.44	11.16	10.90	3.51	3.42
DT cosmic veto	/	/	95.78	10.44	99.69	3.41
muon veto	100.00	2.44	44.63	4.66	64.77	2.21
jet veto	49.35	1.20	70.81	3.30	53.15	1.18
ME11/MB1 ratio	89.46	1.08	86.93	2.87	79.84	0.94
$N_{\text{minstationhits}} / N_{\text{maxstationhits}}$	/	/	62.52	1.79	88.12	0.83
time cut	77.04	0.83	/	/	82.28	0.68
time spread	92.48	0.77	/	/	95.38	0.65
$\Delta\phi(\text{cluster}, \text{MET})$	79.95	1	62.87	1.13	85.59	0.56
$\Delta R(\text{cluster1}, \text{cluster2})$	97.25	0.60	/	/	98.66	0.55
N_{rechits} cut	39.62	0.24	13.10	0.15	32.83	0.18

Table 59: Signal Efficiency(%) of each cut for darkphoton portal dark shower model, $x_{i0} = 2.5$, $x_{iL} = 2.5$, LLP mass 15 GeV and lifetime of 5000 mm. (Cumulative Efficiency for all cuts applied after Trigger and MET cut are calculated with respect to events passing the MET and trigger cut and cut efficiency is calculated with respect to the previous cut.)

Selection	CSC-CSC		DT-DT		DT-CSC	
	cut eff	overall eff	cut eff	overall eff	cut eff	overall eff
Trigger and MET	0.510	0.510	0.510	0.510	0.510	0.510
MET filters	99.43	99.43	99.43	99.43	99.43	99.43
$N_{jet} \geq 1$	97.87	97.32	97.87	97.32	97.87	97.32
$N_{\text{CSC+DT rings}} \leq 10$	100.00	97.32	100.00	97.32	100.00	97.32
DT noise veto	99.99	97.31	99.99	97.31	99.99	97.31
$N_{cluster} \geq 2$	1.96	1.91	9.31	9.06	2.87	2.79
DT cosmic veto	/	/	95.53	8.65	99.74	2.78
muon veto	99.40	1.89	43.14	3.73	62.66	1.75
jet veto	50.64	0.96	73.67	2.75	57.14	1.00
ME11/MB1 ratio	87.10	0.84	83.98	2.31	79.30	0.79
$N_{\text{minstationhits}} / N_{\text{maxstationhits}}$	/	/	62.97	1.45	91.04	0.72
time cut	77.27	0.65	/	/	84.27	0.61
time spread	89.15	0.58	/	/	95.35	0.58
$\Delta\phi(\text{cluster}, \text{MET})$	74.55	0	57.72	0.84	78.61	0.45
$\Delta R(\text{cluster1}, \text{cluster2})$	99.36	0.43	/	/	100.00	0.45
N_{rechits} cut	39.48	0.17	12.95	0.11	42.76	0.19

Table 60: Signal Efficiency(%) of each cut for darkphoton portal dark shower model, $x_{i0} = 1$, $x_{iL} = 1$, LLP mass 15 GeV and lifetime of 5000 mm. (Cumulative Efficiency for all cuts applied after Trigger and MET cut are calculated with respect to events passing the MET and trigger cut and cut efficiency is calculated with respect to the previous cut.)

Selection	CSC-CSC		DT-DT		DT-CSC	
	cut eff	overall eff	cut eff	overall eff	cut eff	overall eff
Trigger and MET	1.076	1.076	1.076	1.076	1.076	1.076
MET filters	99.80	99.80	99.80	99.80	99.80	99.80
$N_{jet} \geq 1$	97.17	96.98	97.17	96.98	97.17	96.98
$N_{\text{CSC+DT rings}} \leq 10$	100.00	96.98	100.00	96.98	100.00	96.98
DT noise veto	100.00	96.97	100.00	96.97	100.00	96.97
$N_{cluster} \geq 2$	0.43	0.42	2.49	2.42	0.67	0.65
DT cosmic veto	/	/	94.56	2.29	99.50	0.64
muon veto	99.78	0.42	49.45	1.13	68.72	0.44
jet veto	56.38	0.24	76.76	0.87	55.13	0.24
ME11/MB1 ratio	84.84	0.20	85.16	0.74	78.10	0.19
$N_{\text{minstationhits}} / N_{\text{maxstationhits}}$	/	/	57.28	0.42	88.11	0.17
time cut	57.00	0.11	/	/	63.69	0.11
time spread	85.62	0.10	/	/	90.50	0.10
$\Delta\phi(\text{cluster}, \text{MET})$	67.85	0	50.27	0.21	84.44	0.08
$\Delta R(\text{cluster1}, \text{cluster2})$	100.00	0.07	/	/	100.00	0.08
N_{rechits} cut	22.85	0.02	10.96	0.02	38.43	0.03

1050 B Signal and Data Distributions

1051 A few sanity plots for the signal and data distributions for cluster-level variables are shown
 1052 in this section. For signal, all clusters are required to match to an LLP and two clusters are
 1053 required per event. For data, two clusters are required per event, but the N_{rechits} are < 100 (80)
 1054 for CSC (DT) clusters. Clusters are required to pass the jet veto, muon veto and ME11/12 or
 MB1 veto.

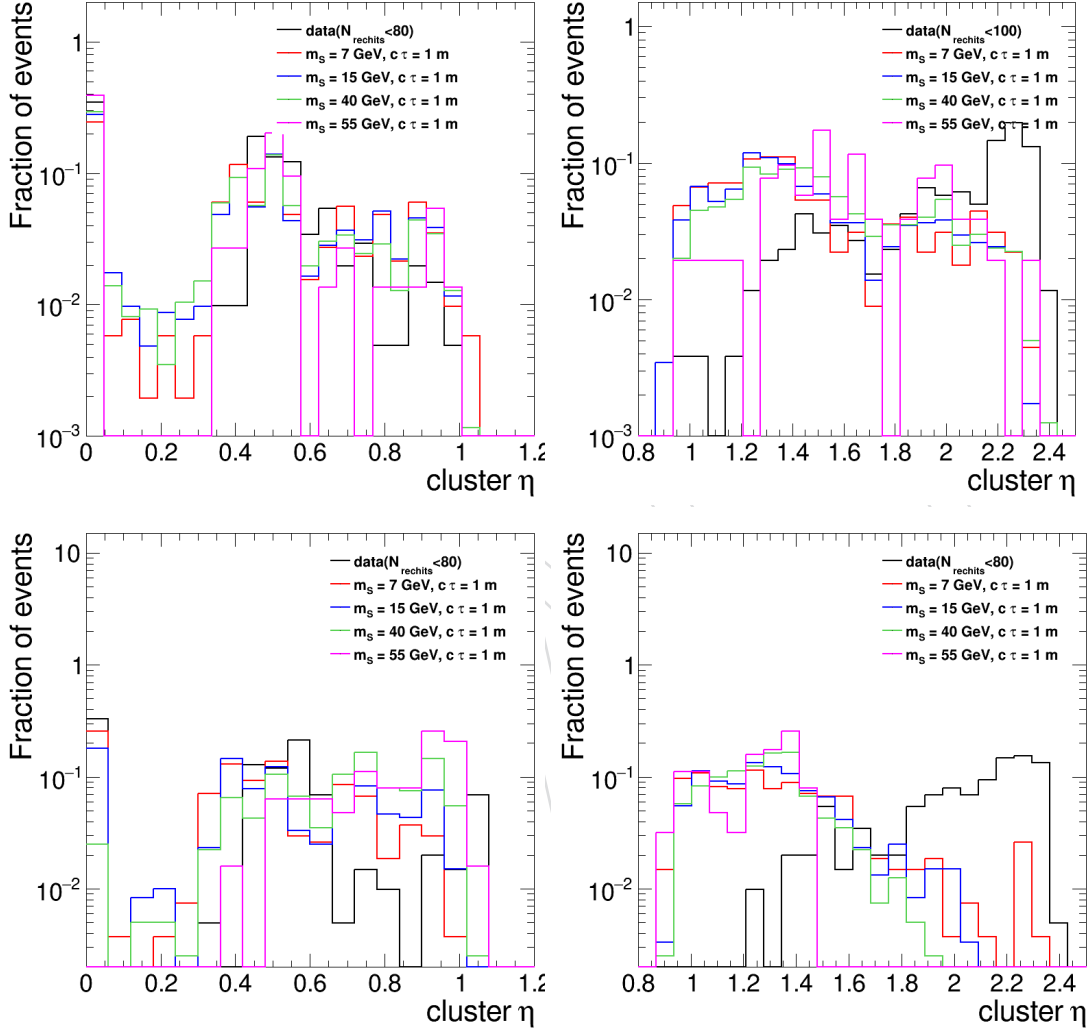


Figure 57: The cluster η distributions are shown. The η of both clusters are shown for DT-DT (top left) and CSC-CSC (top right) category. The cluster η for DT (bottom left) and CSC (bottom right) clusters are shown in separate plots for DT-CSC category.

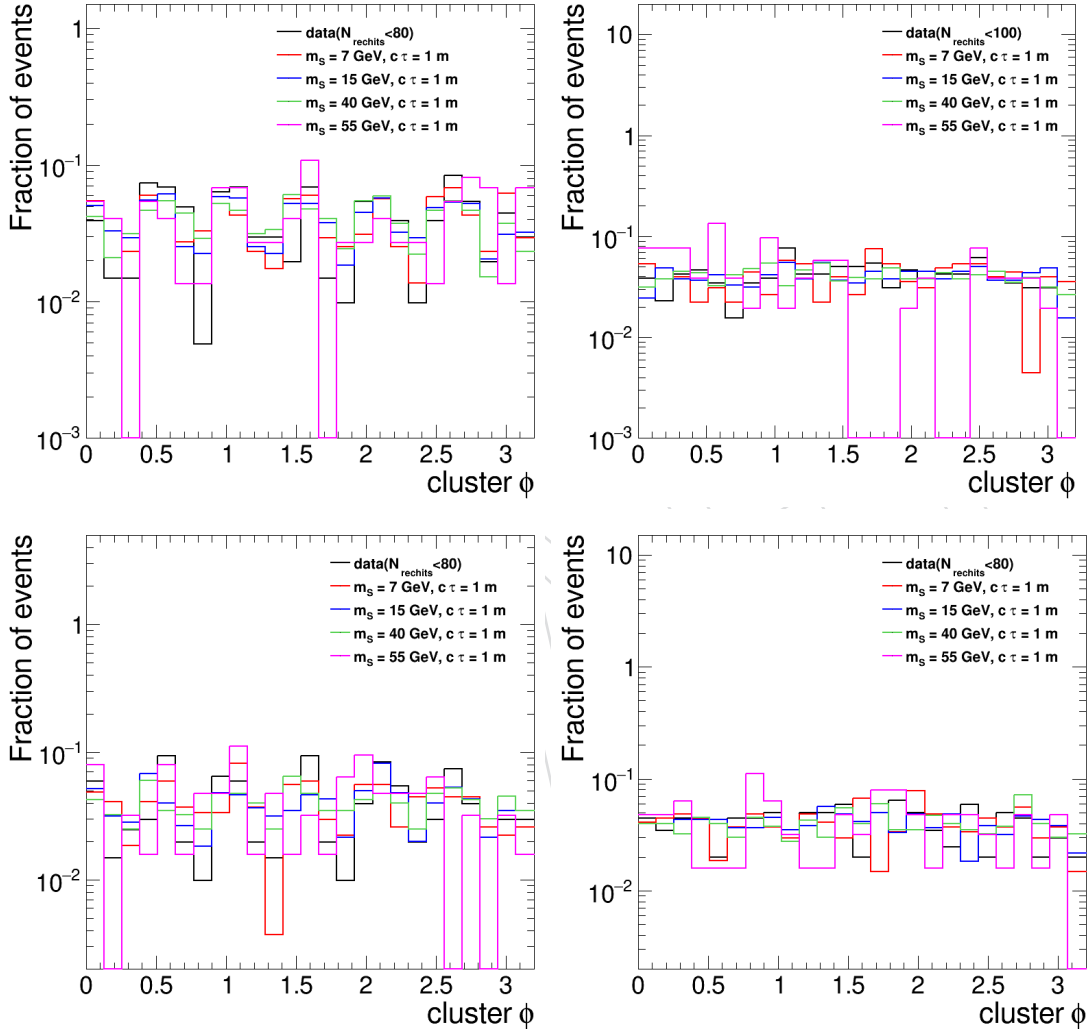


Figure 58: The cluster ϕ distributions are shown. The ϕ of both clusters are shown for DT-DT (top left) and CSC-CSC (top right) category. The cluster ϕ for DT (bottom left) and CSC (bottom right) clusters are shown in separate plots for DT-CSC category.

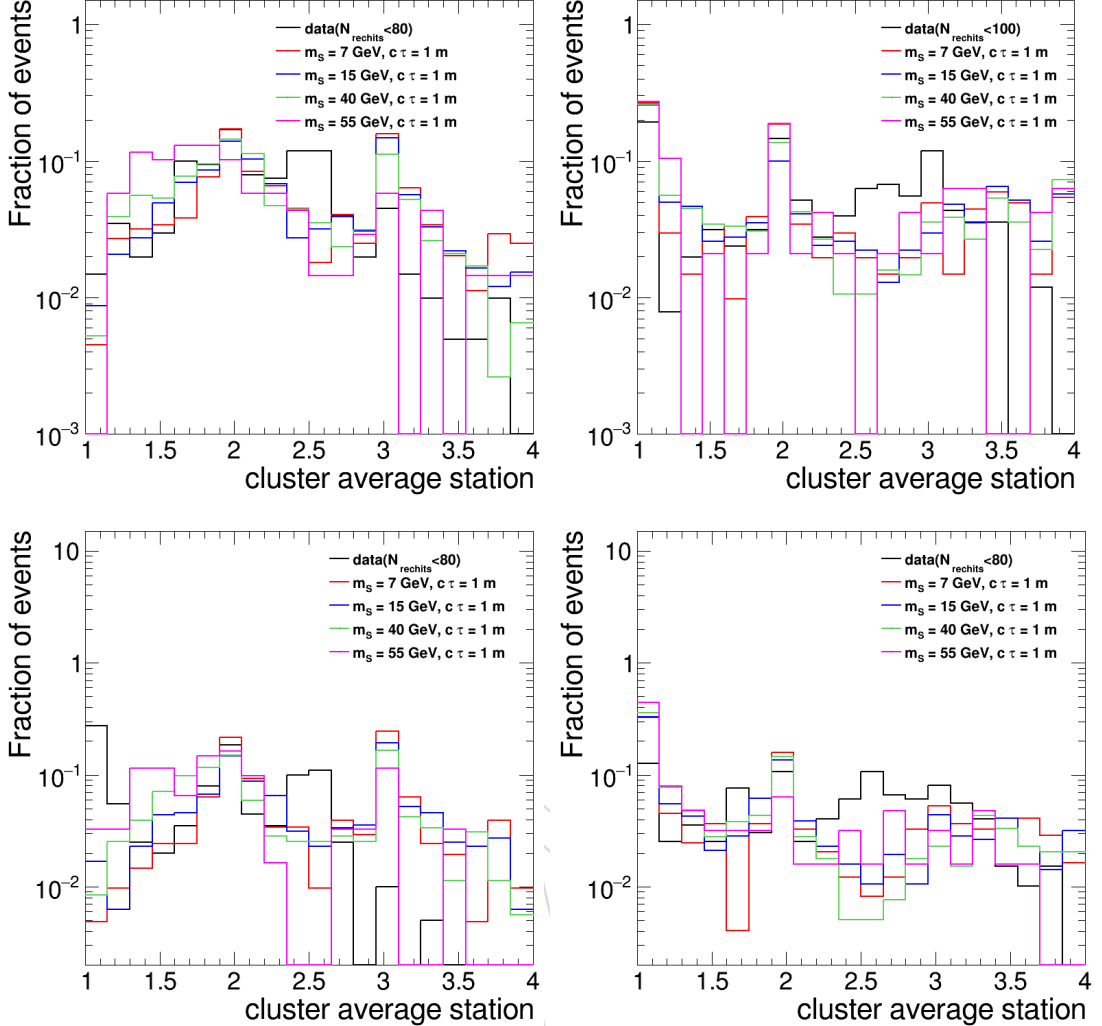


Figure 59: The cluster average station distributions are shown. The average station of both clusters are shown for DT-DT (top left) and CSC-CSC (top right) category. The cluster average station for DT (bottom left) and CSC (bottom right) clusters are shown in separate plots for DT-CSC category.

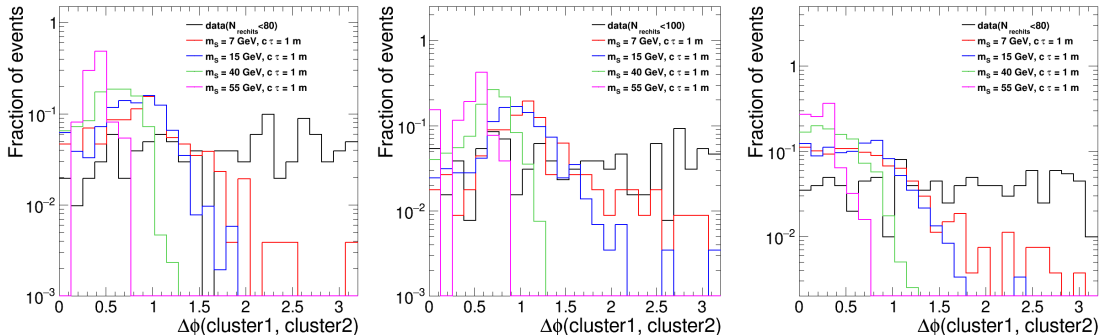


Figure 60: The $\Delta\phi(\text{cluster1}, \text{cluster2})$ distributions are shown for DT-DT (left), CSC-CSC (middle), and DT-CSC (right) category.

1056 C Issues in Run2 Data Taking

1057 C.1 L1 EE Pre-firing

1058 In 2016 and 2017, the ECAL endcap was pre-firing at L1, resulting in inefficiencies in the data
 1059 taking. As a result, we follow the recommended procedure to check if this analysis is af-
 1060 fected by the pre-firing issue. Following the recommended procedure to check in the EXO Pre-
 1061 Approval checklist[43], we check in MC signal samples (2016 and 2017 condition) the change
 1062 in shape and cut efficiency of $N_{rechits}$ and $\Delta\phi$ (cluster, MET) by removing events with jets with
 1063 $p_T > 100$ GeV and $2.25 < |\eta| < 3.0$. As the analysis uses mostly the CSC system, we do not
 1064 expect and do not observe any significant change from this issue.

1065 The change in signal efficiency of $N_{rechits}$ cuts on both clusters is shown in Table. 61 for various
 1066 LLP masses with 1m lifetime decaying to dd. We observe that the change in signal efficiency is
 1067 at most 1% for all signal points. Furthermore, we observed no significant changes in shape for
 1068 both variables. The shape of $N_{rechits}$ for signal samples for various LLP masses with 1m lifetime
 1069 are shown in Fig. 61, Fig. 62, Fig. 64, and Fig. 63 for each category.

1070 Since the change in signal efficiency is at most 1%, no additional corrections are needed to
 1071 mitigate the issue.

Table 61: Change in $N_{rechits}$ cut Efficiency

	7 GeV	15 GeV	40 GeV	55 GeV
DT-DT	0.8%	0.8%	0.3%	0.2%
CSC-CSC	-1.4%	1.0%	-0.1%	1.4%
DT-CSC	1.3%	-0.1%	-0.7%	0.1%

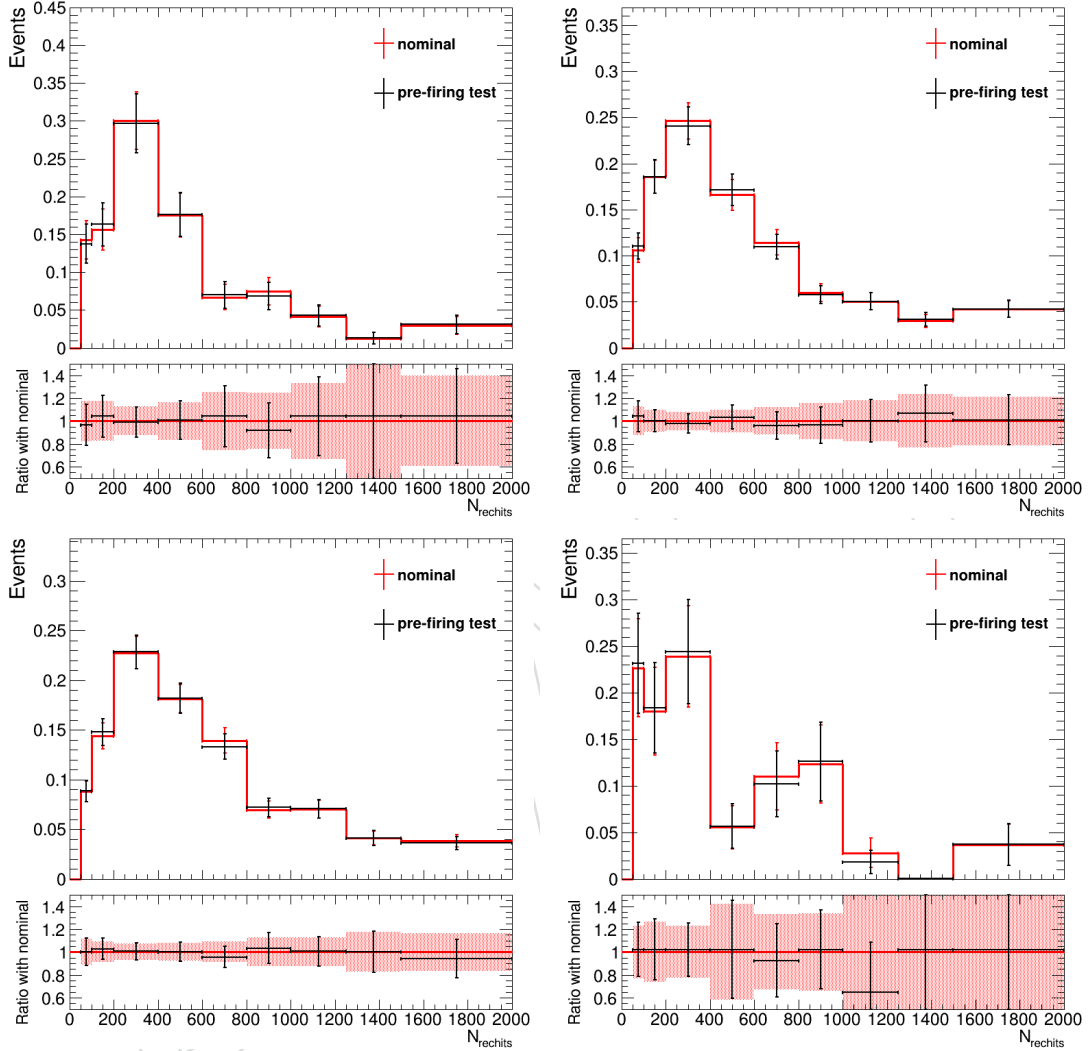


Figure 61: The normalized maximum N_{rechits} distributions for MC signal samples in CSC-CSC category with LLP lifetime of 1m and LLP mass of 7 GeV (Top Left), 15 GeV (Top Right), 40 GeV (Bottom Left), 55 GeV (Bottom Right) is shown. The shape with nominal selection and with event removal that have jets in the problematic region is shown. No significant change is observed between the two shapes.

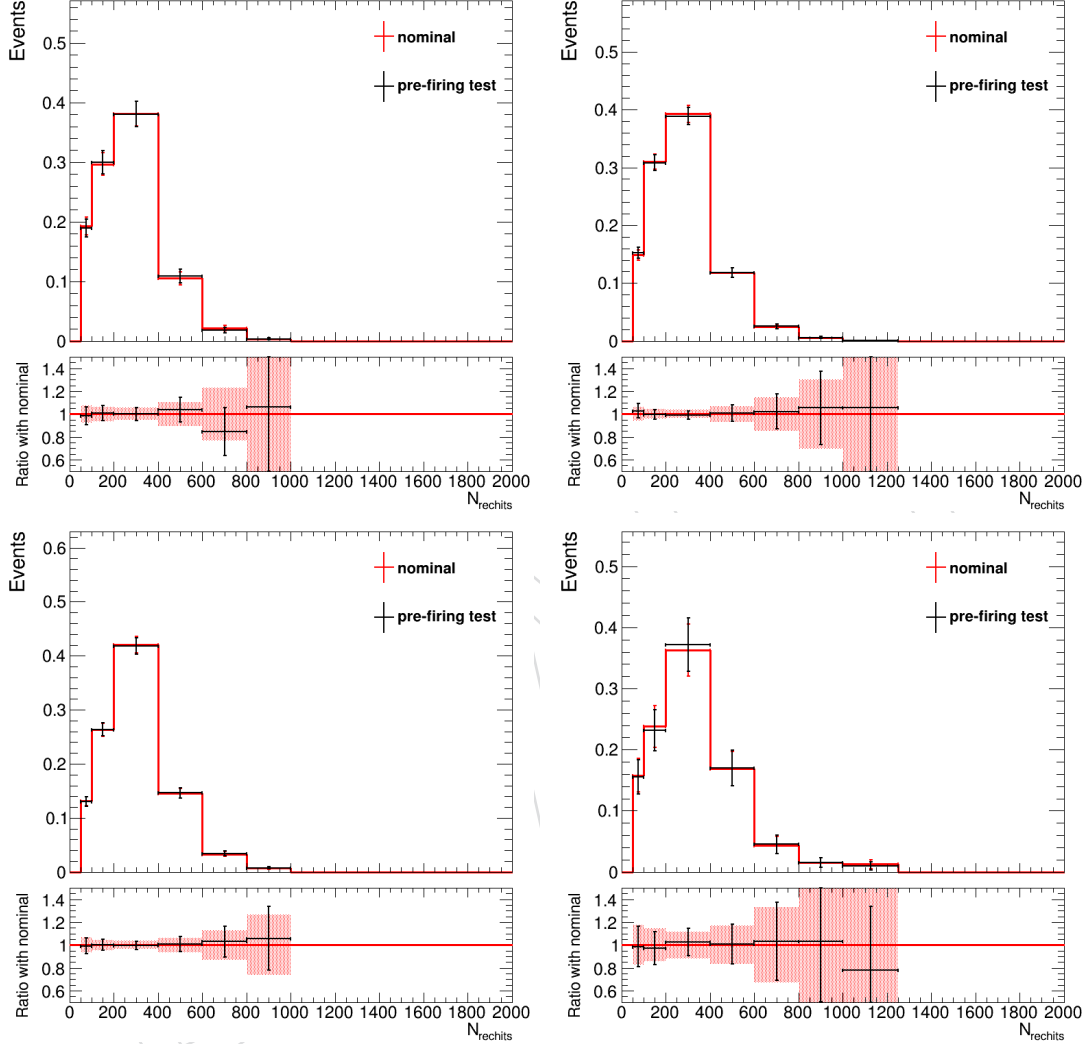


Figure 62: The normalized maximum N_{rechits} distributions for MC signal samples in DT-DT category with LLP lifetime of 1m and LLP mass of 7 GeV (Top Left), 15 GeV (Top Right), 40 GeV (Bottom Left), 55 GeV (Bottom Right) is shown. The shape with nominal selection and with event removal that have jets in the problematic region is shown. No significant change is observed between the two shapes.

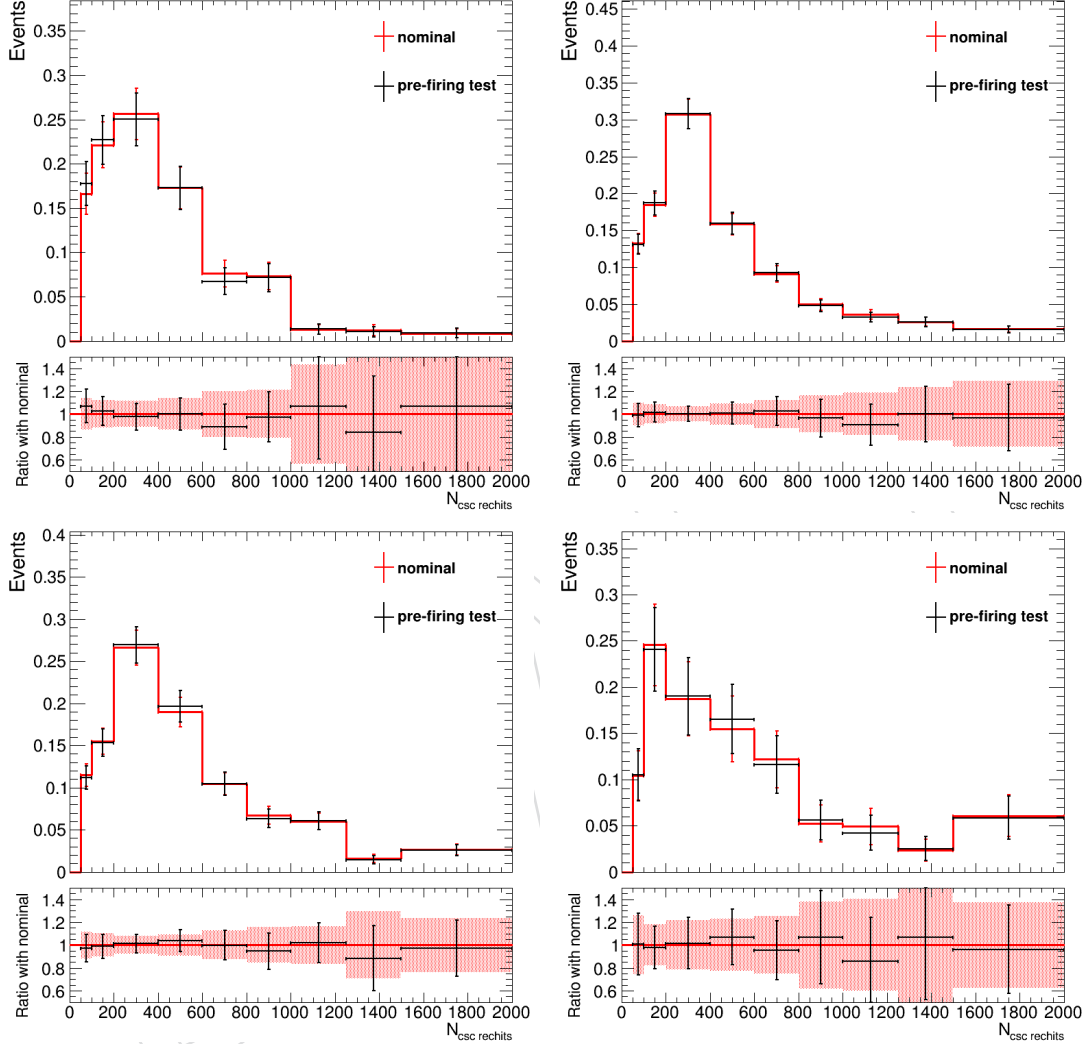


Figure 63: The normalized N_{cscchits} distributions for MC signal samples in DT-CSC category with LLP lifetime of 1m and LLP mass of 7 GeV (Top Left), 15 GeV (Top Right), 40 GeV (Bottom Left), 55 GeV (Bottom Right) is shown. The shape with nominal selection and with event removal that have jets in the problematic region is shown. No significant change is observed between the two shapes.

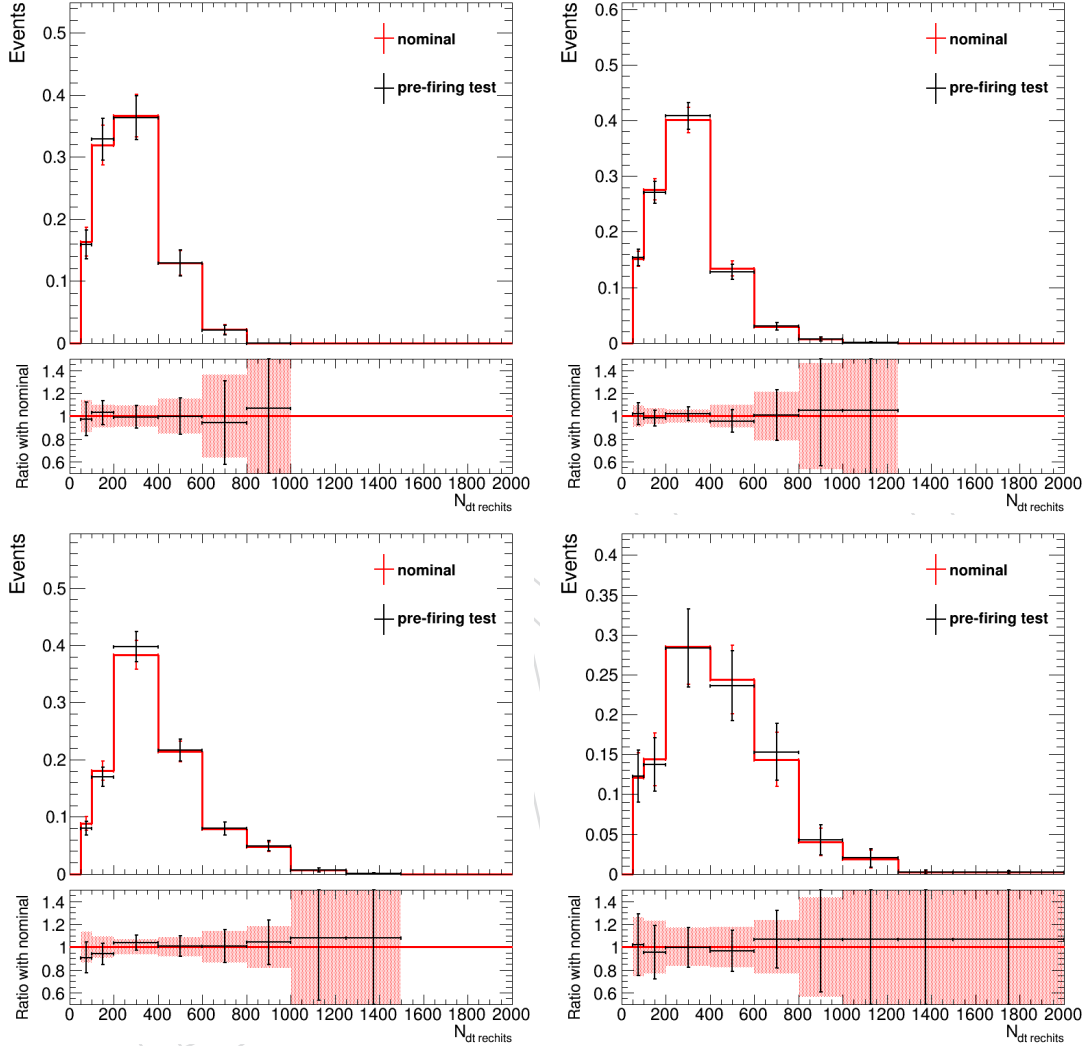


Figure 64: The normalized $N_{dt\text{rec}}^{\text{hits}}$ distributions for MC signal samples in DT-CSC category with LLP lifetime of 1m and LLP mass of 7 GeV (Top Left), 15 GeV (Top Right), 40 GeV (Bottom Left), 55 GeV (Bottom Right) is shown. The shape with nominal selection and with event removal that have jets in the problematic region is shown. No significant change is observed between the two shapes.

C.2 HEM15/16 Failure

Starting from run 3109077 (toward the end of 2018B) until the end of 2018 run, two modules of the ECAL endcap, HEM15 and HEM16 were effectively off, due to power interruptions. The affected region is $-3.0 < \eta < -1.3$ and $-1.57 < \phi < -0.87$. To estimate the impact of this issue on the signal yield prediction, we remove all jets that fall in the problematic region, and recompute the predicted signal yield in the signal region using signal simulations in 2018 condition. The variation in the signal prediction is 3-6% for all signal models, thus the impact on the total signal yield is 1-2%, given the luminosity ratio of the problematic period and the entire Run2 period.

DRAFT

1081 D Study of overlap between double cluster categories and single 1082 cluster categories

1083 D.1 Overlap between Double Cluster and Single Cluster CSC category

1084 We check whether the signal and data events in the ABCD plane of the single CSC cluster
 1085 category satisfies the double cluster requirements.

1086 In data, no events satisfy the double cluster requirement. The percentage of signal events in
 1087 the ABCD plane of CSC analysis is summarized in Table. 62. The largest overlap is observed
 1088 in signals with lifetimes of about 1 meter, corresponding to the lifetimes that the double cluster
 1089 category is most sensitive to. For most signal points the overlap is only a few percent, but for
 1090 lifetimes of 1 meter, the overlap is about 20%.

1091 The observed limit for 4b decay mode computed with asymptotic approximation with and
 1092 without the overlapping events removed is shown in Fig. 65. As expected from the percentage
 1093 of overlapping signal events, the limit at around 1 meter is most affected and the largest impact
 1094 is about 25%.

1095 In the case of overlap, we events are categorized into the double cluster category with priority
 1096 over the single cluster categories because the double cluster category has more favorable signal
 1097 to background ratio, and more favorable sensitivity.

Table 62: Percentage of signal events in ABCD plane of single cluster CSC analysis that also satisfy the double cluster signal region selections.

signal sample	CSC-CSC	DT-DT	DT-CSC	Total
15 GeV, $c\tau$ 100 mm	1.79%	0.0%	0.64%	2.43%
15 GeV, $c\tau$ 1000 mm	5.82%	0.0%	9.69%	15.52%
15 GeV, $c\tau$ 10000 mm	0.4%	0.0%	1.57%	1.97%
15 GeV, $c\tau$ 100000 mm	0.0%	0.0%	0.2%	0.2%
40 GeV, $c\tau$ 100 mm	2.2%	0.0%	0.0%	2.2%
40 GeV, $c\tau$ 1000 mm	10.91%	0.0%	8.47%	19.38%
40 GeV, $c\tau$ 10000 mm	2.49%	0.0%	3.11%	5.6%
40 GeV, $c\tau$ 100000 mm	0.24%	0.0%	0.28%	0.52%
55 GeV, $c\tau$ 1000 mm	1.77%	0.0%	2.02%	3.78%
55 GeV, $c\tau$ 10000 mm	0.55%	0.0%	1.49%	2.04%
55 GeV, $c\tau$ 100000 mm	0.0%	0.0%	0.42%	0.42%

1098 D.2 Overlap between Double Cluster and Single Cluster DT category

1099 We check for overlap between the double cluster categories and the single DT cluster category
 1100 for signal events. The percentage of signal events in the ABCD plane of DT analysis is sum-
 1101 marized in Table. 63. Similar to the overlap with the single cluster CSC category, the largest
 1102 overlap with single cluster DT category is observed in signals with lifetimes of about 1 meter,
 1103 corresponding to the lifetimes that the double cluster category is most sensitive to. For most
 1104 signal points the overlap is only a few percent, but for lifetimes of 1 meter, the overlap is about
 1105 20%.

1106 In the case of overlap, we events are categorized into the double cluster category with priority
 1107 over the single cluster categories because the double cluster category has more favorable signal
 1108 to background ratio, and more favorable sensitivity.

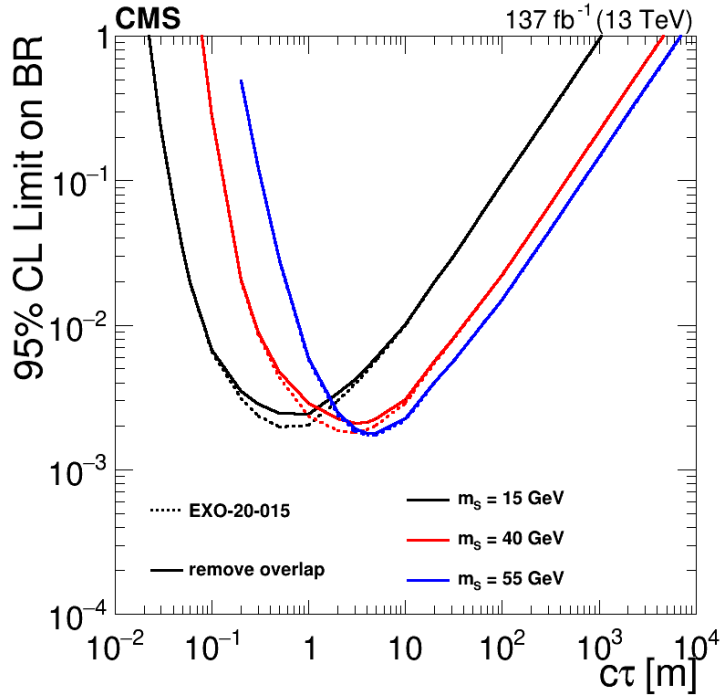


Figure 65: The observed limit for 4b decay mode computed with asymptotic approximation with and without the overlapping events removed is shown.

Table 63: Percentage of signal events in ABCD plane of single cluster DT analysis that also satisfy the double cluster signal region selections.

signal sample	CSC-CSC	DT-DT	DT-CSC	Total
15 GeV, $c\tau$ 100 mm	0.0%	0.0%	0.26%	0.26%
15 GeV, $c\tau$ 1000 mm	0.0%	4.23%	5.37%	9.6%
15 GeV, $c\tau$ 10000 mm	0.0%	0.38%	0.64%	1.02%
15 GeV, $c\tau$ 100000 mm	0.0%	0.0%	0.13%	0.13%
40 GeV, $c\tau$ 100 mm	0.0%	0.0%	0.0%	0.0%
40 GeV, $c\tau$ 1000 mm	0.0%	4.68%	7.06%	11.74%
40 GeV, $c\tau$ 10000 mm	0.0%	1.54%	1.66%	3.21%
40 GeV, $c\tau$ 100000 mm	0.0%	0.08%	0.13%	0.21%
55 GeV, $c\tau$ 100 mm	nan%	nan%	nan%	nan%
55 GeV, $c\tau$ 1000 mm	0.0%	0.41%	3.83%	4.25%
55 GeV, $c\tau$ 10000 mm	0.0%	0.43%	1.12%	1.54%
55 GeV, $c\tau$ 100000 mm	0.0%	0.04%	0.36%	0.4%

1109 E Signal contamination for the two cluster categories

1110 We have also checked the level of signal contamination in the background-enriched bins B,
 1111 C, and D for DT-CSC category and bin B and C for DT-DT and CSC-CSC categories. The ex-
 1112 pected number of signal events (including all production modes) in bin B, C, and D, assuming
 1113 $\text{BR}(\text{H} \rightarrow \text{ss}) = 1\%$ for several LLP masses and proper lifetime $c\tau$ for each category are shown in
 1114 Table. 64, Table. 65, and Table. 66. The signal contamination is small in most lifetimes, com-
 1115 pared to the expected number of predicted background events (See Table. 22). The largest
 1116 contamination comes from $c\tau$ around 1 meter, but at those lifetimes, we expect to set limit at
 1117 around 0.1%, so if we assume $\text{BR}(\text{H} \rightarrow \text{ss}) = 0.1\%$ for those $c\tau$ points the signal contamination is
 1118 small compared to the predicted background.

Table 64: Signal contamination in the signal region in binB and binC in CSC-CSC category including all production modes, for bb decay mode, assuming $\text{BR}(\text{H} \rightarrow \text{ss}) = 1\%$.

binB				
LLP mass $c\tau$	0.1 m	1 m	10 m	100 m
15 GeV	0.3	1.0	0.1	0.0
40 GeV	0.0	1.6	0.4	0.0
55 GeV	0.0	0.3	0.2	0.0

binC				
LLP mass $c\tau$	0.1 m	1 m	10 m	100 m
15 GeV	0.0	0.1	0.0	0.0
40 GeV	0.0	0.1	0.0	0.0
55 GeV	0.0	0.0	0.0	0.0

Table 65: Signal contamination in the signal region in binB and binC in DT-DT category including all production modes, for bb decay mode, assuming $\text{BR}(\text{H} \rightarrow \text{ss}) = 1\%$.

binB				
LLP mass $c\tau$	0.1 m	1 m	10 m	100 m
15 GeV	0.1	3.5	0.1	0.0
40 GeV	0.0	2.2	0.9	0.0
55 GeV	0.0	0.3	0.6	0.0

binC				
LLP mass $c\tau$	0.1 m	1 m	10 m	100 m
15 GeV	0.0	0.2	0.0	0.0
40 GeV	0.0	0.1	0.1	0.0
55 GeV	0.0	0.0	0.1	0.0

Table 66: Signal contamination in the signal region in bin B, C, and D in DT-CSC category including all production modes, for bb decay mode, assuming $\text{BR}(H \rightarrow ss) = 1\%$.

		binB			
LLP mass	$c\tau$	0.1 m	1 m	10 m	100 m
15 GeV		0.1	1.0	0.0	0.0
40 GeV		0.0	0.6	0.2	0.0
55 GeV		0.0	0.1	0.2	0.0

		binC			
LLP mass	$c\tau$	0.1 m	1 m	10 m	100 m
15 GeV		0.0	0.2	0.0	0.0
40 GeV		0.0	0.1	0.1	0.0
55 GeV		0.0	0.0	0.0	0.0

		binD			
LLP mass	$c\tau$	0.1 m	1 m	10 m	100 m
15 GeV		0.1	1.5	0.1	0.0
40 GeV		0.0	1.2	0.4	0.0
55 GeV		0.0	0.4	0.5	0.1

1119 F Studies on extending the sensitivity to low mass regions

1120 The previous analysis (AN-19-154) showed good sensitivity over a mass range from 50 GeV
 1121 down to 7 GeV, showing no mass dependence on the limit. The question arises if a wider range
 1122 of masses can be studied, especially masses below 1 GeV. The decrease in the LLP mass shifts
 1123 the peak sensitivity to a lower $c\tau$ value, as a lower mass results in a more boosted final state,
 1124 which in turn leads to a longer travel distance of the LLP. This is compensated by a smaller
 1125 decay length of the particle. While for the current mass range the LLP decays predominately
 1126 into a b-quark pair, new decay channel start to open up for lower masses. The plot in Figure 66
 1127 shows the different decay channels depending on the LLP mass. Due to a technical limitation
 1128 in the MC production, the lowest LLP mass that can be produced at the moment is 0.4 GeV. Due
 1129 to this limitation the detector response between 0.4 GeV and 4 GeV is checked, to show a mass
 1130 independence of the results. Afterwards the results of the smallest masses can be extrapolated
 1131 to even lower masses, in case for the $\gamma\gamma$ down to the keV scale.

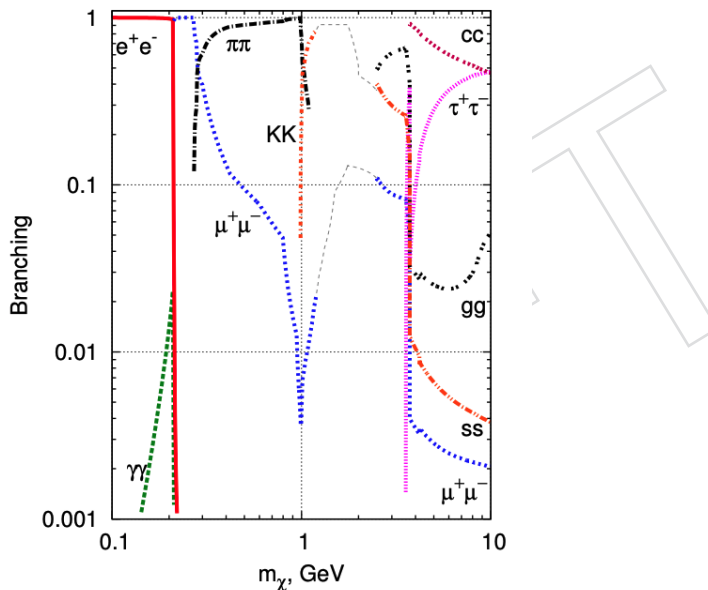


Figure 66: Branching ratio of scalar LLPs

1132 F.1 Detector response study

1133 In this section the detector response is checked for different masses and decay modes. The
 1134 masses and lifetimes of the samples used for each decay channels are shown in Table 67 and
 1135 68. For this study only the ggH production mode is used. To fairly compare the different
 1136 masses, the $c\tau$ of the samples is adjusted in such a way, that the distribution of the LLP decay
 1137 position is the same for all masses. In Fig. 67 the gen-level decay z position for the ee samples
 1138 is shown. The plot shows two groups of samples with the same decay position distribution,
 1139 one with each of the higher $c\tau$ values per mass point, the other with the lower $c\tau$ mass point.
 1140 For the following studies all the analysis cuts have been applied, except for the MET cut and
 1141 the trigger requirement. This is done to increase the statistics in the plots. All the plots in this
 1142 study were also performed with the MET cut applied (see figure 79 to 88) where no significant
 1143 difference was found. In Figure 68 the signal efficiency is shown as a function of the LLP decay
 1144 z position for the ee sample. The plot shows, that decays inside the chambers ME1/2-3, ME2
 1145 and ME4 result in a signal efficiency of close to 0. This can be explained by the difference in the
 1146 decay channel compared to the bb channel: For the ee, $\gamma\gamma$ and $\pi^+\pi^-$ the shower produced in

Table 67: Masses and lifetimes for the ee, $\gamma\gamma$ and $\pi\pi$ decay channels

signal sample
0.4 GeV, $c\tau$ 10 mm
0.4 GeV, $c\tau$ 50 mm
1.0 GeV, $c\tau$ 25 mm
1.0 GeV, $c\tau$ 125 mm
2.0 GeV, $c\tau$ 50 mm
2.0 GeV, $c\tau$ 250 mm
4.0 GeV, $c\tau$ 100 mm
4.0 GeV, $c\tau$ 500 mm

Table 68: Masses and lifetimes for the gg, dd, and KK decay channels

signal sample
3.0 GeV, $c\tau$ 100 mm
3.0 GeV, $c\tau$ 500 mm

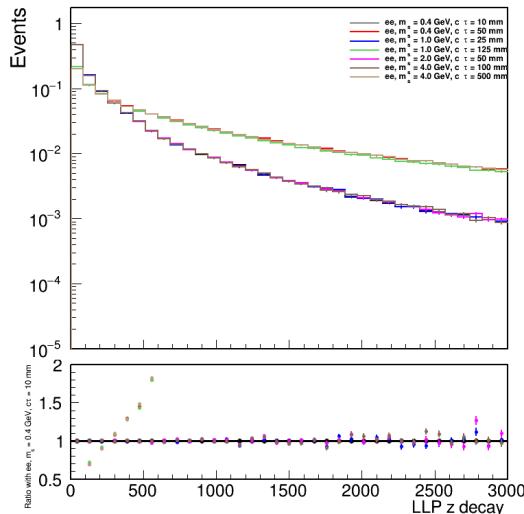


Figure 67: The decay position in z of different signal samples in ee decay mode.

the muon chambers is a electromagnetic shower, while the bb, dd, gg and KK produce hadronic showers. In general hadronic showers need more material to be stopped, while EM showers are not able to penetrate the steel between the chambers, except for ME1/1 and ME3 where the thickness of the steel is lower.

To study the detector response the ABCD variables and the ClusterID variables are compared. We show the distribution of the clusterID variables (cluster η , average station, and number of stations) for all decay modes in Figure 69 to 73. The distribution of the $N_{rechits}$ and $\Delta\phi(\text{cluster}, \text{MET})$ for all decay modes are shown in Figure 74 to 78. The plots show good agreement between the different masses, which leads to the conclusion that the detector response is mass independent. With this result it is possible to extrapolate limits to lower masses than what can be produced in MC.

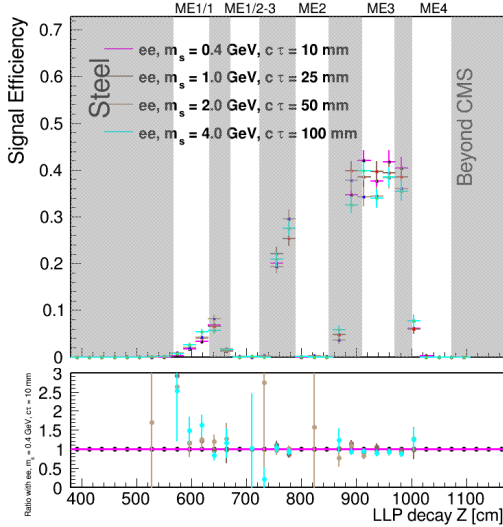


Figure 68: Signal efficiency with respect to the LLP decay position in z for ee channel

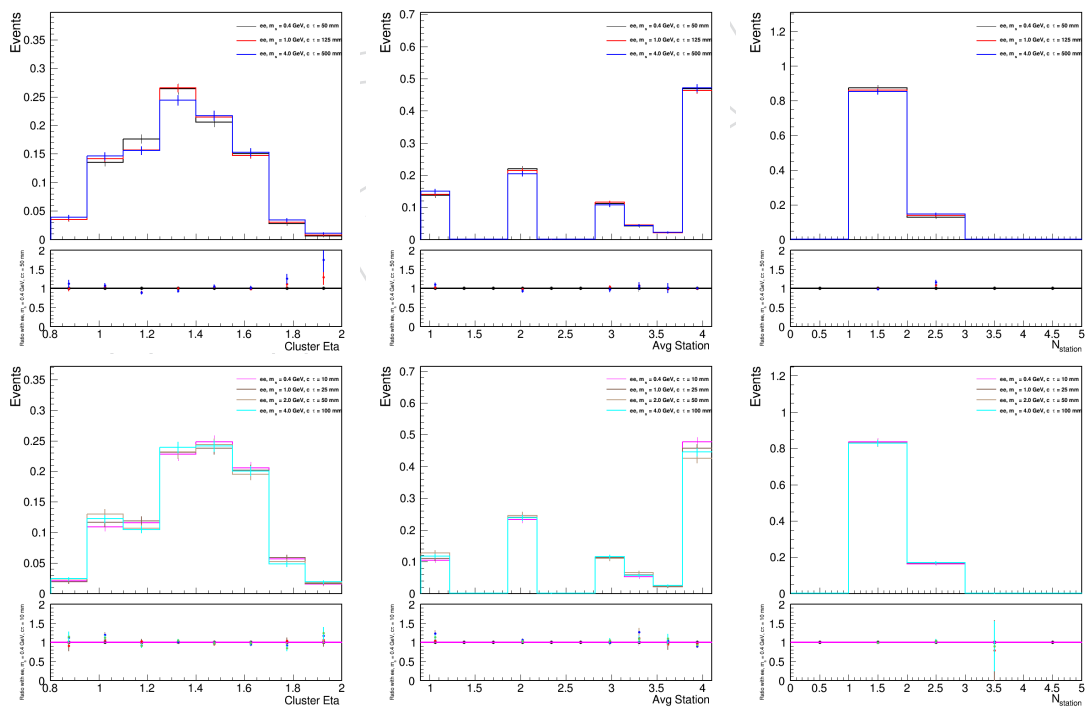


Figure 69: The cluster η (left), average station (center), and number of station (right) distributions are shown for long lifetime (top) and short lifetime (bottom) ee decay mode.

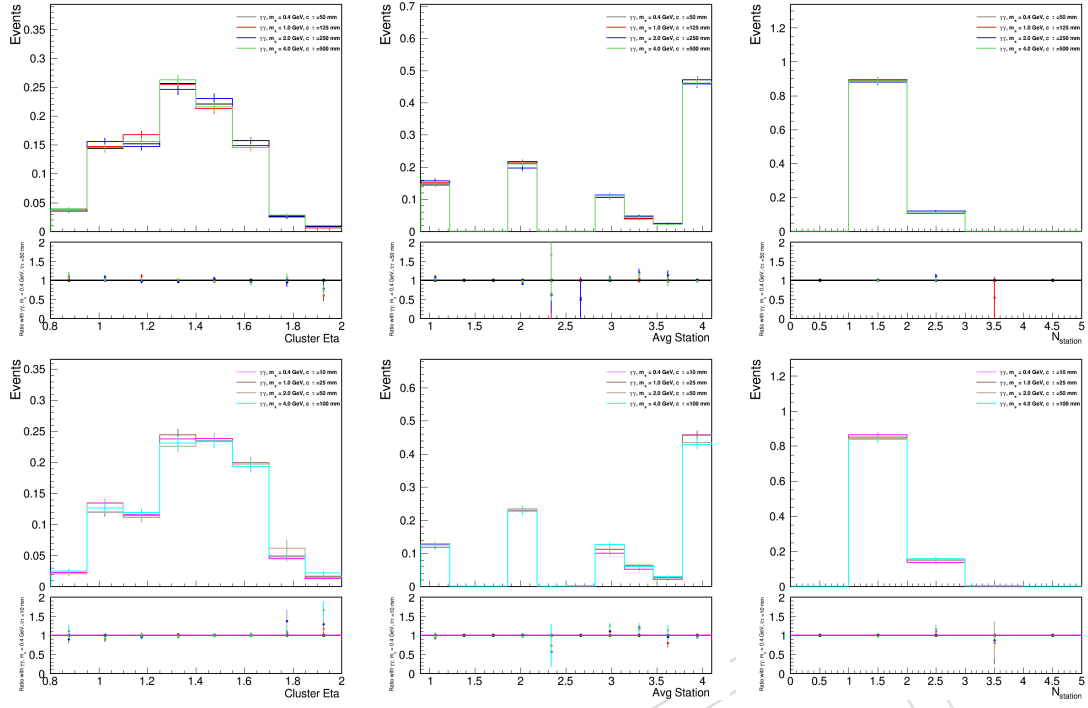


Figure 70: The cluster η (left), average station (center), and number of station (right) distributions are shown for long lifetime (top) and short lifetime (bottom) $\gamma\gamma$ channel

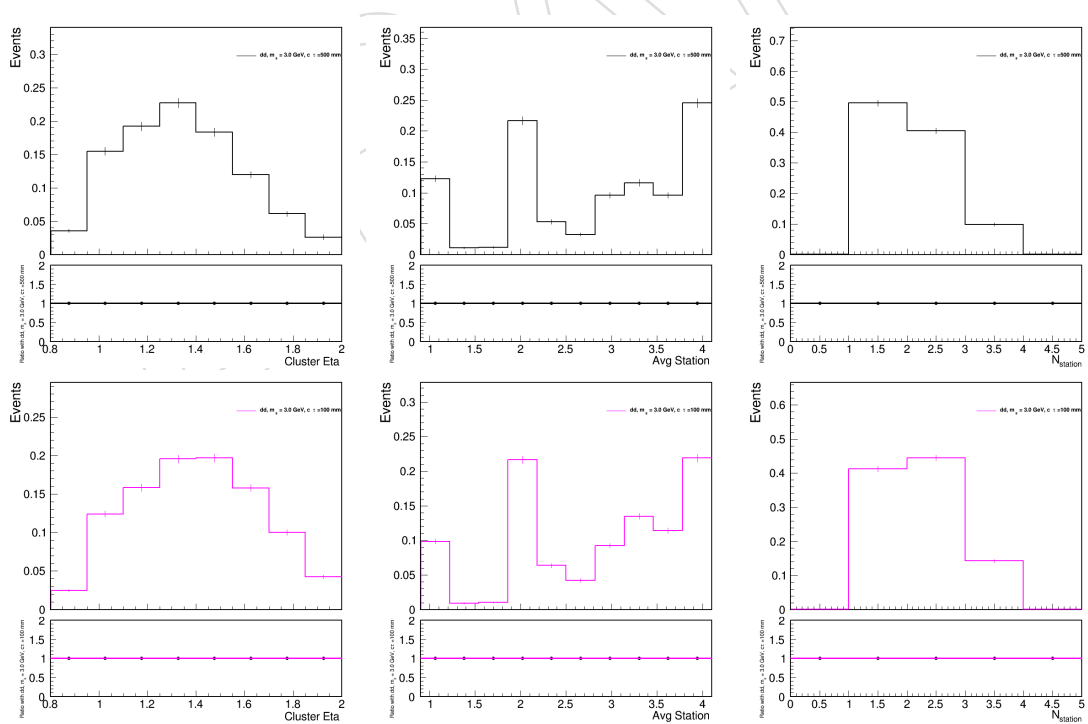


Figure 71: The cluster η (left), average station (center), and number of station (right) distributions are shown for long lifetime (top) and short lifetime (bottom) dd channel

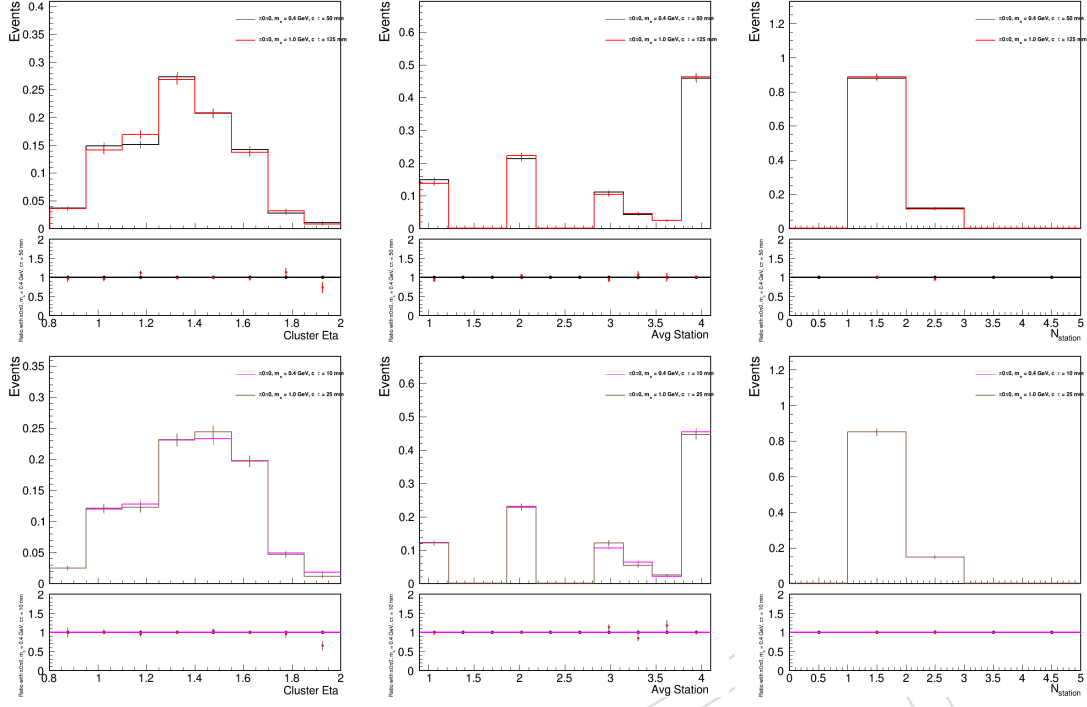


Figure 72: The cluster η (left), average station (center), and number of station (right) distributions are shown for long lifetime (top) and short lifetime (bottom) $\pi^0\pi^0$ channel

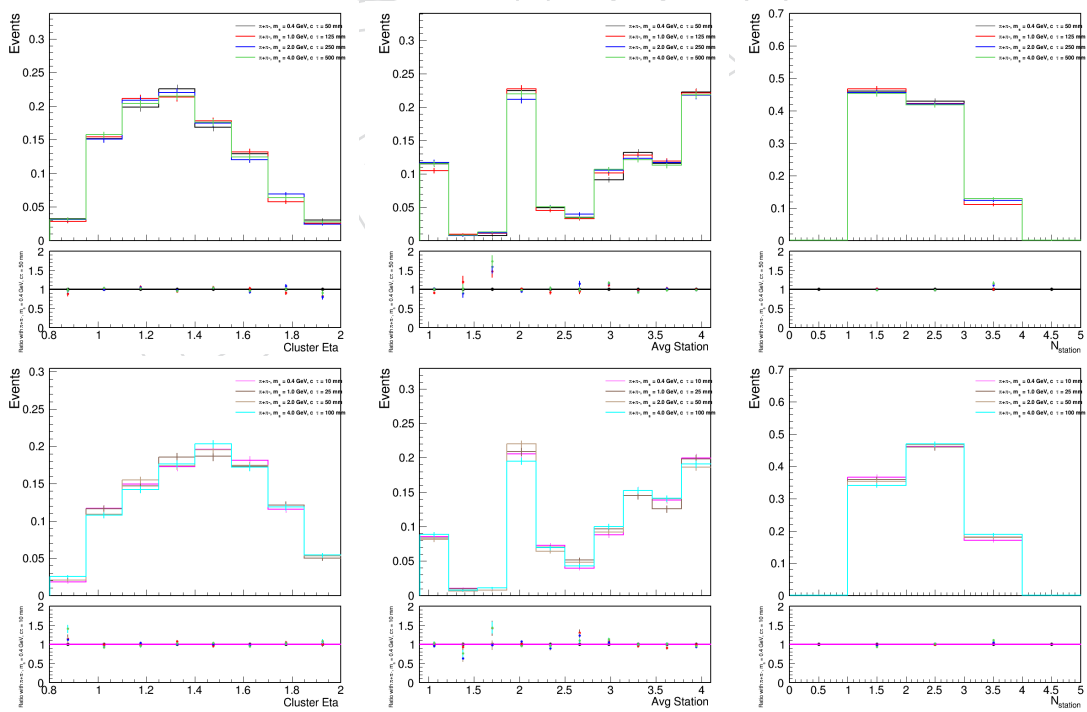


Figure 73: The cluster η (left), average station (center), and number of station (right) distributions are shown for long lifetime (top) and short lifetime (bottom) $\pi^+\pi^-$ channel

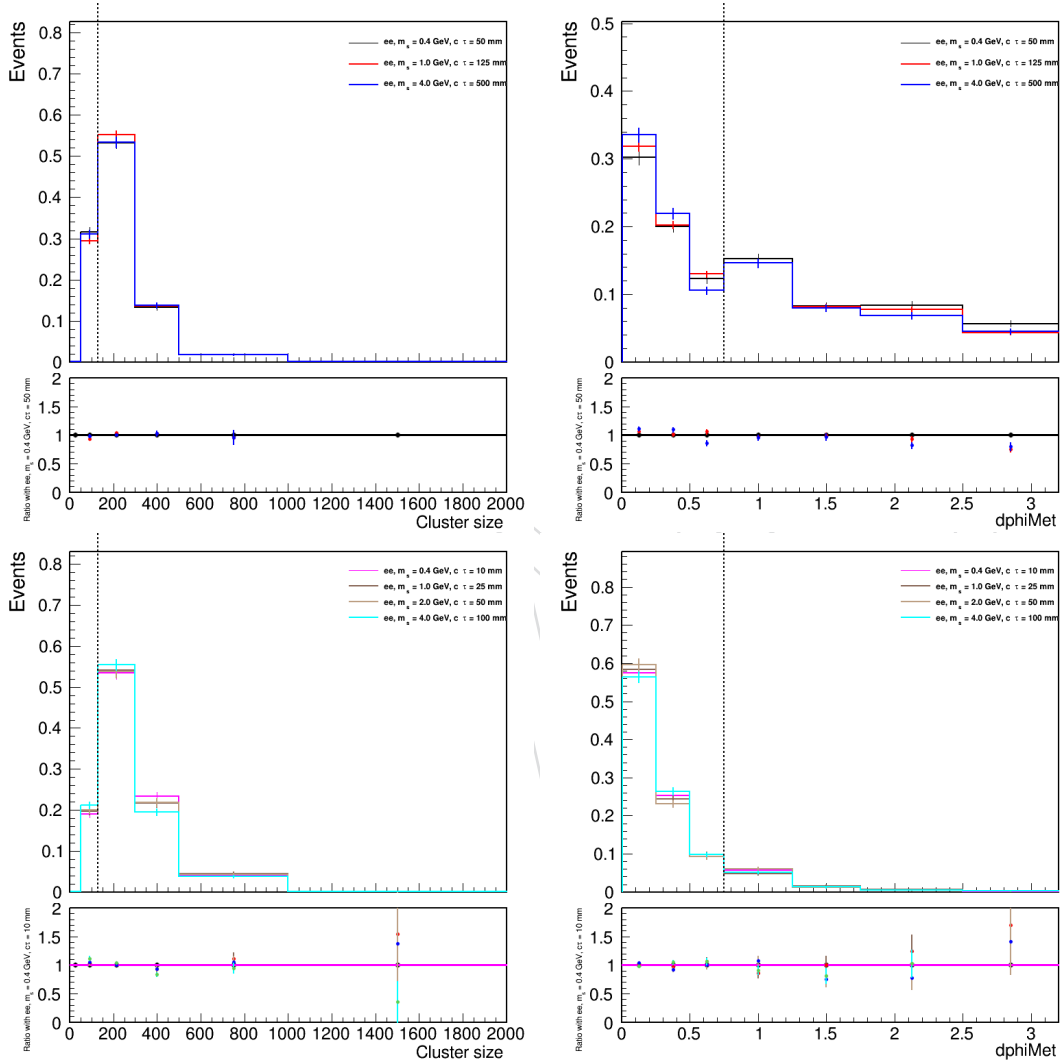


Figure 74: The distributions of the N_{rechits} (left) and $\Delta\phi(\text{cluster}, \text{MET})$ (right) for long lifetime (top) and short lifetime (bottom) ee channel.

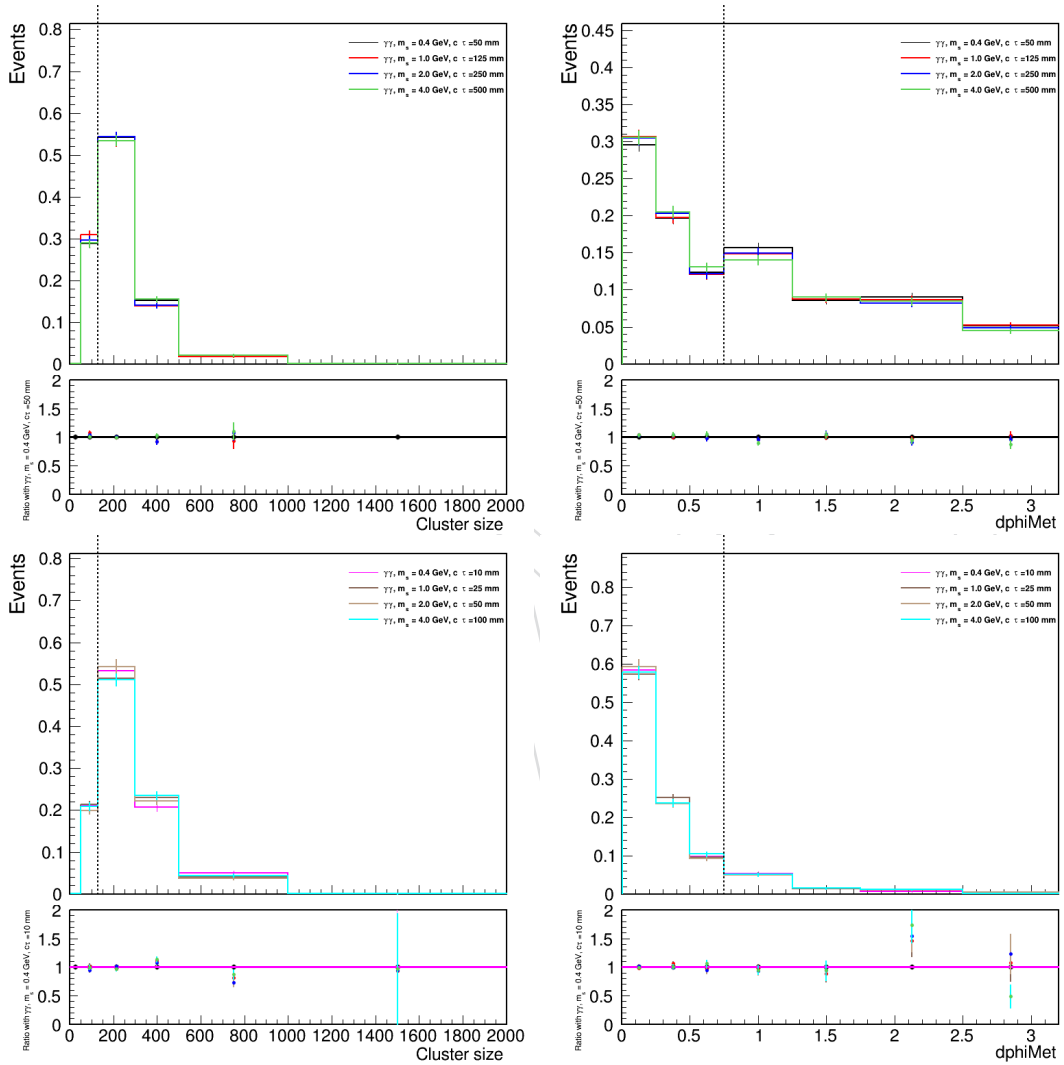


Figure 75: The distributions of the $N_{rechits}$ (left) and $\Delta\phi(\text{cluster}, \text{MET})$ (right) for long lifetime (top) and short lifetime (bottom) $\gamma\gamma$ channel

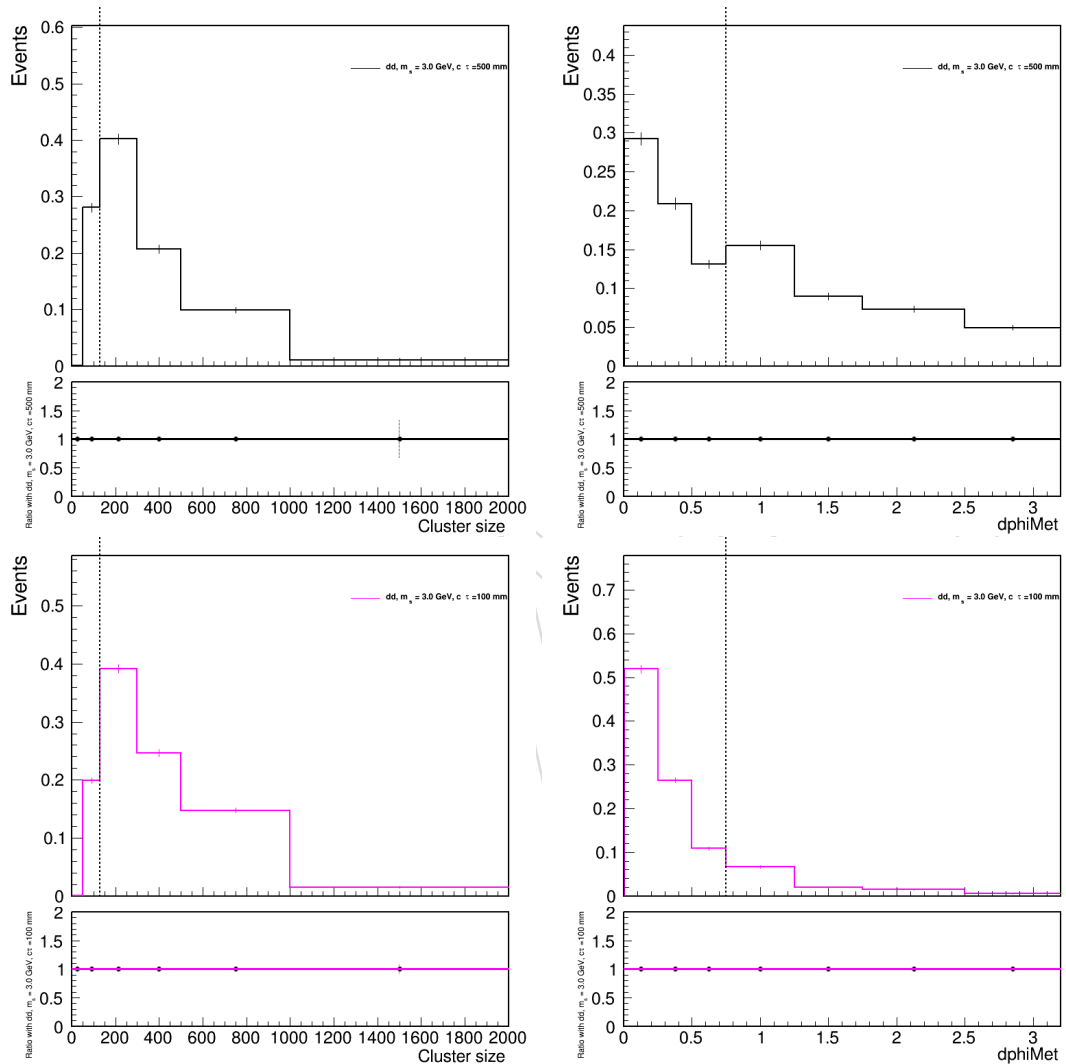


Figure 76: The distributions of the N_{rechits} (left) and $\Delta\phi(\text{cluster}, \text{MET})$ (right) for long lifetime (top) and short lifetime (bottom) dd channel

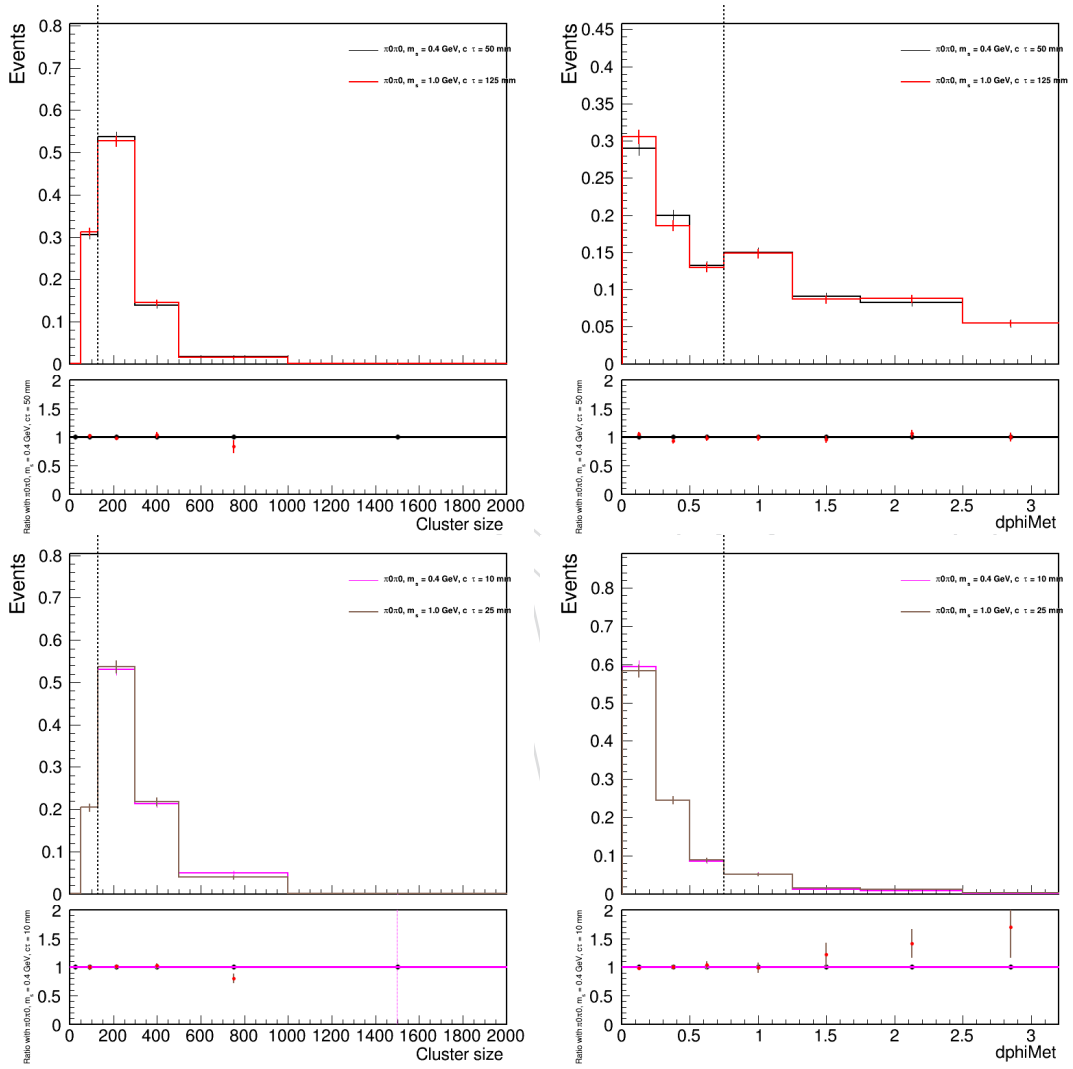


Figure 77: The distributions of the N_{rechits} (left) and $\Delta\phi(\text{cluster}, \text{MET})$ (right) for long lifetime (top) and short lifetime (bottom) $\pi^0\pi^0$ channel

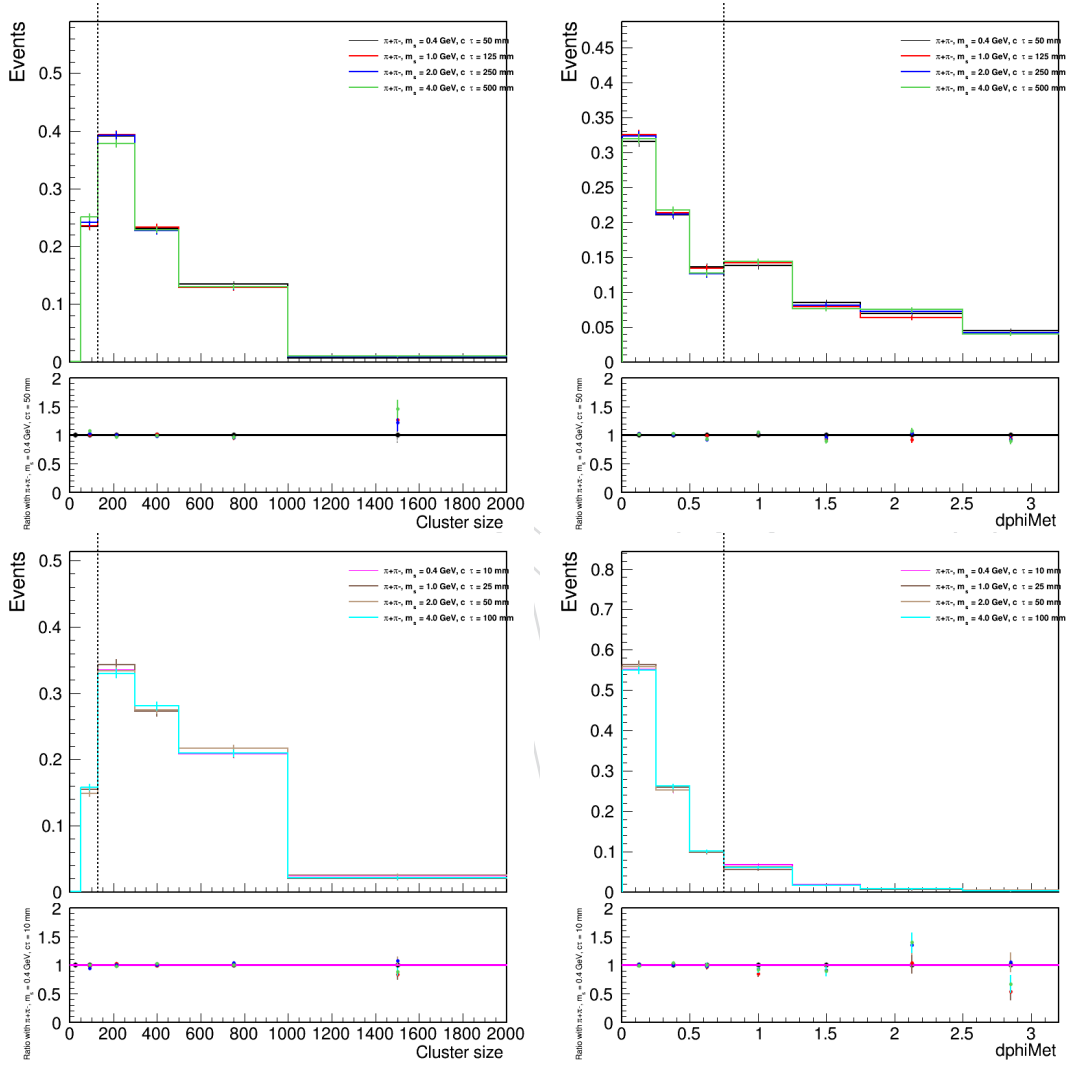


Figure 78: The distributions of the N_{rechits} (left) and $\Delta\phi(\text{cluster}, \text{MET})$ (right) for long lifetime (top) and short lifetime (bottom) $\pi^+\pi^-$ channel

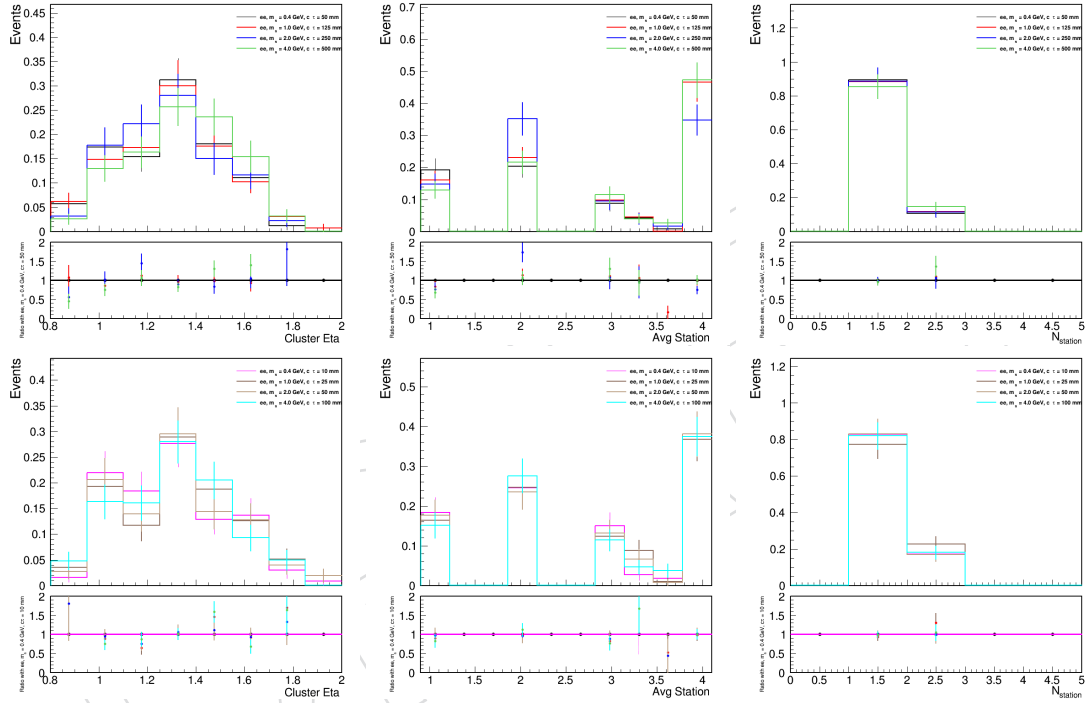


Figure 79: The cluster η (left), average station (center), and number of station (right) distributions are shown for long lifetime (top) and short lifetime (bottom) ee channel with MET cut

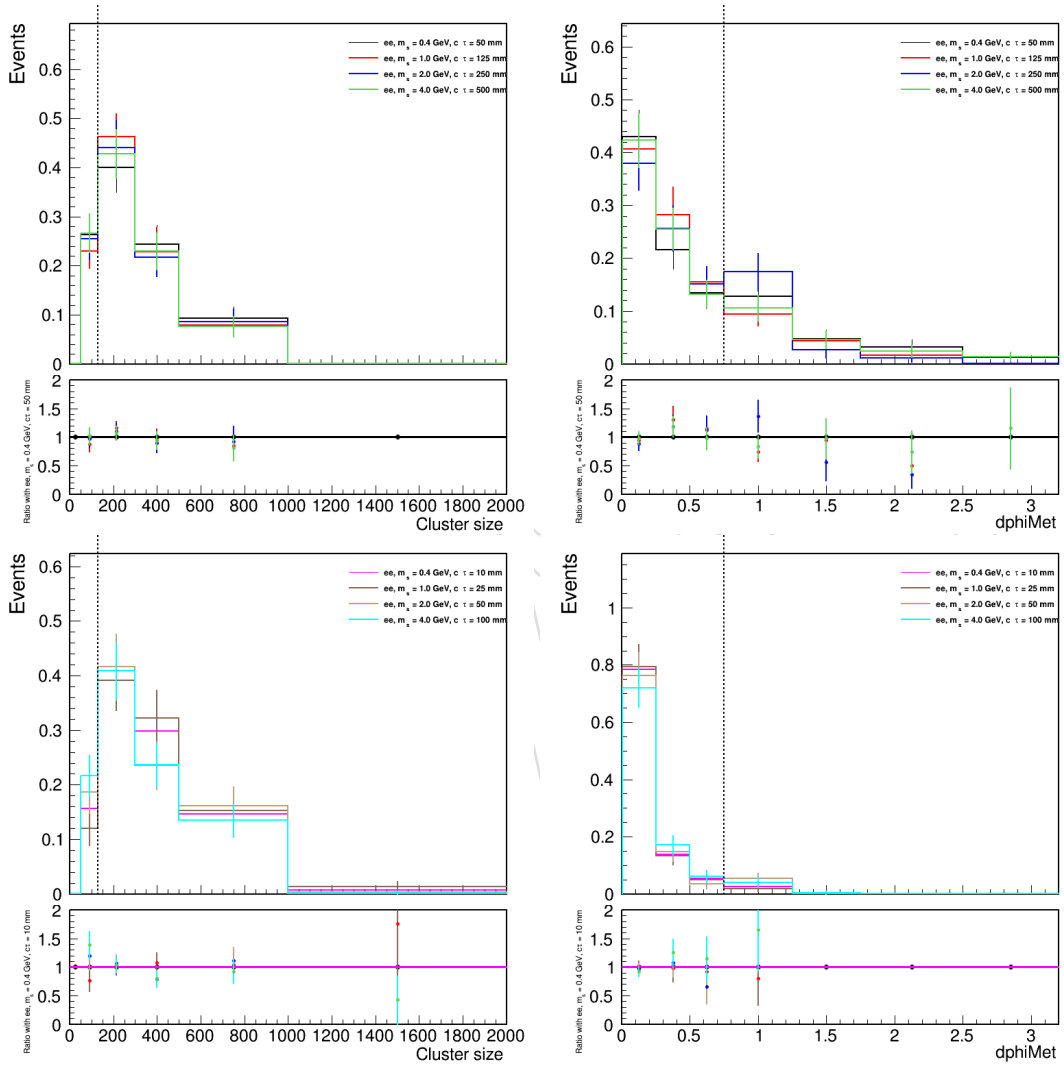


Figure 80: The distributions of the N_{rechits} (left) and $\Delta\phi(\text{cluster}, \text{MET})$ (right) for long lifetime (top) and short lifetime (bottom) ee channel with MET cut

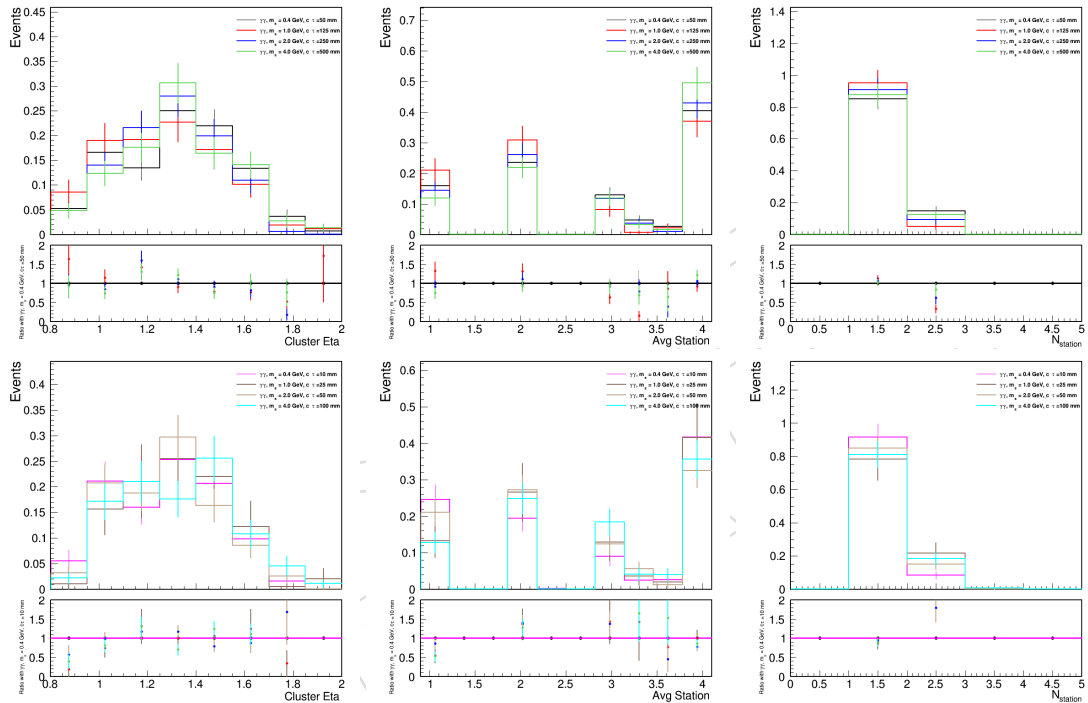


Figure 81: The cluster η (left), average station (center), and number of station (right) distributions are shown for long lifetime (top) and short lifetime (bottom) $\gamma\gamma$ channel with MET cut

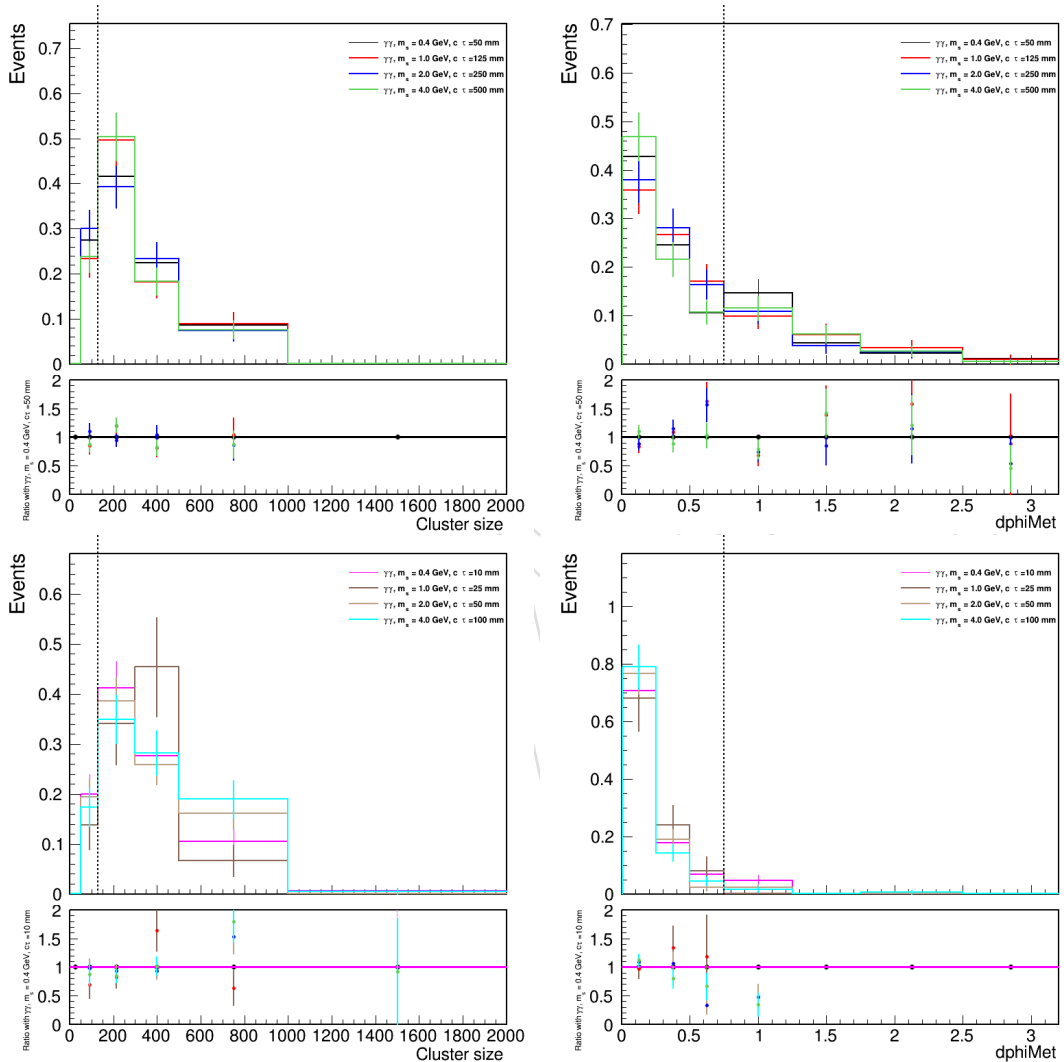


Figure 82: The distributions of the $N_{rechits}$ (left) and $\Delta\phi(\text{cluster}, \text{MET})$ (right) for long lifetime (top) and short lifetime (bottom) $\gamma\gamma$ channel with MET cut

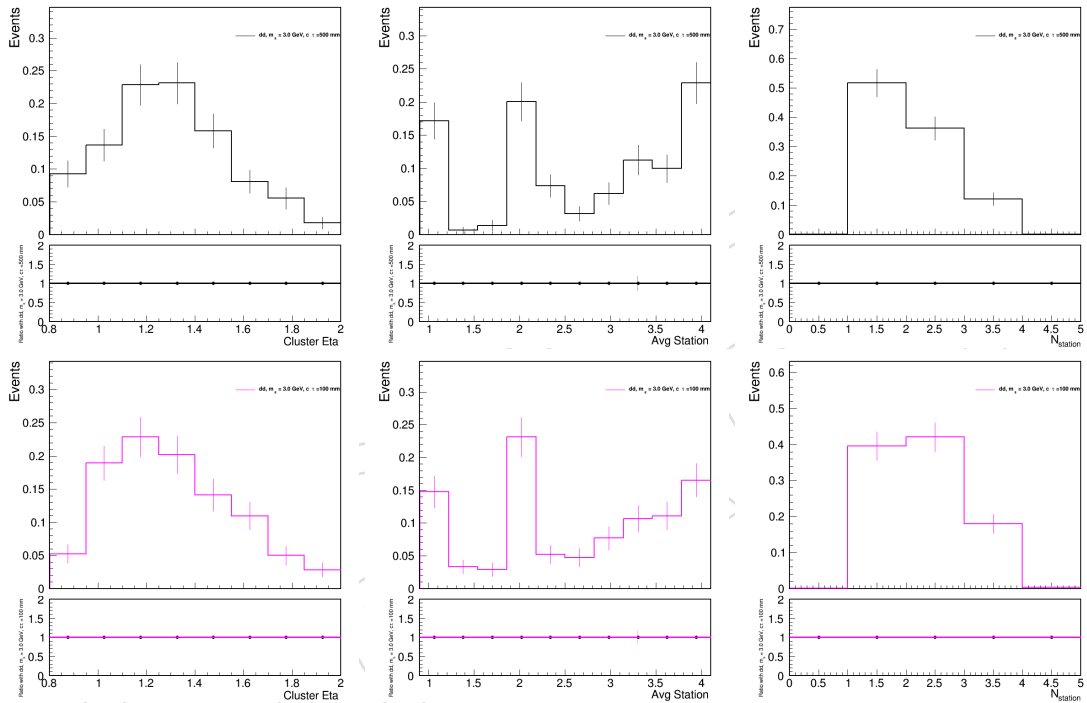


Figure 83: The cluster η (left), average station (center), and number of station (right) distributions are shown for long lifetime (top) and short lifetime (bottom) dd channel with MET cut

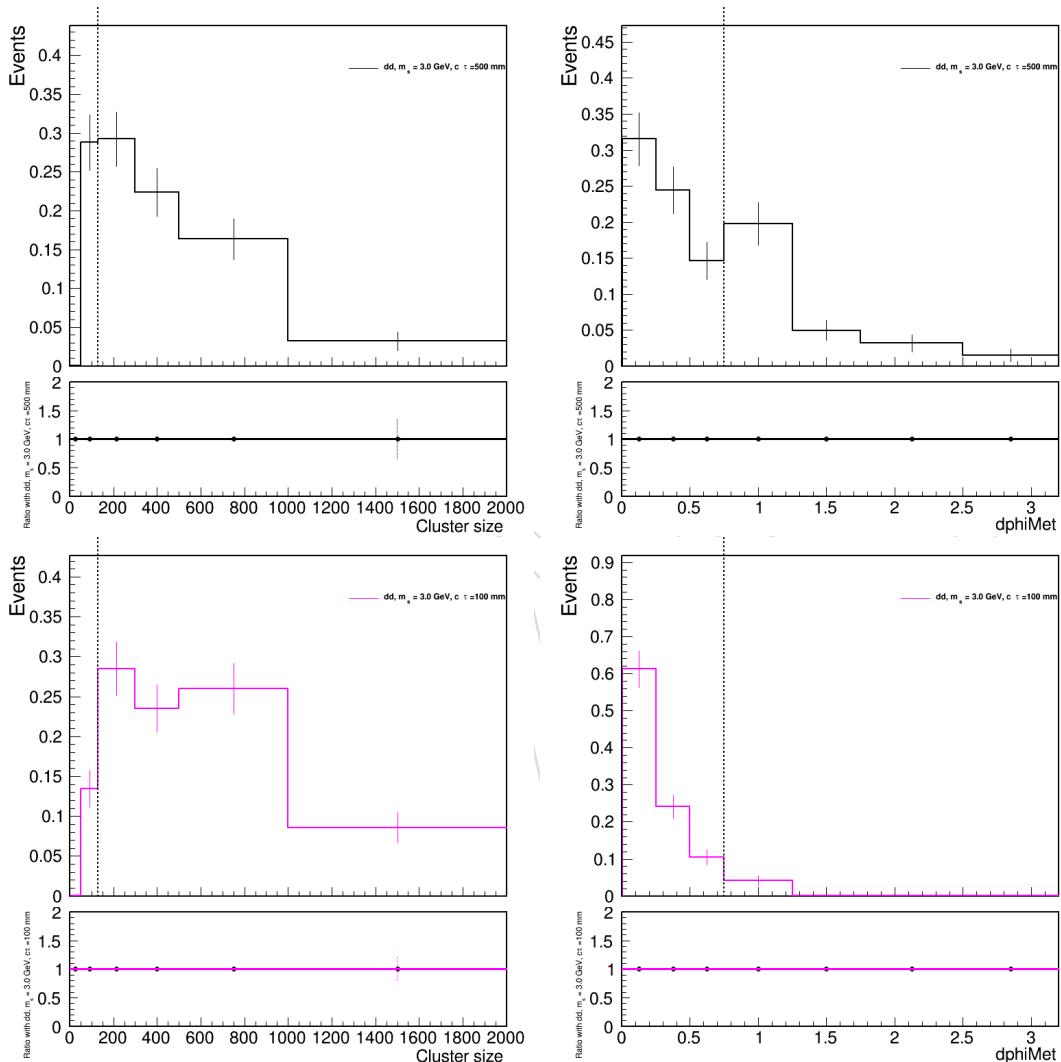


Figure 84: The distributions of the N_{rechits} (left) and $\Delta\phi(\text{cluster}, \text{MET})$ (right) for long lifetime (top) and short lifetime (bottom) dd channel with MET cut

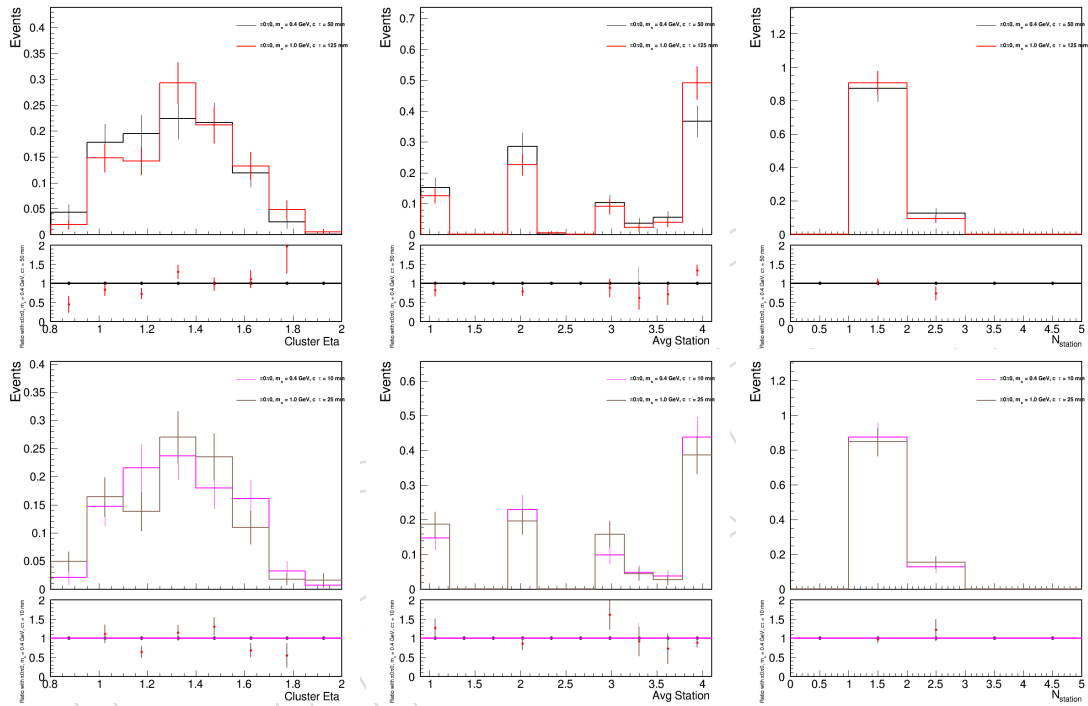


Figure 85: The cluster η (left), average station (center), and number of station (right) distributions are shown for long lifetime (top) and short lifetime (bottom) $\pi^0\pi^0$ channel with MET cut

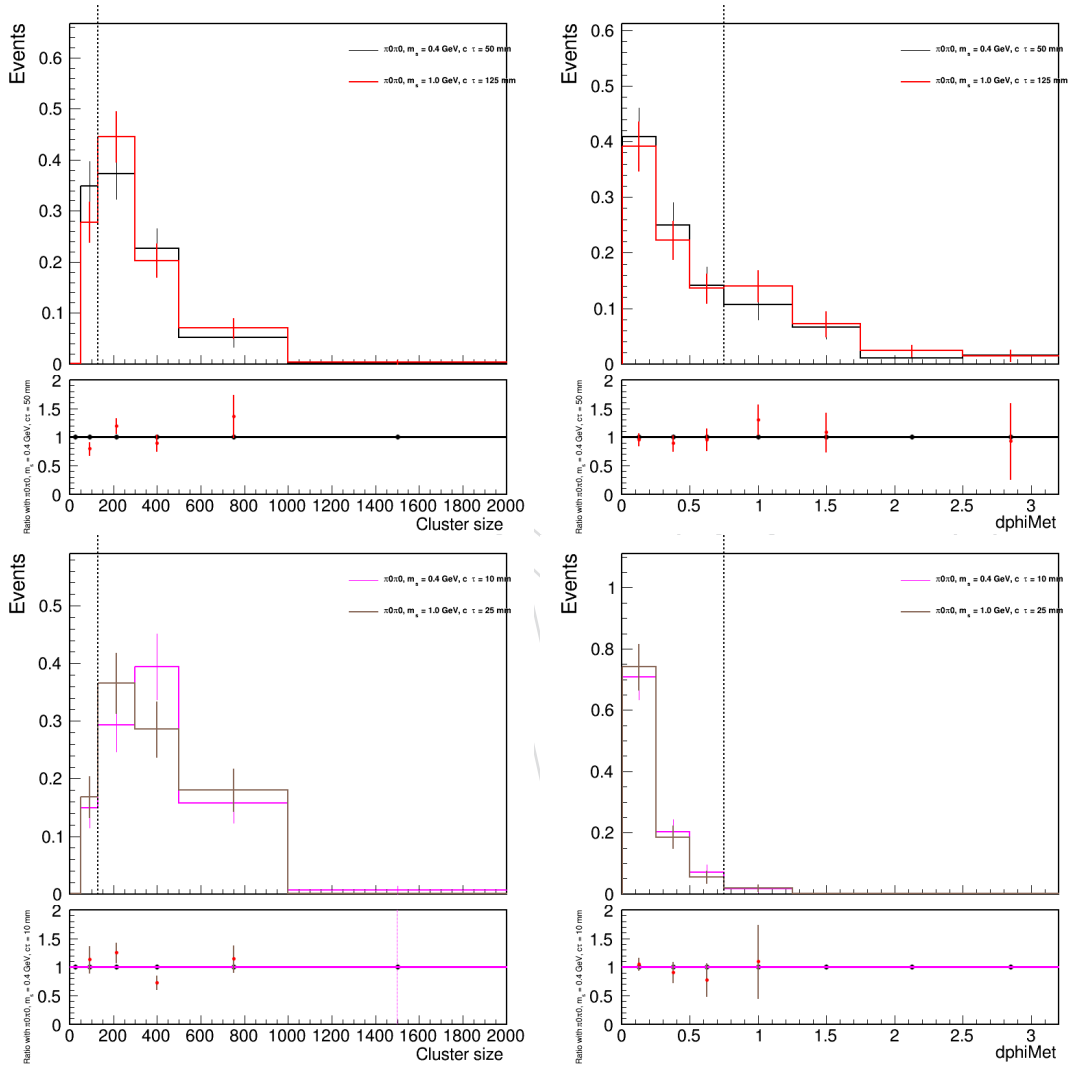


Figure 86: The distributions of the N_{rechits} (left) and $\Delta\phi(\text{cluster}, \text{MET})$ (right) for long lifetime (top) and short lifetime (bottom) $\pi^0\pi^0$ channel with MET cut

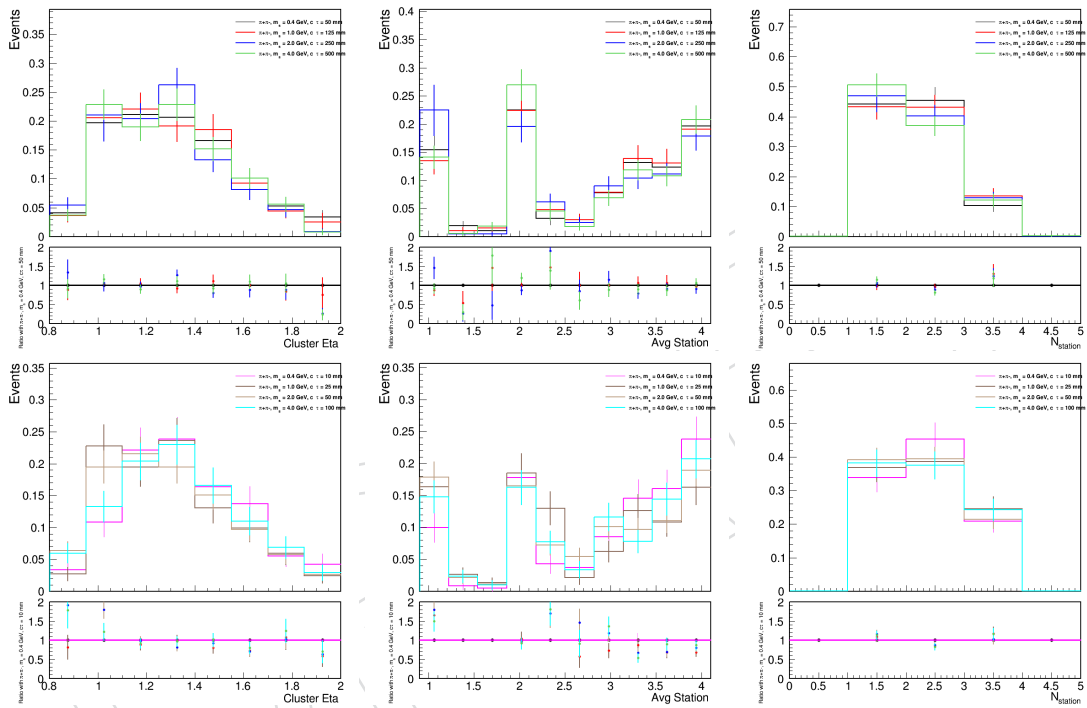


Figure 87: The cluster η (left), average station (center), and number of station (right) distributions are shown for long lifetime (top) and short lifetime (bottom) $\pi^+\pi^-$ channel with MET cut

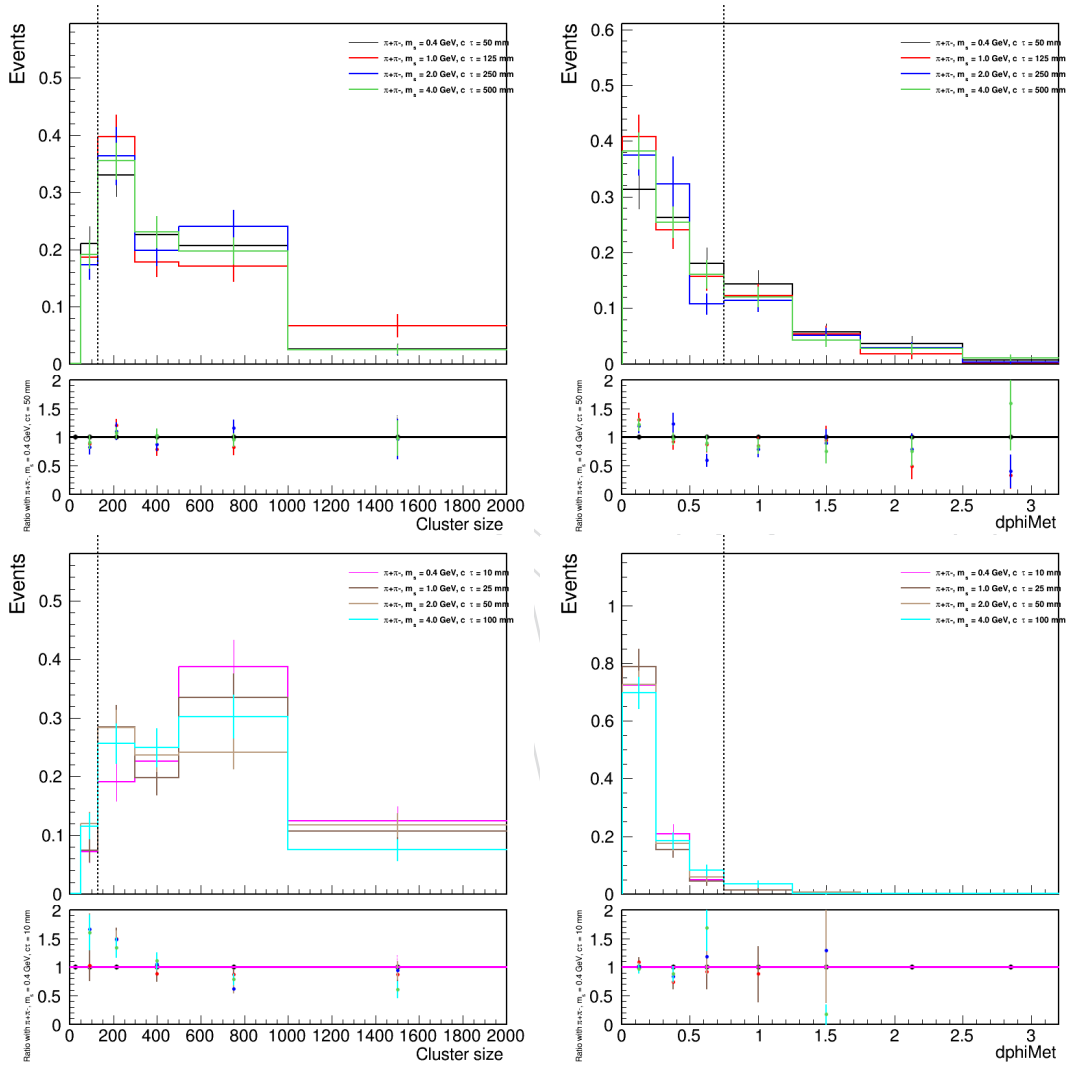


Figure 88: The distributions of the N_{rechits} (left) and $\Delta\phi(\text{cluster}, \text{MET})$ (right) for long lifetime (top) and short lifetime (bottom) $\pi^+\pi^-$ channel with MET cut

1158 **F.2 Sensitivity in low mass region**

1159 To study the sensitivity in the low mass region the masses in Table 69 are used, including the
 1160 ggH, VH, VBF and ttH production channels. The resulting limits are shown in Figure 89. The
 1161 plot shows a peak sensitivity down to the 10^{-2} level and the analysis performs well in this
 1162 region without any changes to the analysis cutflow. For a LLP mass below 0.4 GeV the ee and
 1163 $\gamma\gamma$ decays are the dominating decay channel. To get limits for masses below a mass of 0.4 GeV
 1164 the 0.4 GeV limits presented in Figure 89 is used to scale to lower masses. We move the limit so
 1165 that the $c\tau$ to mass ratio in each point stays the same. This procedure will give a best estimate
 1166 for the limits in this region. The limits for these two decay channels is shown in Figure 90.

Table 69: Masses and lifetimes for the ee, $\gamma\gamma$ and $\pi\pi$ decay channels

decay channel	mass
ee	0.4 GeV
$\gamma\gamma$	0.4 GeV
$\pi\pi$	0.4 GeV, 1.0 GeV
KK	1.5 GeV
dd	3.0 GeV

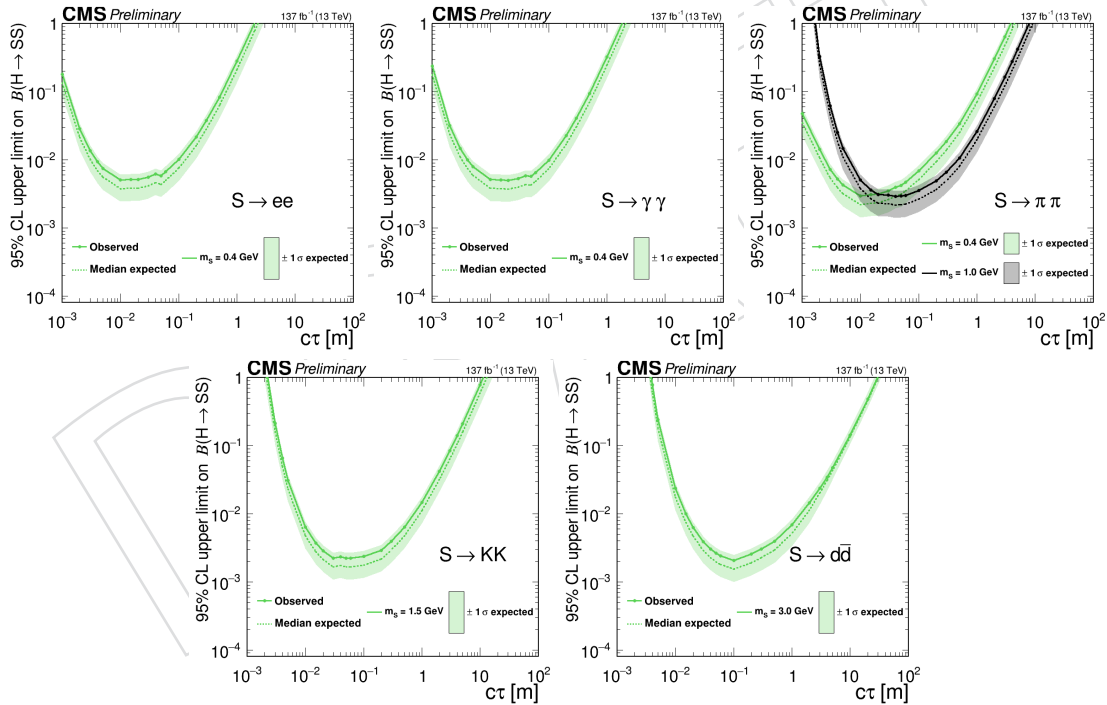


Figure 89: Limits on the low mass samples for the different decay channels

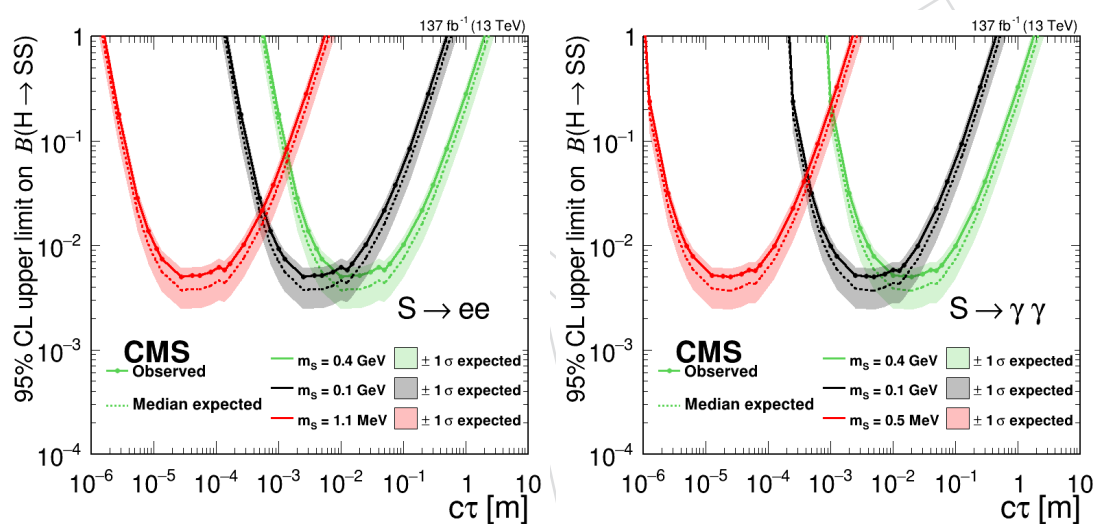


Figure 90: Extrapolation on the low mass limits for ee (left) and $\gamma\gamma$ (right)

1167 G Selection changes for Single Cluster CSC Category

1168 To keep the event-level selections consistent with the single cluster DT and the double cluster
 1169 category we remove the 0 lepton requirement and change the jet p_T cut for the ISR jet from 50
 1170 GeV to 30 GeV from the single cluster CSC category from EXO-20-015.

1171 We have also updated the definition of cluster time and time spread to be consistent with the
 1172 definition in the double cluster categories.

1173 Overall, the changes only change the limits by a few percent.

1174 This section documents the signal yield, observed data, validation of the background estima-
 1175 tion, and single category limit with the updated selections.

1176 G.1 Validation of the Estimation Method

1177 This section documents the updated numbers for the validation of the ABCD method, as pre-
 1178 sented in Section 6.2 in AN-19-154.

1179 G.1.1 Early Out-of-time Validation Region

1180 This section shows the validation of estimation method in the early out-of-time region. The
 1181 looser event-level selections resulted in more background events in the validation region, but
 1182 the background level in signal-enriched region is similar to the original selections. In Table
 1183 70 we show the comparison between the ABCD method prediction and the observation in the
 1184 signal-enriched bin D for the nominal cut values of $N_{rechits} = 130$ and $\Delta\phi(\text{cluster}, \text{MET}) = 0.75$.
 1185 The prediction agrees well with the observation for both cases, within the statistical uncertainty
 1186 of the validation region.

1187 The validation test is also performed for several different values of the cuts in $N_{rechits}$ and
 1188 $\Delta\phi(\text{cluster}, \text{MET})$. In Table 71 and Table 72, we show the validation test results for $N_{rechits}$
 1189 cut boundary values ranging from 100 to 160, while keeping $\Delta\phi(\text{cluster}, \text{MET})$ cut boundary
 1190 fixed at 0.75, for the passing and failing clusterID region, respectively. In Table 73 and Table 74
 1191 we show the validation test result when scanning the $\Delta\phi(\text{cluster}, \text{MET})$ cut boundary from 0.6
 1192 to 0.9, while keeping $N_{rechits}$ cut boundary fixed at 130, for the passing and failing clusterID
 1193 region, respectively. The observed yields in the signal-enriched region D agrees well with the
 1194 prediction in most cases. We also observe no significant trends as the boundaries are varied.

Table 70: Validation of the ABCD method in early OOT validation region at the nominal cut values. The uncertainty of the prediction is the statistical uncertainty propagated from bin A, B, and C.

Cluster ID	A	B	C	D	Prediction ($\frac{A \times C}{B}$)
Pass Cluster ID	8	442	121	3	2.19 ± 0.81
Fail Cluster ID	29	860	266	6	8.97 ± 1.78

Table 71: Validation of the ABCD method in early OOT, pass ID validation region, scanning $N_{rechits}$. The uncertainty of the prediction is the statistical uncertainty propagated from bin A, B, and C.

$N_{rechits}$	A	B	C	D	Prediction ($\frac{A \times C}{B}$)
100	32	418	120	4	9.19 ± 1.88
110	21	429	120	4	5.87 ± 1.42
120	14	436	120	4	3.85 ± 1.10
130	8	442	121	3	2.19 ± 0.81
140	6	444	121	3	1.64 ± 0.69
150	2	448	122	2	0.54 ± 0.39
160	1	449	122	2	0.27 ± 0.27

Table 72: Validation of the ABCD method in early OOT, fail ID validation region, scanning $N_{rechits}$. The uncertainty of the prediction is the statistical uncertainty propagated from bin A, B, and C.

$N_{rechits}$	A	B	C	D	Prediction ($\frac{A \times C}{B}$)
100	80	809	252	20	24.92 ± 3.32
110	51	838	259	13	15.76 ± 2.48
120	40	849	262	10	12.34 ± 2.14
130	29	860	266	6	8.97 ± 1.78
140	21	868	270	2	6.53 ± 1.50
150	16	873	270	2	4.95 ± 1.28
160	13	876	271	1	4.02 ± 1.15

Table 73: Validation of the ABCD method in early OOT, pass ID validation region, scanning $\Delta\phi(\text{cluster}, \text{MET})$. The uncertainty of the prediction is the statistical uncertainty propagated from bin A, B, and C.

$\Delta\phi(\text{cluster}, \text{MET})$	A	B	C	D	Prediction ($\frac{A \times C}{B}$)
0.60	8	470	93	3	1.58 ± 0.59
0.65	8	464	99	3	1.71 ± 0.63
0.70	8	449	114	3	2.03 ± 0.75
0.75	8	442	121	3	2.19 ± 0.81
0.80	8	432	131	3	2.43 ± 0.89
0.85	8	421	142	3	2.70 ± 0.99
0.90	8	406	157	3	3.09 ± 1.13

Table 74: Validation of the ABCD method in early OOT, fail ID validation region, scanning $\Delta\phi(\text{cluster}, \text{MET})$. The uncertainty of the prediction is the statistical uncertainty propagated from bin A, B, and C.

$\Delta\phi(\text{cluster}, \text{MET})$	A	B	C	D	Prediction ($\frac{A \times C}{B}$)
0.60	29	922	204	6	6.42 ± 1.29
0.65	29	902	224	6	7.2 ± 1.44
0.70	29	882	244	6	8.02 ± 1.60
0.75	29	860	266	6	8.97 ± 1.78
0.80	28	843	283	7	9.4 ± 1.89
0.85	28	822	304	7	10.36 ± 2.08
0.90	28	806	320	7	11.12 ± 2.23

1195 **G.1.2 In-time Validation Region**

1196 We show the validation of the estimation method in the in-time validation region in this section.

1197 In Table 75, we compare the observed event yield in the signal-enriched bin D with the ABCD
1198 method prediction and observe agreement. Since good agreement is observed in both valida-
1199 tion regions, we assign no systematic uncertainty to the background prediction.

1200 Similar to the OOT validation region, we also perform the validation test for a range of cut
1201 boundary values on the $N_{rechits}$ and $\Delta\phi(\text{cluster}, \text{MET})$ variable. Table 76 shows the valida-
1202 tion test results for $N_{rechits}$ cut boundary values ranging from 100 to 160, while keeping the
1203 $\Delta\phi(\text{cluster}, \text{MET})$ boundary fixed at 0.75. Table 77 shows the validation test result for $\Delta\phi(\text{cluster}, \text{MET})$
1204 boundary values ranging from 0.6 to 0, while keeping $N_{rechits}$ boundary fixed at 130.

Table 75: Validation of the ABCD method in in-time validation region. The uncertainty of the prediction is the statistical uncertainty propagated from bin A, B, and C.

Cluster ID	A	B	C	D	Prediction ($\frac{A \times C}{B}$)
Fail Cluster ID	8	317	87	2	2.2 ± 0.82

Table 76: Validation of the ABCD method in in-time validation region, scanning $N_{rechits}$. The uncertainty of the prediction is the statistical uncertainty propagated from bin A, B, and C.

$N_{rechits}$	A	B	C	D	Prediction ($\frac{A \times C}{B}$)
100	21	304	83	6	5.73 ± 1.44
110	13	312	86	3	3.58 ± 1.09
120	11	314	86	3	3.01 ± 0.98
130	8	317	87	2	2.2 ± 0.82
140	6	319	89	0	1.67 ± 0.71
150	4	321	89	0	1.11 ± 0.57
160	3	322	89	0	0.83 ± 0.49

Table 77: Validation of the ABCD method in in-time validation region, scanning $\Delta\phi(\text{cluster}, \text{MET})$. The uncertainty of the prediction is the statistical uncertainty propagated from bin A, B, and C.

$\Delta\phi(\text{cluster}, \text{MET})$	A	B	C	D	Prediction ($\frac{A \times C}{B}$)
0.60	9	332	72	1	1.95 ± 0.7
0.65	9	328	76	1	2.09 ± 0.74
0.70	8	323	81	2	2.01 ± 0.75
0.75	8	317	87	2	2.2 ± 0.82
0.80	8	309	95	2	2.46 ± 0.92
0.85	7	309	95	3	2.15 ± 0.85
0.90	7	293	111	3	2.65 ± 1.04

1205 **G.2 Results**

1206 We present results of the search in this section with the updated selections.

1207 **G.2.1 Signal Prediction**

1208 The expected number of signal events with the updated selections and overlap with dou-
1209 ble cluster category removed, for bb decay mode, assuming $BR(H \rightarrow ss) = 1\%$ for several LLP
masses and proper lifetime $c\tau$ are shown in Table 78.

Table 78: Signal Yield in the signal region in binD for different production modes, assuming $BR(H \rightarrow ss) = 1\%$.

ggH				
LLP mass $c\tau$	0.1 m	1 m	10 m	100 m
15 GeV	6.4	19.9	5.2	0.6
40 GeV	0.2	16.1	14.7	1.9
55 GeV	0.0	7.1	18.6	2.9
VBF				
LLP mass $c\tau$	0.1 m	1 m	10 m	100 m
15 GeV	2.0	6.0	1.5	0.2
40 GeV	0.0	5.0	4.4	0.7
55 GeV	0.0	2.3	6.1	0.9
WH				
LLP mass $c\tau$	0.1 m	1 m	10 m	100 m
15 GeV	0.6	2.2	0.5	0.1
40 GeV	0.0	1.6	1.3	0.2
55 GeV	0.0	0.7	1.9	0.3
qqZH				
LLP mass $c\tau$	0.1 m	1 m	10 m	100 m
15 GeV	0.4	1.1	0.3	0.0
40 GeV	0.0	1.1	0.9	0.1
55 GeV	0.0	0.5	1.0	0.2
ggZH				
LLP mass $c\tau$	0.1 m	1 m	10 m	100 m
15 GeV	0.1	0.4	0.1	0.0
40 GeV	0.0	0.4	0.4	0.1
55 GeV	0.0	0.1	0.4	0.1
ttH				
LLP mass $c\tau$	0.1 m	1 m	10 m	100 m
15 GeV	0.4	1.8	0.4	0.0
40 GeV	0.0	1.4	1.2	0.2
55 GeV	0.0	0.6	1.5	0.2

1210

1211 **G.2.2 Observed Data**

1212 The number of background events predicted from the background-only fit in the signal re-
1213 gion (in-time region passing the cluster ID) is summarized in Table 79, as well as the observed
1214 yields. With the ABCD method fitted to the observed data, we predict 1.8 ± 0.9 (stat) events

in the signal-enriched region D, and observe 3 events in the data. We observe no statistically significant deviation with respect to the expected number of events.

Table 79: Number of background events in the signal region observed and predicted by the background-only fit using the ABCD method.

	A	B	C	D
Bkg-only fit prediction	4.2 ± 1.7	119.8 ± 11.1	51.2 ± 6.6	1.8 ± 0.8
Observed	3	121	50	3

G.2.3 Expected and Observed Limits

The updated expected and observed limits (calculated using Asymptotic Limits for now, we run with HybridNew method in the next iteration) on the Higgs decay branching ratio to LLPs is shown in Fig. 91, separately for scenarios where each LLP exclusively decays into 2 b quarks, 2 d quarks, and 2 τ leptons. The signal contributions of all the available productions are included, including ggH, VBF, VH, and ttH. The observed limits presented is about 3% better than the observed limits presented in AN-19-154.

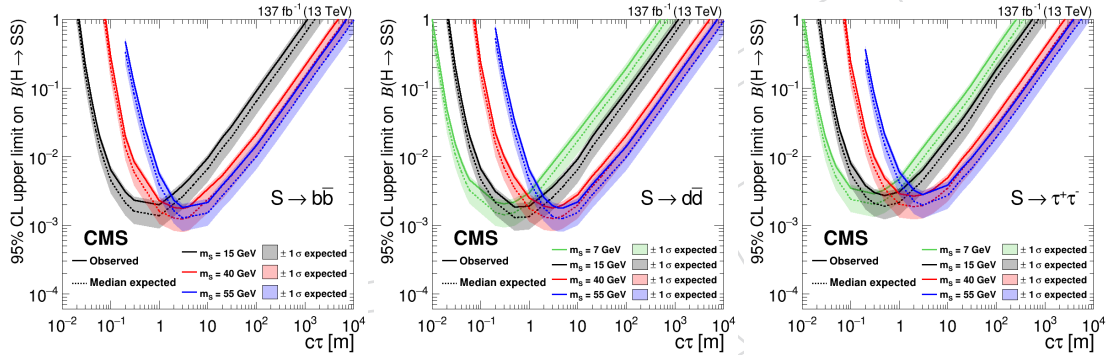


Figure 91: The observed and expected limit for signal predictions that include ggH, VBF, VH, and ttH production modes for 4b (Left), 4d (Middle), 4 τ (Right) decay modes are shown. The additional contribution from the sub-dominant production modes increases the signal yield by 54%.

H Background Composition for Single CSC Cluster Category

In this section, we present the study for the background composition of the clusters passing all the vetos in the single CSC cluster category in MC samples.

The samples that are being used are W+jets, Minimum Bias sample, and privately produced particle guns consisting of K_L^0 , K^+ , and π^+ with p_T of 2, 5, and 10 GeV, respectively. The full list of samples are summarized in Table 80.

Table 80: MC simulation samples used for background composition study.

/MinBias_TuneCP5_13TeV-pythia8/RunIIFall18GS-102X_upgrade2018_realistic_v9-v1/GEN-SIM
/WJetsToLNu_TuneCP5_13TeV-madgraphMLM-pythia8/RunIIFall18wmLHEGS-102X_upgrade2018_realistic_v11-v2/GEN-SIM
ParticleGun_K0Lpt2
ParticleGun_K0Lpt5
ParticleGun_K0Lpt10
ParticleGun_KPluspt2
ParticleGun_KPluspt5
ParticleGun_KPluspt10
ParticleGun_PiPluspt2
ParticleGun_PiPluspt5
ParticleGun_PiPluspt10

Due to the limited availability of background simulation samples with the CSC and DT rechit collections available, the only signal region sample available for the background composition study was the WJetsToLNu sample. Private reprocessing of this sample was necessary to gain access to the CSC and DT rechit collections because the AODSIM data-tier of the centrally produced samples do not contain these rechit collections. The CSC and DT rechit clusters from this W+jets sample are representative of the clusters in the final signal region. There are a total of 7.1×10^7 events in the sample, and after we apply most of the cluster-level selections, including the jet, muon, ME11/12, RE12, RB1, MB1 segment veto, time spread cut, time cut, and $N_{rechits}$ cut, we are left with 1084 events with one CSC cluster.

We found that among the 1084 events, 34% of the clusters are matched to a generator-level muon. These clusters were all required to pass the muon veto, and therefore are cases where the muon reconstruction failed. The overwhelming majority of such clusters are matched to generator-level muons with large η values near the edge of the CSC acceptance, as shown in Fig. 92, and for this reason often fail to be reconstructed. In our analysis, we apply the $|\eta| < 2$ cut to explicitly reject such background clusters.

Of the remaining clusters, we observed that the majority of clusters are matched to low p_T generator-level kaons and pions, as shown in Table 81. Initially, we suspected that the matching between these clusters and the low p_T pions and kaons were accidental and that other particles from pileup may be the real cause for the cluster objects, and were not found simply because generator-level pileup particles are not saved in the event record.

To verify this hypothesis, we performed the same study using the MininumBias simulation sample without any pileup events mixed in. The MinBias sample has a total of 3.3×10^8 events, and after we apply the same cluster-level selections, we found 76 events with one CSC cluster, which results in a cluster efficiency of about 2.3e-7. Similarly, we match the CSC clusters to status 1 generator-level particles to study the origin of the background clusters. We found that similar to the WJetsToLNu sample after removing the muon contribution, most clusters are matched to low p_T pions and kaons, as shown in Table 82.

To confirm that the background clusters really are produced by these low p_T pions and kaons, suggested by the W+jets and Minimum Bias simulation samples, we produced particle gun samples for K_L^0 , K^+ , and π^+ with p_T of 2, 5, and 10 GeV in order to verify that such low mo-

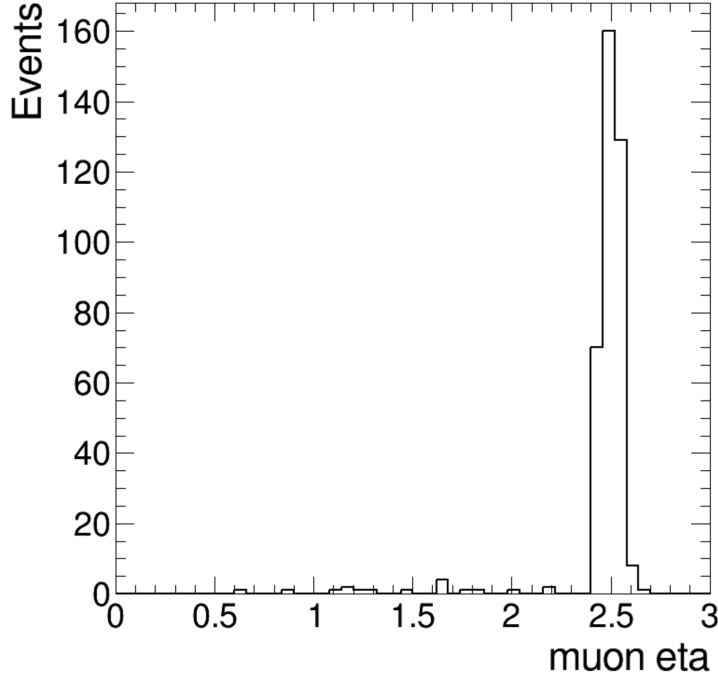


Figure 92: The distribution of gen-level muon $|\eta|$ of the muons that are matched to clusters passing all vetos in the WJetsToLNu sample.

Table 81: A breakdown of the generator-level particles that are matched to background CSC clusters passing the cluster selections in the WJetsToLNu sample. The cases where no match was found are interpreted to be caused by pileup particles, for which generator level particles are not stored in the event record.

particle type	fraction of events
K_L^0	3.6%
K_S^0	3.1%
charged kaon $p_T > 2 \text{ GeV}$	0.6%
charged pion $p_T > 2 \text{ GeV}$	2.5%
charged kaon $1.5 < p_T < 2.5 \text{ GeV}$	1.1%
charged pion $1.5 < p_T < 2.5 \text{ GeV}$	5.2%
charged kaon $0.5 < p_T < 1.5 \text{ GeV}$	22.9%
charged pion $0.5 < p_T < 1.5 \text{ GeV}$	44.2%
not matched to any status 1 genParticles	16.8%

1260 momentum single particles can in fact produce the CSC clusters of the type observed in our back-
1261 ground samples.

1262 We observed that the efficiency of reconstructing a cluster (without any vetos) is of the order of
1263 10^{-5} to 10^{-3} for both kaons and pions, increasing with p_T of the particle. We further observed
1264 that the efficiency of reconstructing a cluster passing all selections is on the order of 10^{-6} to
1265 10^{-7} , which roughly agree with what we observed in the Minimum Bias simulation sample. A
1266 summary of the particle gun cluster efficiencies are shown in Table 83.

1267 We also show in Figure 93 the N_{rechits} distribution for the clusters from 2 GeV K_L^0 , K^+ , and π^+ ,
1268 demonstrating that, although very rarely, low p_T pions and kaons can produce clusters with a

Table 82: Breakdown of the type of status 1 generator-level particles that CSC clusters are matched to in MinBias sample.

particle type	fraction of events
muon	3.9%
K_L^0	7.9%
K_S^0	5.3%
charged kaon $p_T > 2 \text{ GeV}$	2.6%
charged pion $p_T > 2 \text{ GeV}$	5.3%
charged kaon $1.5 < p_T < 2.5 \text{ GeV}$	2.6%
charged pion $1.5 < p_T < 2.5 \text{ GeV}$	5.3%
charged kaon $0.5 < p_T < 1.5 \text{ GeV}$	23.7%
charged pion $0.5 < p_T < 1.5 \text{ GeV}$	43.4%

Table 83: Summary of cluster efficiencies for single particle guns. We study K_L^0 , K^+ , and π^+ with p_T ranging from 2 to 10 GeV.

sample	Total N_{events}	cluster efficiency (No veto)	efficiency with all selections (except for $N_{rechits} > 130$)	efficiency with all selections including $N_{rechits} > 130$
K0Lpt2	2.5E+07	2.4E-05	2.8E-07	0E+00
K0Lpt5	2.5E+07	2.4E-04	1.9E-06	1.6E-07
K0Lpt10	2.4E+07	9.3E-04	5.3E-06	1.8E-06
KPluspt2	2.5E+07	2.2E-05	3.7E-07	0E+00
KPluspt5	2.5E+07	3.4E-04	1.5E-06	4.0E-08
KPluspt10	2.3E+07	9.7E-04	1.8E-06	1.3E-07
PiPluspt2	2.5E+07	1.7E-05	4.1E-08	0E+00
PiPluspt5	2.5E+07	3.3E-04	7.3E-07	0E+00
PiPluspt10	2.3E+07	1.4E-03	1.3E-06	1.3E-07

¹²⁶⁹ large number of rechits.

¹²⁷⁰ Based on these studies with WJetsToLNu, Minimum Bias, and particle gun simulation samples,
¹²⁷¹ we conclude that after all the cluster-level vetos that reject clusters from jets and muons with
¹²⁷² high p_T , the dominant background clusters are from low p_T pions and kaons. They will very
¹²⁷³ rarely punchthrough the shielding material and produce background clusters with large cluster
¹²⁷⁴ size. However, due to the large flux of low p_T pions and kaons in LHC collision events, they
¹²⁷⁵ are the dominant source of background CSC clusters.

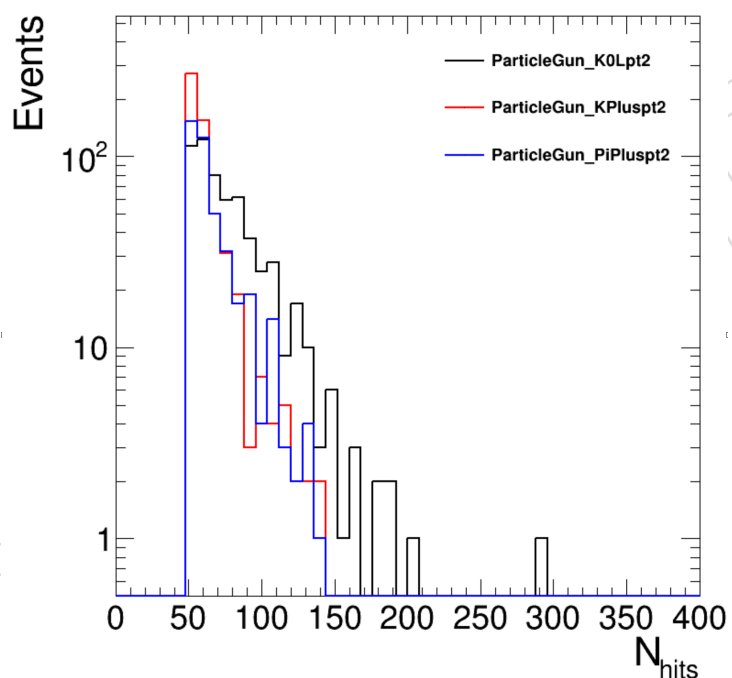


Figure 93: The distribution of $N_{rechits}$ for the clusters in the 2 GeV particle gun samples.